University of Strathclyde

Department of Mechanical & Aerospace Engineering

Water flow at the nanoscale: a computational molecular and fluid dynamics investigation

Konstantinos Ritos

A thesis presented in fulfilment of the requirements
for the degree of Doctor of Philosophy

2014

Declaration of author's rights

This thesis is the result of the author's original research. It has been composed by the author and has not been previously submitted for examination which has led to the award of a degree.

Konstantinos Ritos

October 2014

Abstract

A complete understanding of the most common and abundant fluid on Earth, water, has challenged the scientific community since the dawn of science. Nanoscale confinement and flow through nanotubes show counter-intuitive behaviour and produce interesting new phenomena.

Experimental studies of water flow at the nanoscale report diverse results because measurement devices still struggle to provide the necessary accuracy. Molecular Dynamics (MD) simulations can instead provide molecular detail and a plethora of information. The main disadvantage of the method is space and time restraints on the simulated problems. To overcome this, hybrid multiscale methods that combine MD with macroscopic equations have been recently developed.

This thesis investigates water flow at the nanoscale, over free surfaces and in nanotube membranes, using MD, multiscale methods and macroscopic hydrodynamic equations. Initially, water nanodroplets on static and moving surfaces of different hydrophilicity are studied here with the developed MD solver. The findings, contrary to macroscopic observations, suggest that the dynamic contact angle of water nanodroplets on graphite is independent of the capillary number.

Then, a new method is firstly presented here in order to measure the average molecular orientation of water and highlight any type of anisotropy. For the first time, biaxial ordering of water molecules close to the nanotube walls is observed. It is also found that static electric fields can control the flow rate through them (e.g. a 2 V/nm electric field increases the flow rate by more than 300% for the same pressure difference).

The effect of the wall material on water flow is also investigated. The accuracy of a flow enhancement prediction model originally suggested by Mattia *et al.* [1] is tested, giving satisfactory results for nanotube membranes of small thickness.

Finally, results from hybrid multiscale simulations are presented in this thesis, showing perfect agreement with pure MD simulations. The same multiscale method is used for the first time to simulate water flow through a millimeter thick membrane with a pore diameter smaller than 2 nm.

All the results presented in this thesis contribute towards the better understanding of water flow at the nanoscale. In parallel this thesis provides a number of computational tools and methods that will help in future studies as well as in the design and simulation of nanoscale fluid devices.

Acknowledgements

First and foremost I want to express my sincere gratitude and deepest appreciation to my supervisor, Prof. Jason M. Reese, for his continuous guidance, knowledge, advices, trust and support that he provided throughout the past 3 and a half years.

I am also grateful to Dr Davide Mattia, at the University of Bath, for the opportunity to visit his laboratory and experience the procedure of building, visualising and testing nanomaterials. Thanks also go to Prof. Nigel J. Mottram, at the University of Strathclyde, for all the interesting meetings where he patiently introduced me in the unfamiliar area of liquid crystals and the mathematical analysis of ordering in fluids. The fruitful collaboration with both of them led to publications and chapters of this thesis.

Thank you to the rest of the researchers in the James Weir Fluids Laboratory for many useful and enlightening discussions throughout this process. In particular; Dr Matthew K. Borg for the numerous discussions on OpenFOAM programming, molecular dynamics, multiscale hybrid simulations and answers to many queries. Dr Nishanth Dongari for many hours of discussions on all things from general thermodynamics and fluid dynamics, to nanodroplet dynamics and liquid film theory. Dr William Nicholls and Dr Craig White for putting up with my many queries while I learned OpenFOAM, and Stephanie Docherty for the daunting task of proofreading this thesis.

I recognise, and am thankful for, the financial support of the EPSRC in the form of the scholarship that they have provided me with.

Last, but by no means least, I would like to express my utmost gratitude to my family, who have supported me unconditionally throughout my whole life and education. My family has been a constant source of love, concern and strength all these years and I dedicate this thesis to them.

Contents

List of figures

List of tables

Nomenclature

$\mathbf{a}$	acceleration (m/s^2)
Ca	Capillary number (-)
C	coefficient of fluid entrance and exit losses (-)
ch	magnitude of chiral vector (-)
D	diameter (m)
D_r	reduced diameter (m)
D_s	self diffusivity (m^2/s)
$\mathbf{E}$	electric field (V/m)
E	electric field magnitude (V/m)
E_{bm}	bulk modulus fluid elasticity of water (N/m^2)
$\mathbf{F}$	force (N)
$\bar{F}$	Gaussian force peak value (N)
f	scaling function (-)
g	radial distribution function (-)
H	contact angle hysteresis (-)
h	Planck's constant (m^2 kg/s)
$\mathbf{I}$	second rank identity tensor (-)
k_B	Boltzmann's constant (m^2 kg s^{-2} K^{-1})
L	length (m)
L_s	slip length (m)
m	mass (kg)
$\dot{\mathrm{m}}$	mass flow rate (kg/s)
$\bar{\dot{\mathrm{m}}}$	mean mass flow rate (kg/s)
N	number of (-)

n_{HB}	number of hydrogen bonds (-)
$\hat{\boldsymbol{n}}$	unit vector (-)
$\mathbf{n}$, $\mathbf{l}$, $\mathbf{m}$	orthogonal directors (-)
P	pressure (Pa)
$\dot{Q}$	volumetric flow rate (m^3/s)
$\mathbf{Q}$, $\mathbf{B}$	order tensors (-)
$\mathbf{q}$, $\mathbf{b}$	microscopic counterparts of order tensors $\mathbf{Q}$, $\mathbf{B}$ (-)
q	charge (C)
R	radius (m)
$\mathbf{r}$	position (m)
r, θ, z	spatial cylindrical co-ordinates (m, °, m)
r_B	droplet base radius (m)
r_{cut}	potential truncation radius (m)
T	temperature (K)
t	time (s)
U	interatomic potential energy (J)
u	velocity (m/s)
$\boldsymbol{u}$	velocity vector (m/s)
W_A	work of adhesion (N/m)
x, y, z	spatial Cartesian co-ordinates (m, m, m)

Greek

α	anisotropy parameter (-)
β^2	biaxiality parameter (-)
γ	surface tension (N/m)
δ	Kronecker's delta (-)
ΔE	binding energy (J)
Δt	time-step (s)
ΔP	pressure difference (Pa)
δt	timestep of macro solver in SHMM (s)
ε	depth of the potential well (J)

ε_0	vacuum permittivity (C^2 N^{-1} m^{-2})
ϵ	flow enhancement, MD over no-slip Hagen-Poiseuille prediction (-)
ζ	convergence criterion (-)
θ	microscopic advancing contact angle (°)
θ_∞	macroscopic static contact angle (°)
θ_D	microscopic dynamic contact angle (°)
θ_s	microscopic static contact angle (°)
Λ	de Broglie wavelength (m)
λ	eigenvalue (-)
μ	dynamic viscosity (Pa s)
ξ	eigenvector (-)
Π	number of micro elements (-)
ρ	mass density (kg/m^3)
ρ_n	number density (m^{-3})
ρ^*	mass density in reduced units (-)
σ	finite distance at which the inter-particle potential is zero (m)
σ_s	standard deviation of distribution (-)
τ	line tension (J/m)
$\tilde{\tau}$	number of MD time-steps used for sampling (-)
ϕ	microscopic receding contact angle (°)
ψ	relaxation coefficient (Pa s/kg)
Ω	domain (-)
ω	effective hydrodynamic diameter of a water molecule (Å)

Superscripts

$*$	reduced units
l	iteration index

Subscripts

∞	macroscopic
0	reference, no electric field

[1]	eigenvalue index
A	atomistic
at	atoms
av	averaging
B	regarding order tensor $\mathbf{B}$
Bu	bulk
b	droplet base
C	continuum
Cou	Coulomb
D	dynamic
E	electric field
H	hybrid IMM
HP	Hagen-Poiseuille
HPm	modified Hagen-Poiseuille
i, j	atom or microelement indexes
in	inlet reservoir
$iner$	inertia
L	liquid phase
M	macroscale
m	microscale or molecular
MD	molecular dynamics
O	overlapping
out	outlet reservoir
Q	regarding order tensor $\mathbf{Q}$
S	solid phase
s	static
$shift$	shifted potential
st	surface tension
tol	tolerance
V	vapor phase
vis	viscous
W	near tube wall

Acronyms

ARCHIE-WeST	Academic and Research Computer Hosting Industry and Enterprise in the West of Scotland
BNNT	boron nitride nanotube
CFD	computational fluid dynamics
CNT	carbon nanotube
CPU	central processing unit
DDM	domain decomposition method
GPU	graphics processing unit
HB	hydrogen bonds
HMM	heterogeneous multiscale method
HP	Hagen-Poiseuille
HPC	high performance computer
IMM	internal-flow multiscale method
LB	Lorentz-Berthelot
LJ	Lennard-Jones
MD	molecular dynamics
MEMS	microelectromechanical system
NEMS	nanoelectromechanical system
NPT	isothermal-isobaric ensemble
NVE	microcanonical ensemble
NVT	canonical ensemble
OpenFOAM	Open Field Operation And Manipulation
RAM	random-access memory
RDF	radial distribution function
RO	reverse osmosis
SiCNT	silicon carbide nanotube
SPC/E	extended simple point charge model
SHMM	seamless HMM
TIP3P	transferable intermolecular potential 3P
TIP4P	transferable intermolecular potential 4P
TIP4P/2005	2005 version of TIP4P

Chapter 1

Introduction

Αρχή ήμισυ παντός.

- Πλάτωνας (427-347 π.Χ.)

The beginning is the most important part of the work.

- Plato (427-347 B.C.)

1.1 Motivation

After the rediscovery of carbon nanotubes (CNTs) in 1991 by Iijima [2] there was an exponential growth in scientific publications [3] regarding their possible applications and unique mechanical, electromechanical, structural and fluid transport properties. Possible application areas include, but are not restricted to, drug delivery [4, 5], molecular detection [6, 7], water filtration and desalination [8, 9], gas storage [10, 11], and nanoelectronics [12, 13].

During the last 15 years, and after the first Molecular Dynamics (MD) simulation of water in CNTs [14], a significant part of the relevant research is about the computational modelling and study of water confined and/or flowing in nanotubes. The choice of water as the fluid of interest is not random but is based on the fact that it is the universal solvent, and although it is the most studied liquid of all, a significant number of its properties are far from understood [15, 16]. With the existence of numerous water-filled and water-permeable pores in biological cells, on the surface of proteins, and in membranes [17], the importance of studying water behaviour inside nanotubes is

recognised. In addition to this, reverse osmosis (RO) is currently the most widely used desalination technology globally with nanotube based RO membranes probably being the next state-of-the-art technology [9].

Despite the great amount of experimental and computational research over the last 2 decades, there are still open problems, contradictory results, and results that cannot be adequately explained with current mathematical models [18]. The purpose of this thesis is to investigate water flows at the nanoscale, in particular, through nanotube membranes. New physical observations provide further insight to previous puzzling results and a better understanding of water flow in nanotubes. This study is not limited to the research and understanding of physical phenomena occurring at the nanoscale, but it also develops and combines new and existing mathematical models as well as computational methods. In the remainder of this chapter an outline of this thesis is given as well as a justification of the chosen computational methods.

1.2 Thesis outline

Simulations of water nanodroplets on static and moving solid surfaces are presented in Chapter 2. An overview of the simulation domain and the used parameters is given, along with a description of the density and hydrogen bonding measurements. The water–graphite potential calibration is also given in detail, followed by contact angle measurements on static and moving surfaces of different hydrophobicity. The potential calibration is essential for this research as the majority of the studied flows are inside graphitic surfaces, i.e. CNTs.

Chapter 3 presents the nanotube membrane geometry and simulation results of water flow in a CNT. The Gaussian forcing method for imposing a pressure difference in a MD domain is given. The same chapter introduces an orientation and ordering measurement method, previously used in the liquid crystals research field. New findings on the average orientation and ordering of water close to the walls and entrance of the CNT are presented. It is found that the application of an external static electric field can control the flow rate for a pressure driven flow through a nanotube membrane. Results in this chapter show that a localised field can increase water flow rate by more than 300% compared to the no-field case under the same pressure difference.

Water flow inside nanotube membranes is further studied in Chapter 4. In this chapter, the effect of different nanotube materials on the water flow rate is presented. A recently developed prediction model is directly compared with the simulation results. Valuable physical insight into water flow in nanotubes of different materials is gained through the various measurements performed during the MD simulations and the use of this model.

Chapter 5 is a review of multiscale methods including the Internal-flow Multiscale Method (IMM), a recent multiscale approach that is the most appropriate for simulating water flow in nanotube membranes.

In Chapter 6, the IMM is validated for water flow in nanotube membranes. In addition, computational results of very long systems are presented for the first time. A direct comparison with experimental results is attempted, and the expected flow enhancement limit is explored. Future improvements to the hybrid approach are suggested, as well as alternative approaches that could produce a more computationally efficient simulation tool.

The key findings of this research and a discussion of how the work can be advanced in the future are covered in Chapter 7.

1.3 Project objectives

The main objective of this thesis is to study the behaviour of water flow in nanotubes with molecular accuracy, identify the critical factors affecting it and propose methods to control the water flow rate without altering the external macroscopic conditions (i.e. pressure difference). It also focuses on the development and validation of hybrid multiscale approaches that can provide results directly comparable to experimental observations, while keeping computational cost at reasonable levels. Finally, macroscopic models, assumptions, and boundary conditions are revisited and tested at the nanoscale. If a macroscopic analytical or empirical equation can be used with acceptable accuracy levels, then the computational savings can be quite significant.

1.4 Molecular Dynamics simulations

Computational fluid dynamics (CFD) is a field extensively developed and used in order to perform numerical experiments avoidng the cost and risks the actual experiments contain. In a further extend CFD allows the study of phenomena taking place in extreme conditions where actual experiments are impossible to be performed or current measurement tools cannot operate and/or give accurate enough results. A significant number of CFD methods has been proposed, each one focusing in a specific application area. There are many ways to distinct and categorise CFD methods, either by the phase of the fluid (liquid *vs* gas), the spatial scale of the system under investigation (nano *vs* micro *vs* macro), or the nature of the computational solver (particle *vs* continuum/mesh methods).

The studied applications in this thesis have some specific characteristics that dictate the choice of the CFD method. The fluid under investigation is water, so the method should be appropriate for liquid flows. The size of the nanotubes is comparable to the size of the fluid molecules under investigation and the surface-to-volume ratio is very high. These two observations mean that any wall/surface induced effects cannot be neglected and the interaction of the fluid with the surface can have a profound influence on the flow characteristics in nanotubes. In addition, density fluctuations over interatomic distances are important at the studied scales, while they can be largely neglected at larger scales. Finally, transport properties such as the diffusion coefficient and viscosity are not equal to the bulk ones and they can vary significantly across the nanotube [16, 19, 20].

For the above reasons and to the best of the author's knowledge Molecular Dynamics (MD) is the most appropriate method to study water flow at the nanoscale. Multiple times in the past [21–29], the MD method has shown its ability to accurately resolve phenomena at the nanoscale, and specifically for liquid flow through nanotubes [18, 30–33]. This thesis takes advantage of previous developments and extends the applicability of MD to water flow in nanotube membranes, while unveiling and explaining phenomena that are observed for the first time. The basics of MD as well as a validation of the developed code and adopted parameters are presented in the next section.

1.4.1 Basics of MD

The MD simulation technique is a deterministic method, based on the simple idea of exploiting Newton's equations of motion linking forces with acceleration [34–37], viz.

$$\mathbf{F}_i = m_i \mathbf{a}_i, \tag{1.1}$$

i.e. the interatomic force $\mathbf{F}_i$ acting on atom i is equal to the atomic mass m_i multiplied by its acceleration $\mathbf{a}_i = d^2\mathbf{r}_i/dt^2$, where $\mathbf{r}_i$ is its position. If there are a total of N_{at} atoms in a system, the force acting on the i^{th} atom at a given time can be obtained from the interatomic potential $U(\mathbf{r}_1, \mathbf{r}_2, ..., \mathbf{r}_{N_{at}})$ that, in general, is a function of the positions of all the atoms:

$$\mathbf{F}_i = -\nabla_i U(\mathbf{r}_1, \mathbf{r}_2, ..., \mathbf{r}_{N_{at}}). \tag{1.2}$$

The time evolution of a system containing molecules with known interatomic interaction potentials and initial positions and velocities can then, in principle, be completely determined.

Every MD simulation starts with a large configuration of molecules, each consisting of one or more atoms, with known positions and velocities. Energy potentials, derived either empirically or through quantum mechanical methods, are used to compute the total force on each molecule. With the aid of Newton's law, Eq. (1.1), this force is converted to an acceleration, and with a numerical time integration algorithm (such as the Verlet or the Leap-Frog methods [36]), the position of each atom can be predicted, and consequently of each molecule, a small time interval later. So molecules will move, interact with each other, and evaporate away from the system, in a way very similar to the behaviour of molecules in a real substance. A small amount of uncertainty always exists when a MD simulation is performed due to the finite integration time-step and arithmetic rounding errors. The computed trajectory of the molecules will therefore always deviate from the true trajectory.

The choice of the interaction potential and its parameters therefore defines the accuracy and the realism of each representative substance and of the overall simulation. All of the applications presented in this thesis have been simulated using the mdFoam

code [38–41], a parallelised and GPU-accelerated non-equilibrium MD solver that is implemented within OpenFOAM [42], an open-source set of of C++ libraries for fluid dynamics simulations.

Molecular Dynamics could be criticised in that atomistic (and as a consequence molecular) movement and interaction should be based on quantum laws rather than classical ones, and that Schrödinger's equation is therefore the one to be followed. For a particle of mass m at temperature T, with h and k_B the Planck and Boltzmann constants, respectively, its de Broglie wavelength can be calculated [43]:

$$\Lambda = \sqrt{h^2 / (2\pi m k_B T)}. \tag{1.3}$$

According to this equation the classical Newtonian approximation is valid as long as the system under investigation does not consist of very light molecules (with small mass m), such as H_2, He or Ne. Additionally, quantum effects are important when the temperature T is sufficiently low. In other words, if a molecule's de Broglie wavelength Λ is of the same order or greater than its system's characteristic dimension (i.e. intermolecular distance $\approx \rho^{-1/3}$, where ρ is the system's density) then quantum effects are important [36, 44]. In all the examples presented in this thesis the systems contain heavier molecules, and simulations are performed close to standard room temperature, so the Newtonian-based MD is sufficient.

The thermodynamic properties and characteristic behaviour of a material cannot be observed in the individual trajectories of molecules. Through the use of statistical mechanics, physical quantities can be represented by averages over configurations distributed according to a certain statistical ensemble [44]. The most commonly used ensembles in MD studies are the microcanonical NVE, the canonical NVT and the isothermal-isobaric NPT. In these ensembles the properties referred to with capital letters are kept constant, i.e. the number of molecules N, the volume V, total energy E, temperature T, pressure P. The measurement of a physical quantity in MD simulations is simply obtained by the arithmetic average of various instantaneous values asssumed by that quantity during the MD simulation. Details of the measurement of specific properties in a particular region have been given in previous works by Borg [45] and Nicholls [46].

Through the use of statistical physics, these measurements link the microscopic behaviour with the experimentally-observable macroscopic thermodynamic properties. Theoretically, only in the limit of infinitely long simulation times is the phase space fully sampled, and in that limit this averaging process would yield the thermodynamic properties. In practice, MD simulations are always of finite time, and the user must be cautious in deciding if the sample is adequate or not (i.e. whether the system is at equilibrium and/or steady state). Beyond its original role of measuring the thermodynamic properties and evaluating physical quantities of materials, MD is nowadays used for a variety of other purposes. Characteristic examples include studies of non-equilibrium processes, and as a component model in hybrid multiscale simulations.

The key element in a MD simulation is the force calculation. A simulation is realistic only to the extent that the interatomic forces are similar to those that real molecules would experience when placed in the same spatial configuration. Forces are obtained as the spatial derivative of potential energy functions, depending on the positions of the molecules and its component atoms. In this thesis, only pair potential functions are considered, so the general $U(\mathbf{r}_1, \mathbf{r}_2, ..., \mathbf{r}_{N_{at}})$ can be substituted here by $U(r_{ij})$, where $r_{ij} = \|\mathbf{r}_i - \mathbf{r}_j\|$ is the interatomic distance between atoms i and j. The calculation of the forces on each atom is an $\mathcal{O}(N_{at}^2)$ operation and the most computationally time consuming aspect of a MD simulation.

As most potential energy functions approach zero quickly after a small distance and, in order to keep computation to a reasonable level, all MD textbooks [34, 36, 37] suggest the truncation of the potential at a relatively short range (r_{cut}), where the interaction energy is less than 2% of the energy well depth. The resulting discontinuity at r_{cut} affects both the apparent energy conservation and the actual molecular motion, with molecules separated by a distance close to r_{cut} sometimes moving repeatedly in and out of interaction range. Truncation is an integral part of the MD potential and large truncation radii or Ewald summation techniques [16, 36, 37] do not guarantee more accurate predictions. This has been highlighted in a recent publication by Angelikopoulos *et al.* [47] where uncertainty quantification studies of MD simulations of water-graphitic systems have been performed.

The discontinuity can be smeared out by changing the form of the potential function

slightly, although this must be done carefully. A common modification of a potential $U(r_{ij})$ is to shift it in a way that both energy and force are zero at r_{cut}, i.e.

$$U_{shift}(r_{ij}) = U(r_{ij}) - U(r_{cut}) - \frac{dU(r_{ij})}{dr}|_{r=r_{cut}}(r_{ij} - r_{cut}). \tag{1.4}$$

Another possible modification that involves the use of a cubic spline polynomial that interpolates smoothly and differentiably between the value of $U(r_{ij})$ at $r_{ij} = r_{cut} - \delta r$ (where δr is a small distance) and zero at r_{cut}. This approach confines the modification of the potential to the vicinity of r_{cut}.

Two potentials are used throughout this thesis for the interaction of atoms, namely the Lennard-Jones (LJ) 6-12 and Coulomb (Cou) potentials:

$$U_{LJ}\left(r_{ij}\right) = \begin{cases} 4\varepsilon\left[\left(\frac{\sigma}{r_{ij}}\right)^{12} - \left(\frac{\sigma}{r_{ij}}\right)^{6}\right] & \text{if } r_{ij} < r_{cut}, \\ 0 & \text{if } r_{ij} \geq r_{cut}, \end{cases} \tag{1.5}$$

$$U_{Cou}\left(r_{ij}\right) = \begin{cases} \frac{q_i q_j}{4\pi\varepsilon_0}\left(\frac{1}{r_{ij}} - \frac{1}{r_{cut}} + \frac{1}{r_{cut}^2}\left(r_{ij} - r_{cut}\right)\right) & \text{if } r_{ij} < r_{cut}. \\ 0 & \text{if } r_{ij} \geq r_{cut}, \end{cases} \tag{1.6}$$

where ε is the depth of the potential well, σ is the finite distance at which the interatomic potential is zero, q_i are q_j are the charges of atom i and j, respectively, and ε_0 is the vacuum permittivity equal to 8.854×10^{-12} $\mathrm{C}^2/(\mathrm{N\,m}^2)$. Force calculations due to Coulomb interactions are truncated at the same cutoff distance, $r_{cut} = 1.2$ nm, as the LJ interactions (which is chosen according to previous publications [18, 32, 48] and after performing a sensitivity test). This cutoff distance is used throughout this thesis unless stated differently for a specific case. The electrostatic interactions are also shifted as explained above, which offers adequate accuracy and significant computational savings compared to other methods [18, 32, 48, 49].

1.4.2 Validation of water model and MD code

Water is the fluid that is extensively studied in this thesis; it should be represented by a model that will reproduce its thermodynamic and physical properties with high accuracy. In all the simulations presented here the rigid TIP4P/2005 water model

is used [50–52] to model the condensed phases of water. Studies have shown that this model can reproduce major water properties, such as critical temperature and density, surface tension, shear viscosity and the phase diagram, more accurately than other commonly-used rigid models, such as the SPC/E, TIP3P, and TIP4P [51]. This TIP4P/2005 model consists of a LJ interaction potential at the oxygen atom site (O) with $\varepsilon_{OO} = 0.7749$ kJ mol^{-1} and $\sigma_{OO} = 0.31589$ nm, positive Coulomb charges at the two hydrogen sites (H) ($q_H = 0.5564$ e), and a negative charge at a massless site (M) ($q_M = -1.1128$ e), located a small distance away from O (see Fig. 1.1).

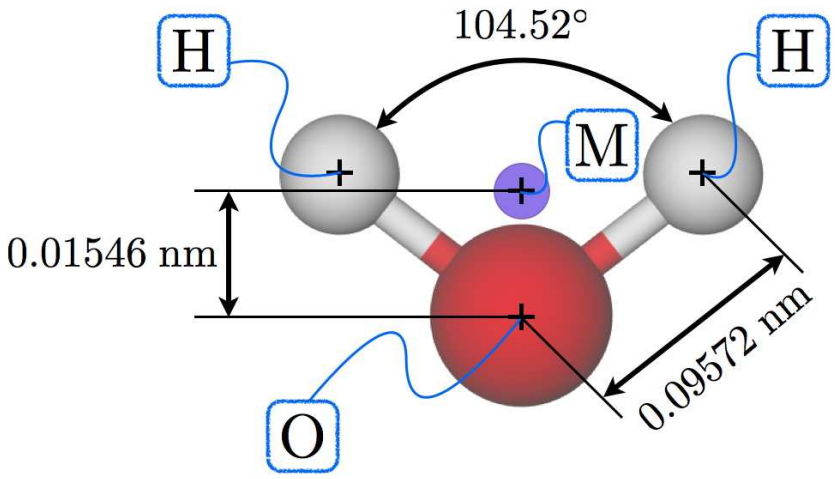

Figure 1.1: Graphical representation of the TIP4P/2005 water model. The oxygen atom site (O) of one water molecule interacts with oxygen atom sites from other water molecules through a LJ interaction potential. The hydrogen (H) and massless (M) atom sites interact through Coulomb interactions with charged atom sites of other water molecules. The massless site (M) will not be visualised in the rest of this thesis.

As mentioned in the previous paragraph, the TIP4P/2005 water model is rigid meaning that O-H bond and H-O-H angle vibrations are not considered. This approach has the advantage that a bigger time-step can be used and fewer interactions need to be calculated making the MD simulation much more computationally efficient. In addition, modelling quantum effects can be avoided — in a flexible model it is possible to object that hydrogen is a light atom and therefore treating the high frequency (see De Broglie's Eq. (1.3)) intramolecular movements with classical statistical mechanics is not justified.

One of the crucial benchmarks that any computer simulation or theory of water

must be tested against is the radial distribution function (RDF) $g(r)$. Although an isotropic fluid is characterised by the absence of any permanent structure, there are well-defined structural correlations that can be measured, both experimentally and computationally, through the RDF. In the case of spatially homogeneous systems the RDF can be calculated through the following relation:

$$g(r) = \frac{2V}{N_a^2} \left\langle \sum_{i<j}^{N_a} \delta \left(r - r_{ij} \right) \right\rangle, \tag{1.7}$$

where V is the volume of the system, N_a is the number of atoms over which the RDF measurement is performed, $\langle \, \rangle$ is the ensemble average and δ is the Kronecker delta. This function describes the spherically–averaged local structure around any given atom.

It is generally recognised that obtaining a reliable set of radial distribution functions for water is an essential prerequisite in any attempt to model and understand the properties of water and aqueous systems at the nanoscale. Most of the published computer simulations of water models make a comparison with experimental values of radial distribution functions [50, 52, 53]. Furthermore, when attempting to understand the effect of dissolved substances in water, it is essential to be able to compare the structure of the solvent (water in this case) in the presence of the solute with that of the pure solvent. This comparison is an important indication of how the solute-solute interaction may be modified when the solute is dissolved in water. A characteristic example is the study of Alejandre *et al.* [54] on crystal formation of ions in water and the parameterisation of the interaction parameters in order to reproduce the experimental phase diagram and radial distribution functions. Finally, the distinct hydrogen bonding between water molecules combined with the particular geometry of the water molecule gives rise to characteristic and unique forms for the OO, OH and HH radial distribution functions [55]. The average structure and orientation of water is therefore fundamentally important for characterising the nature of the hydrogen bond at the nanoscale.

Figure 1.2 shows a comparison of the radial distribution functions of pure water as measured using the TIP4P/2005 water model with experimental measurements from the study of Postorino *et al.* [56]. The simulation setup is a simple water box with

periodic boundary conditions equilibrated at 298 K with a density of 997.5 kg/m^3. The experiments are performed at the same temperature and an ambient pressure of 1 bar. The excellent agreement of the MD measurements with the experimental data enable the author to be confident regarding the accuracy of the selected water model and the methods applied in this thesis.

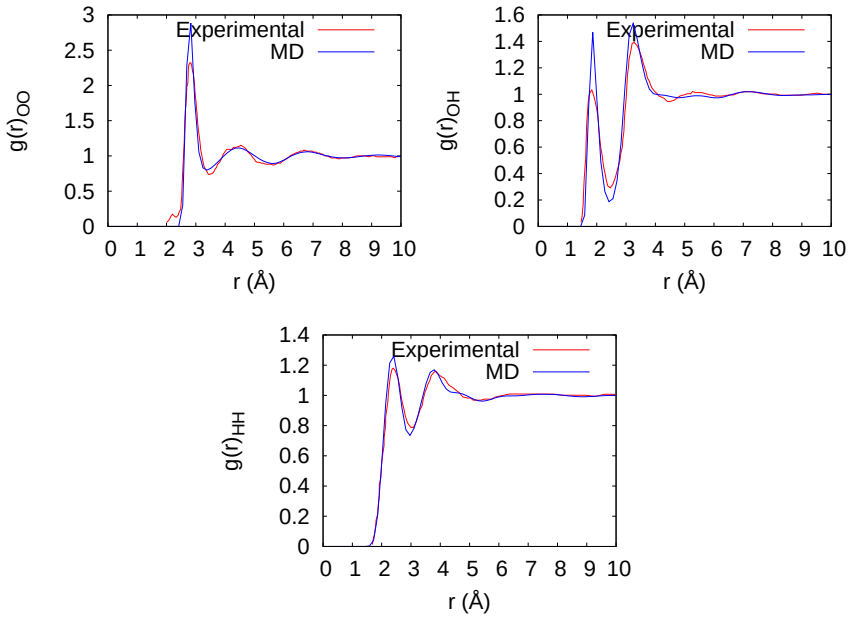

Figure 1.2: Comparison between experimental data of Postorino *et al.* [56] and measurements provided through using the TIP4P/2005 water model in mdFoam of site-site radial distribution functions.

Further, simulations of NaCl ions in water at high concentrations are performed. The methods and tools developed here should be able to simulate more complex systems that include saline water for desalination and filtration applications. Based on this, the ability to add ions to water without altering the water model and/or the interatomic potential parameters is of paramount importance.

Here, the interatomic potential parameters for ion-ion and water-ion interactions are those from the study of Alejandre *et al.* [54], where interatomic parameters are calibrated in order to reproduce saline water properties as measured in other experimental studies. Figures 1.3 and 1.4 present the site-site radial distribution functions for an over-saturated solution with a molality equal to 5.3 mol/kg. The system is initially equilibrated at 300 K with a water density of 997.5 kg/m^3 and the overall pressure is

around 1 bar.

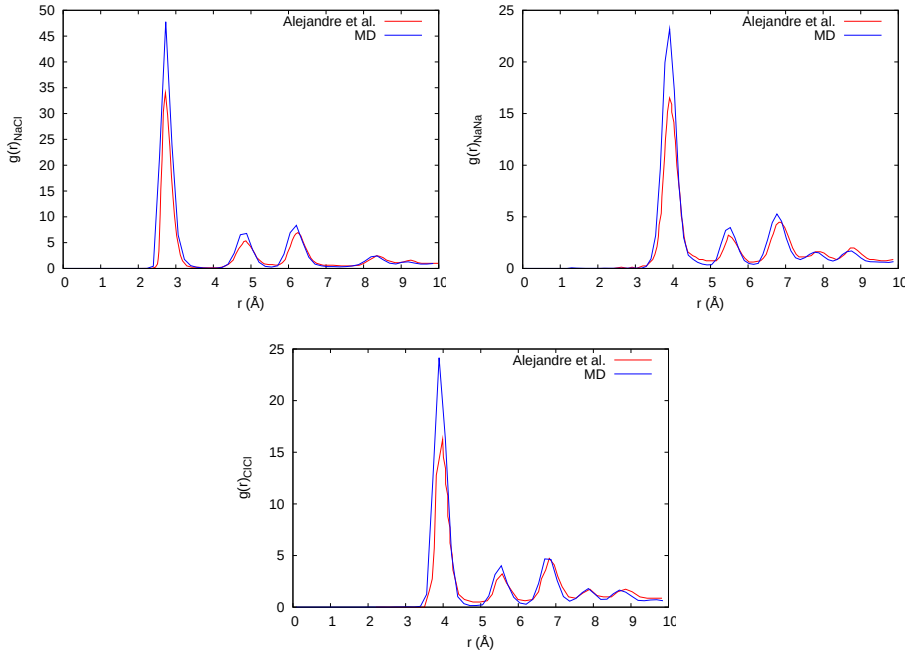

Figure 1.3: Comparison of ion-ion radial distribution functions given in the study of Alejandre *et al.* [54] and measurements provided by mdFoam. The TIP4P/2005 water model is used along with the ion-ion and ion-water interactions given in [54].

The formation of NaCl crystals, as expected in an oversaturated solution, is clear from the structured shape of g_{NaCl}, g_{NaNa} and g_{ClCl} as seen in Fig. 1.3. The qualitative agreement of the simulation results presented here with those in [54] is very good, and the differences in the magnitude of the first peak can be explained from the choice of simulation ensemble (NVE in the current simulation, and NPT in [54]). Other differences are due to the cut-off distance of the interaction potentials, the sampling radius, and the averaging and simulation times.

The results shown in Figs. 1.3 and 1.4 further validate the models, methods and computational code used in this thesis, through the simulation of a complex system where crystals are formed and dissolved. In all the applications presented in the following chapters, only pure water is considered. The study of ionic solutions could be a straightforward future extension, as all the necessary components and methods are already tested in terms of performance as well as validated for their accuracy.

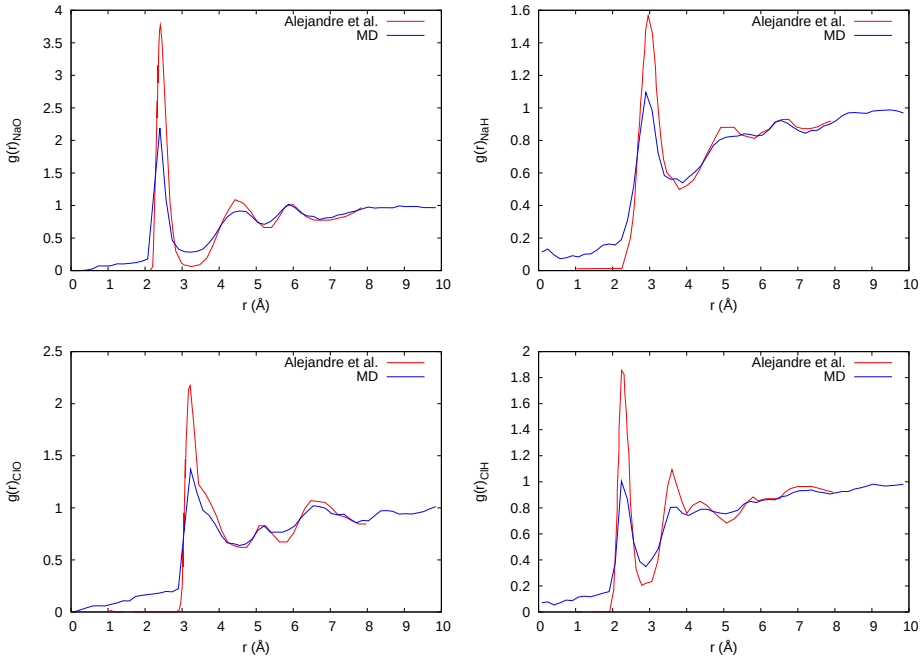

Figure 1.4: Comparison of ion-water site radial distribution functions given in the study of Alejandre *et al.* [54] and measurements provided by mdFoam. The TIP4P/2005 water model is used along with the ion-ion and ion-water interactions given in [54].

1.5 Key developments

All the computational models are developed and performed in a free and open source MD code which is parallelised and also able to run on Graphics Processing Units (GPUs). The solver is based on the MD code initially developed by Macpherson [57], and substantially extended in recent years by Borg [45] and Nicholls [46]. The source code and the solver are part of the Open Field Operation and Manipulation (OpenFOAM) C++ fluid dynamics toolbox [42]. All the developments reported in this thesis are made by the author or the author is a major contributor. These developments include the modelling of nanotubes made from various elements, and combinations of them, and is not restricted to CNTs. Another development is the extension of the pre-processing intialisation tool that enables the use of material input files, such as amorphous silicon dioxide (glass) and forms of ice. Further code development provides additional measurement, control and visualisation features. The main contributions of this work are:

- Validation of the TIP4P/2005 water model, NaCl ion-ion and ion-water potential

parameters, and the MD solver against experimental results and independent simulation data from previous publications.

- Calibration of the water–graphite interaction potential parameters in order to reproduce the macroscopic, experimentally observed contact angle.
- Development of measurement features for hydrogen bonding and radial distribution functios used during validation.
- A new static and dynamic contact angle measurement tool through the measurement of the density. The measuring region is able to follow the center of mass of the water nanodroplet — a significant feature for the dynamic cases where the nanodroplet's mobility is quite high.
- MD simulations of water nanodroplets on silicon and graphite, static and moving, surfaces. The analysis of the results shows a different behaviour depending on the hydrophobicity of the solid surface.
- Application of the Gaussian forcing method for pressure difference creation in simulated water-nanotube membrane systems. This pressure control method was initially applied in atomistic fluid MD simulations by Borg *et al.* [58].
- Validation and usage of the FADE density controller developed by Borg *et al.* [59] for water molecules.
- Development of a controller that applies a linear axial or radial electric field over a selection of molecules in the whole simulation domain or in parts of it.
- Extension of a method that calculates a complete description of ensemble molecular order, previously applied in the liquid crystals field. Development of a measurement tool for this in MD simulations.
- MD simulations of water flowing within a carbon nanotube membrane show that water exhibits biaxial paranematic liquid crystal ordering both within the CNT and close to its ends. Crucially, this preferred molecular ordering can be enhanced when an electric field is applied, affecting the water flow rate through the nanotube. The selective minimisation of the CNT entrance effects and significant

increase of the flow rate can be achieved by applying a spatially patterned electric field.

- Further development of the parallelised, pre-processing CNT and graphene initialisation tool in order to create nanotubes of different materials.
- Computational efficiency and major speed up of the performed simulations through the addition of GPU functionality in the MD solver.
- Performance of MD simulations of water flow in carbon, boron nitride, and silicon carbide nanotubes as a part of membrane. Alongside an analytical model, the results show that the flow enhancement depends on tube's geometric characteristics and the solid-liquid interactions.
- Validation and performance benchmarking of the hybrid IMM of Borg *et al.* [58, 60] for water–nanotube membrane systems.
- Confirmation of the flow rate enhancement limit for water flow in CNT membranes. This is achieved with a series of IMM simulations of CNT membranes with varying thickness from 50 nm up to 2 μm.
- First time comparison between the results of a hybrid molecular simulation (IMM) and an experimental study of water flow in CNT membranes with a thickness of 1 mm.

1.6 Published papers

The work from this thesis has contributed to the following peer reviewed research papers:

1. Konstantinos Ritos, Davide Mattia, Francesco Calabrò and Jason M. Reese. Flow enhancement in nanotubes of different materials and lengths, *The Journal of Chemical Physics*, 140:014702, 2014.
2. Konstantinos Ritos, Nishanth Dongari, Matthew K. Borg, Yonghao Zhang and Jason M. Reese. The dynamics of nanoscale droplets on moving surfaces, *Langmuir*, 29:6936–6943, 2013

3. Konstantinos Ritos, Matthew K. Borg, Duncan A. Lockerby, Spela Ivekovic, Yonghao Zhang and Jason M. Reese. Towards realistic multiscale molecular-continuum modelling of water flow through nanotube membranes, *66th Annual Meeting of the APS Division of Fluid Dynamics, 2013, Pittsburgh, USA*

4. Konstantinos Ritos, Matthew K. Borg, Spela Ivekovic, Duncan A. Lockerby and Jason M. Reese. Simulating flow in aligned nanotube membranes using molecular dynamics, *1st International Conference on Desalination Using Membrane Technology, 2013, Sitges, Spain*

5. Konstantinos Ritos, Matthew K. Borg, Nishanth Dongari, Yonghao Zhang and Jason M. Reese. Dynamic wetting on moving surfaces: A molecular dynamics study, *ASME 10th International Conference on Nanochannels, Microchannels, and Minichannels Proceedings, 2012, Puerto Rico, USA*

6. Konstantinos Ritos, Matthew K. Borg and Jason M. Reese. From hydrophobic to super-hydrophobic behaviour: A multiphase molecular dynamics study of water on nano-rough surfaces, *Summer school for Fast Methods for Long-Range Interactions in Complex Systems, 2011, Juelich, Germany*

Chapter 2

Water nanodroplets on solid surfaces

Στη συμβατική μας καθημερινή γλώσσα μιλάμε για γλυκό, πικρό, θερμό, ψυχρό, για χρώματα ενώ στην πραγματικότητα υπάρχουν μόνο άτομα και κενό.

- Δημόκριτος (460-370 π.Χ.)

Sweet exists by convention, bitter by convention, colour by convention; atoms and void alone exist in reality.

- Democritus (460-370 B.C.)

Wetting phenomena play an important role in diverse processes across the fields of physics, chemistry, and biology [61–63]. The physics of wetting phenomena for water droplets is of fundamental importance in the design of surfaces that can mimic natural surfaces [64–66]. A thorough understanding of solid-liquid interactions at a molecular level is also crucial to technological applications, including surface coatings, emulsions, oil recovery, and in microfluidic and nanofluidic applications [67–70].

The key experimental parameter describing the degree of wetting is the macroscopic static contact angle θ_∞, measured through the liquid L placed in contact with a solid S, at the contact line. This angle is directly related to the microscopic static contact angle θ_s that can be measured through MD simulations. Figure 2.1 shows the wetting of a graphitic surface by a water nanodroplet, along with the density isochores of the droplet and the measurement of θ_s. A detailed explanation of the measurement

procedure based on Fig. 2.1 follows in section 2.2. The extent to which a liquid wets a given solid, i.e. the wettability, has been a subject of much research over the past few decades, both theoretically and experimentally [71]. The wettability determines the equilibrium configuration of the system: if θ_∞ is zero, then the liquid is said to wet the solid completely and the solid surface is fully hydrophilic; if it is 180°, then the system is said to non-wet the solid and the surface is fully hydrophobic.

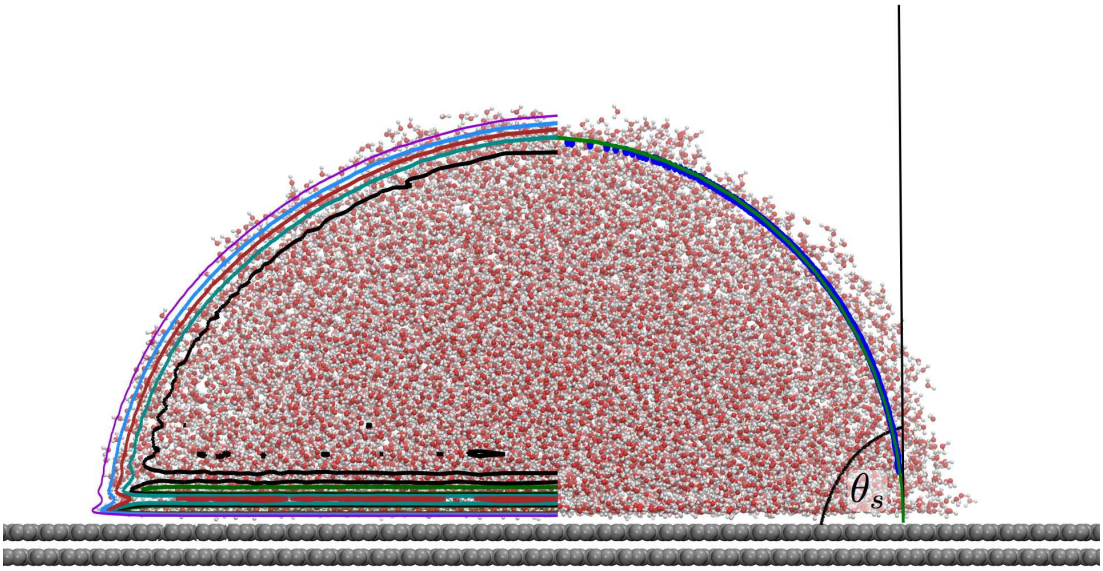

Figure 2.1: Equilibrated water droplet on a graphitic surface. Water molecules are represented by red and white spheres, which are the oxygen and hydrogen atoms respectively, while carbon is represented by grey spheres. Coloured lines over the left half of the droplet are density isochores. Blue circles on the right half of the droplet are the density isochore with half the bulk density. The green continuous line over the blue circles is a fitting of a circle equation. The black line is tangential to the circle equation where it meets the graphitic surface.

During the dynamic wetting process, in which the contact line moves across a solid surface, there may be several different modes of dissipation. For partially-wetting and non-wetting Newtonian liquids (and leaving aside dissipations within the main bulk of the liquid) the principal losses are viscous ones due to flow very near the contact line and contact-line friction associated with the creation (or loss) of the solid-liquid interface [72]. The actual physics that governs the wetting dynamics at the liquid-solid interface remains poorly understood [73, 74]. One reason for this is that the dynamics are dictated by physical phenomena taking place on different length scales. The large-scale dynamics are typically governed by hydrodynamic theory, while the movement of

the contact line itself is determined by processes on (or just above) molecular length scales. Another reason that dynamic wetting has remained unclear is that performing experiments and the associated measurements is quite difficult, with a large span in length scales and very rapid time scales [75].

There exist three principal theories for the description of dynamic wetting phenomena, namely, molecular-kinetic theory [72, 73], hydrodynamic theory [76, 77], and phase field theory [78–81]. Molecular-kinetic theory describes dynamic wetting as the disturbance of adsorption equilibria at the contact line. The movement of the contact line is determined by the statistical dynamics of the molecular motion within the three phase zone, where the solid, liquid and gas phases meet. Hydrodynamic theories are built on a continuum description and typically use the lubrication approximation involving either a microscopic cut-off length beyond which the solution is truncated, or a postulated region of local-slip between the liquid and solid. Another way to handle moving contact lines without violating the no-slip boundary condition is to apply the phase field theory, in which the contact line motion is due to diffusive interfacial fluxes. Its theoretical framework stems from a thermodynamic formulation [81], based on a description of the free energy in the system. Although all three theoretical formulations have been applied with some success, the models involve adjustable parameters that need to be determined through fitting experimental data. In addition, the applicability of these models to nanoscale droplet dynamics is questionable, as the exact nature of hydrophobic and hydrophilic interactions at the nanoscale remains elusive and controversial [62, 67–69].

Molecular dynamics simulations have been used extensively to study the surface wetting phenomena of nanoscale droplets [48, 82–99]. Microscopic equivalence of the contact angle has been casually applied to nanometer-scale droplets on a wide variety of surfaces (such as polymers, cellulose, silica, graphite and carbon nanotubes among others) in order to establish a connection between the microscopic calculations and the macroscopic wetting properties of the surfaces. The equilibrium macroscopic contact angle has been used as a reference for tuning the intermolecular interaction parameters. In most of the MD-based studies, the surfaces have been held frozen during these simulations to save computational time.

A common procedure for measuring the microscopic contact angle of a droplet on a surface is the fitting of a circle on the density profile as Fig. 2.1 shows. Sergi *et al.* [88] introduced an alternative approach to capture the droplet profile for the extreme case where very small droplets are not spherical and profiles cannot be described accurately by a circle. Their fitting procedure is based on local averages that approximate the profile of the droplet by a piecewise linear function. Their results highlight the influence of the water-wall interactions, especially for droplets with a base radius smaller than 3 nm. A completely different approach has been presented by Santiso *et al.* [89] where local normal vectors of all the molecules close to the solid surface are used to compose an average contact angle. For their test case they use coarse-grained water particles and their study pointed out once more the importance of size effects on the contact angle measurements.

Wang and Zhao [90] investigated the contact angle hysteresis of nanodroplets on both rigid and flexible substrates with different wettabilities, in response to a body force. Koishi *et al.* [91] and Savoy *et al.* [92] carried out simulations of the wetting characteristics of water and oil droplets, respectively, when placed on static pillar-type nanostructures. Similar studies were performed by Jeong *et al.* [93] by taking into account the effect of a body force on the water droplet behaviour. Dutta *et al.* [94] studied size and temperature effects on the wetting transition of water on graphite and boron-nitride surfaces.

Other recent studies on wetting phenomena and the dynamics of nanodroplets include the publication of Ambrosia *et al.* [95] which focused on the static behaviour of a water droplet on a graphite surface with different pillar heights and various pillar surface fractions. As an extension of this, Khan and Singh [98] also explored system size effects as well as the influence of fluid-surface interactions in a range of wetting states. Similarly, Jiang *et al.* [99] studied wetting and embedding on more realistic polymer pillared surfaces.

Previous MD investigations have examined the effect of temperature, size, surface physical chemistry, gravity-like forces and nanostructure effects on the wetting behaviour. However, none of these MD investigations have considered wall movement effects on the wetting dynamics of water droplets. The study of droplet dynamics on

a moving wall involves different physical mechanisms than a droplet moving due to gravity type forces. The conditions developed due to a moving wall are relevant to many industrial applications, such as slot bead, slot curtain, and roller coating methods [70, 100–102], and other experimental studies [103].

This chapter presents investigations on the interactions of water droplets with moving silicon and graphite surfaces at a nanometer length scale. Two different surfaces are studied, and their velocities are varied in order to gain insights into the correlations between the surface movement and the microscopic contact angle. Advancing and receding contact angles and contact angle hysteresis measurements are obtained at different capillary numbers for silicon and graphite surfaces. The structure of the nanoscale droplets is also studied by examining the water density profiles, water depletion layers and hydrogen bonding near both the hydrophobic (graphite) and hydrophilic (silicon) surfaces. Water droplet behaviour on a fictitious super-hydrophobic surface is also investigated under static conditions. The existence of a vapour-like depletion layer of water molecules near a super-hydrophobic surface is also discussed.

To study the static and dynamic wetting of water on stationary and moving surfaces, MD simulations of water droplets on smooth graphite, silicon and an artificial super-hydrophobic surface are performed. While silicon is a hydrophilic material, graphite is weakly hydrophobic. In the following, details of the MD parameters are given, along with details on how the dynamic contact angle, contact angle hysteresis, density profiles, hydrogen bond distribution, and line tension are measured from the numerical experiments.

2.1 Simulation details

For the study of dynamic wetting, at least 4 droplet simulations are performed for both graphite and silicon surfaces across a range of capillary numbers (Ca), from 0.01 to 10.0. The capillary number is given by

$$Ca = \frac{\mu u_S}{\gamma}, \tag{2.1}$$

where u_S is the solid wall velocity, $\mu = 0.855 \times 10^{-3}$ Pa s is the dynamic macroscopic viscosity of water, and $\gamma = 69.3 \times 10^{-3}$ N/m is the surface tension according to the detailed study of Vega and Abascal [51]. No forces are applied to the graphite or silicon atoms, but their distance relative to each other is kept fixed in order to represent an inert wall; solid atoms are only allowed to move as a bulk in the direction of the given velocity. It has been shown previously that fixing the solid atoms of a surface does not affect the contact angle of the droplets, but it does reduce the computational expense significantly [48]. The dimensions of the surfaces are $20 \times 20 \times 0.34$ nm and $38.018 \times 38.018 \times 1.5$ nm for graphite and silicon, respectively. The graphite consists of two staggered graphene sheets with an interlayer distance of 0.34 nm, while the silicon wall is constructed as a uniform crystallite. This silicon model is later adapted to represent a fictitious super-hydrophobic material by altering the interaction parameter ε only. The thicknesses of the solid surfaces are intentionally kept small, as additional layers of solid material are not expected to have a significant influence on the water due to the employed MD cutoff radius of 1.2 nm. A third layer of graphite would be at least 1.0 nm away from water molecules, and the interaction forces from this layer to the water molecules would be very close to zero. Periodic boundary conditions are applied in all directions of the simulation box which, in effect, means that the droplet lies on a surface of infinite extent.

All the simulations in this chapter are carried out for a problem-time of 1 ns, with an integration step of 2 fs. Measurements of the contact angle, density, and hydrogen bonding are averaged over a minimum of $500,000$ samples, which is sufficient to obtain accurate results within $\pm 1\%$ error. Before sampling begins, the simulations are run for 200 ps in order for the molecular ensemble to relax. During this relaxation time the system is coupled to a Berendsen thermostat at a temperature of 300 K, which is then removed for the remainder of the simulation and subsequent measurements. The sampling is performed in the microcanonical ensemble (NVE) with constant number of atoms, constant volume, and constant energy. The evaporation time of the smallest droplet simulated here is of the order of 100 μs [104], which is quite large compared to the simulation timescale.

For the graphite surface, 2000 water molecules are initially placed in a rectangular

lattice of dimensions $5.8 \times 6.2 \times 1.6$ nm. For the silicon surface, 5000 water molecules are placed in a $6.3 \times 3.8 \times 6.3$ nm rectangular lattice. This difference is necessary because the hydrophilic nature of the silicon surface means that a droplet of 2000 water molecules is insufficient to provide the necessary thickness for accurate contact angle measurement, as explained in the following section. Samples of the molecular trajectories and other measurements are stored every 0.2 ps. All the simulations presented here typically took approximately 5 days, using 4 and 8 cores of a parallel computer for the graphite and silicon surfaces, respectively.

2.2 Measurements

Water density isochore profiles are obtained from the MD simulation trajectories (see Fig. 2.1). To do this, the volume around the water droplet is divided into bins radially (r) from the centre of mass of the droplet, and also in the direction perpendicular to the solid surface (z). This results in a cylindrical binning, with the centre of mass of the water droplet as the reference axis origin. The bins have equal volume, and the average bin height is 0.05 nm.

In order to capture both the static and dynamic microscopic contact angles, the cylindrical binning follows the centre of mass of the water droplet at every timestep. In each bin the water density is calculated and, for the dynamic contact angles calculation, the binning cylinder is divided into two parts — one for the advancing part of the droplet and one for the receding part (depending on the direction of the imposed velocity of the wall). With the resulting density contour plots, a two-step procedure is followed in order to calculate the microscopic static contact angle (θ_s) or the advancing (θ) and receding (ϕ) microscopic dynamic contact angles, similar to that described in Ref. [105]. First, the liquid-vapour interface contour line is chosen as the one with half the density of bulk water. Second, a circular best fit is applied on these points and is extrapolated to the solid surface, where the contact angles θ_s, or θ and ϕ are then measured. Figure 2.1 shows the measurement of θ_s on a stationary surface, while Fig. 2.2 illustrates the microscopic dynamic contact angles θ and ϕ of a water droplet on a moving silicon surface. It should be noted that density contour points at a distance less than 0.8 nm from the solid surface are not taken into account during the fitting. This ensures that

any fluctuations at the liquid-solid interface do not affect the measurements. It was shown in previous studies that the choice of this distance has negligible effect on the measured contact angles [48].

On the graphite sheet, water does not spread very much, which leads to a hemispherical droplet formation with bulk water density at the centre of it, even with only 2000 water molecules simulated. However, water spreads much more on the hydrophilic silicon surface, which therefore requires 5000 water molecules to be simulated in that case. The difference between the two measured dynamic angles then represents the contact angle hysteresis ($H = \theta - \phi$). All density values, lengths and angles that will be presented in sections 2.4 and 2.5 are in reduced units, with a reference density of 952.03 kg/m^3, a reference length of 0.3154 nm, and reference angle equal to the static contact angle of each material (θ_s).

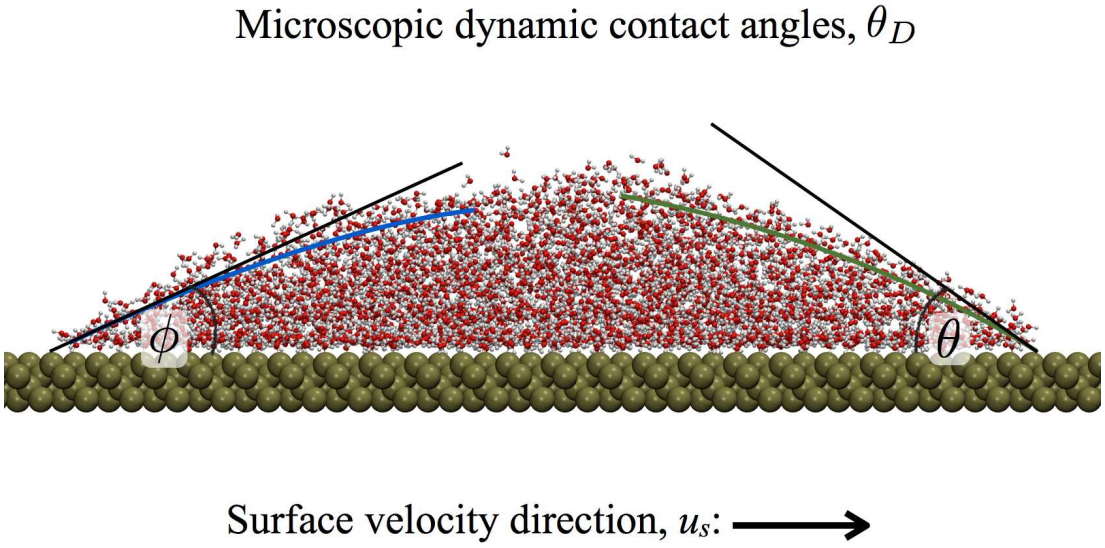

Figure 2.2: Equilibrated water droplet on a moving silicon surface. Water molecules are represented by red and white spheres, which are the oxygen and hydrogen atoms respectively, while silicon is represented by green spheres. The green and blue continuous lines are circular best fitting on the corresponding half density contour isochores. The black lines are tangential to the circle equations where they meet the silicon surface.

The distribution of hydrogen bonds (HB) in the droplet is calculated using a similar binning procedure as for the water density. The geometrical criterion of Luzar and

Chandler [106] is used to count the HB: two water molecules are considered to be hydrogen bonded if the oxygen and the hydrogen that form the HB are less than 0.35 nm apart and if the oxygen-oxygen/oxygen-hydrogen bond angle is less than 30°.

2.3 Water-graphite potential calibration

It has been mentioned in section 1.4.2 that the choice of the potential parameters is of paramount importance for any MD simulation. This section therefore presents new LJ parameters (σ_{CO} and ε_{CO}) for the interaction of the TIP4P/2005 water model with graphite. The calibration methodology is the one presented by Werder *et al.* [48]. Following this procedure, the author wishes to reproduce the desired macroscopic contact angle of a water droplet on a graphite surface, namely 86° [8, 107].

Size effects are important when the contact angle measurement is considered. Gibbs was the first to make a qualitative suggestion with the line tension τ concept [108]. He recognised the fact that the three-phase interactions at the contact line between a solid (S), a liquid (L), and a vapour (V) phase cannot be simply accounted for by the interfacial tensions of each pair of phases. The line tension refers to the excess free energy per unit length of the three-phase contact line, and it can be thought of as a one-dimensional analogue of the surface tension. Later, the effect of the line tension on wetting in a solid-liquid-vapour system was quantitatively expressed by the modified Young's equation [109, 110]. This equation correlates the microscopic contact angle θ_s to the macroscopic angle θ_∞ [111]. Under the assumption of a smooth, rigid, chemically homogeneous, insoluble, and non-reactive solid surface, the surface tensions γ of the relevant phases and the line tension τ can be related to the microscopic contact angle θ_s and the droplet base radius r_b,

$$\gamma_{SV} = \left(\gamma_{SL} + \gamma_{LV} cos\theta_s + \frac{\tau}{r_b} \right). \tag{2.2}$$

When macroscopic droplets are considered, i.e. for $1/r_b \to 0$, the macroscopic contact angle θ_∞ can be defined as $(\gamma_{SV} - \gamma_{SL})/\gamma_{LV}$. Then, the microscopic contact angle can linearly related to the macroscopic one and Eq. (2.2) can be rewritten as

$$cos\theta_s = cos\theta_\infty - \frac{\tau}{\gamma_{LV}}\frac{1}{r_b}. \tag{2.3}$$

The effect of a positive line tension is to contract the droplet base and to increase the contact angle, whereas a negative τ enhances wetting. The line tension will have significant effects on droplets with diameters below 10 nm, as it is believed to have a value on the order of 10^{-10} J/m [112]. In order to precisely determine τ, an accurate contact angle measurement is needed as well as the use of a highly purified liquid on an atomically smooth surface. These requirements are perfectly fulfilled in MD simulations, as is the necessary length scale.

An apparent method to determine the effect of the line tension in MD simulations is to measure θ_s and the contact line curvature $1/r_b$ for droplets of different sizes. Figure 2.3 presents the cosine of the microscopic water contact angle θ_s varying with the inverse of the base radius of the droplet $(1/r_b)$ as measured in this work by simulations of water droplets on a smooth graphite surface, with droplet sizes ranging from 1000 to 15000 water molecules. In all these cases, the LJ parameters used are $\sigma_{CO} =$

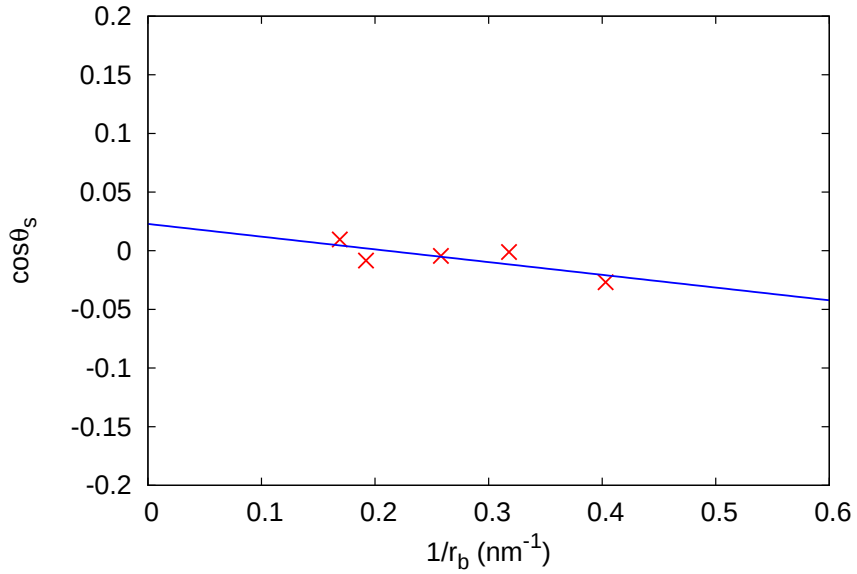

Figure 2.3: Cosine of the microscopic contact angle θ_s as a function of the droplet base curvature $1/r_b$. Red symbols are the results from MD simulations, while the blue line is a linear fit. These simulations were performed using a Lennard-Jones parameter of $\varepsilon_{CO} = 0.4119$ kJ/mol for droplets with an increasing number of water molecules on a smooth graphite surface.

3.19 $\mathring{A}$ and $\varepsilon_{CO} = 0.4119$ kJ/mol — this initial guess for ε_{CO} is taken from a range

of previously reported values for other water models, and can be considered as a good initial approximation as τ is not expected to vary significantly in a narrow range of ε_{CO}. Werder *et al.* [48] used previous studies to obtain their initial set of parameters and showed that a 40% increase in ε_{CO} lead to only a 12.5% change in τ. The coefficients of the linear fit in Fig. 2.3 can be used in Eq. (2.3) to calculate the line tension and the macroscopic contact angle θ_∞ — this resulted in $\tau = 0.752 \times 10^{-11}$ J/m and a macroscopic contact angle $\theta_\infty = 88.69°$ when the water model's surface tension is $\gamma_{LV} = 69.3$ mN/m as given in [51]. It is therefore apparent that the initial set of parameters used here is very close to the desired ones. Taking into account the calculated line tension τ and that a 2000 water molecule droplet has a base radius $r_b \simeq 3$ nm, the target value should be $\theta_s = 88.08°$ in order to reproduce the desired macroscopic contact angle $\theta_\infty = 86°$.

After studying the effect of the droplet size and calculating the line tension, the calibration of the interaction potential can be performed by studying the dependence of the contact angle on ε_{CO}. All the following simulations are performed on a 2000 water molecule droplet, with $\sigma_{CO} = 3.19$ Å, and seven different potential strengths ε_{CO}. In Fig. 2.4, the water contact angle θ_s for this range of different potentials is plotted against the binding energy ΔE of a water monomer on graphite. The linear fit to these data points has the following form:

$$\theta_s = 166.41° + \Delta E \cdot 14.01°(\text{kJ/mol})^{-1}. \tag{2.4}$$

An extrapolation of the fit to a vanishing interaction energy ($\Delta E = 0$ kJ/mol) between the water and the graphite leads to a microscopic contact angle of 166.41°, which is close to the expected value of 180.0°. Equation (2.4) can be used to predict the equilibrium microscopic static contact angle θ_s if the binding energy of a water monomer on graphite is known. In a similar way the water monomer binding energy can be adjusted in order to produce a prescribed contact angle.

The final step in this calibration procedure is to define a relation between the Lennard-Jones parameter ε_{CO} and the binding energy of one water molecule over a

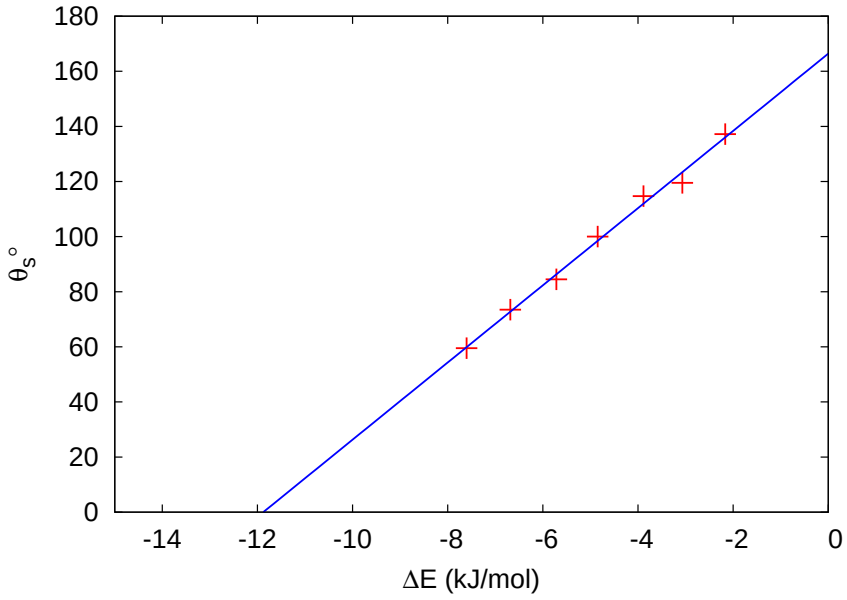

Figure 2.4: Microscopic water contact angle θ_s on graphite as a function of the binding energy ΔE of a water monomer. Red crosses are the measured microscopic contact angles θ_s from the MD simulations. The blue line is a linear fit to these points.

graphite surface. Figure 2.5 shows the relation for the set of simulated potentials with varying ε_{CO}. The linear fit to these data points produces the following equation:

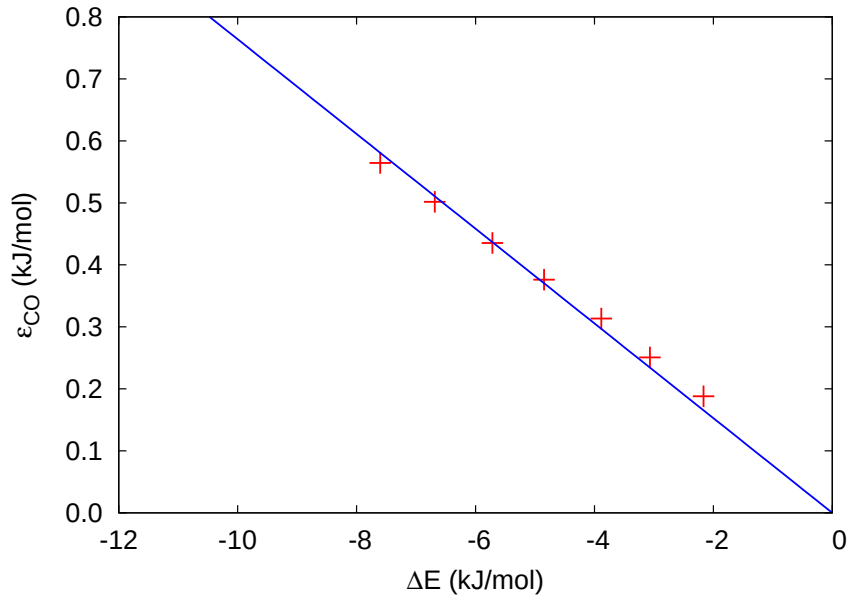

Figure 2.5: Linear fit to all data points of the Lennard-Jones parameter ε_{CO} varying with the water monomer binding energy ΔE on graphite.

$$\epsilon_{CO} = -0.07639 \cdot \Delta E. \tag{2.5}$$

The interaction potential parameter ε_{CO} can be calibrated by combining Eqs. (2.4) with (2.5) and using a target microscopic contact angle $\theta_s = 88.08°$, in order to achieve the experimentally measured macroscopic contact angle of 86°. Using this set of parameters in a system with 2000 water molecules on graphite, $\varepsilon_{CO} = 0.427$ kJ/mol corresponds to $\theta_\infty = 86.7°$ deviating from the intended target value by less than 1%.

The fitted parameters, the microscopic contact angle and, most importantly, the calculated ε_{CO} parameter differ significantly from those Werder *et al.* [48] presented for the SPC/E water model. This variation in the results is expected for different water models as they produce different bulk water energy. This underlines the importance of using the proper interaction parameters when a different water model is used. The same LJ parameters can then be used for simulations of TIP4P/2005 water flowing through or over carbon nanotubes.

For all the simulations in this chapter, the water-surface interaction is solely based on a Lennard-Jones potential between the oxygen atom of the water molecule and the carbon or silicon atoms of the surface. The LJ values of $\sigma_{CO} = 0.319$ nm and $\sigma_{SiO} = \sigma_{fiO} = 0.323$ nm are employed for all of these simulations, following the Lorentz-Berthelot mixing rules, previous studies [48, 113, 114] and the above analysis. The LJ interaction parameters $\varepsilon_{CO} = 0.427$ kJ mol^{-1}, $\varepsilon_{SiO} = 2.36$ kJ mol^{-1} and $\varepsilon_{fiO} = 0.139$ kJ mol^{-1} have been chosen in order to reproduce the macroscopic static contact angle θ_∞ of the simulated water model on the selected surfaces, namely 86° for graphite [107], 43° for silicon [115], and 150° for the fictitious super-hydrophobic material, respectively.

2.4 Nanoscale droplets on static walls

Qualitative observations on the droplet behaviour are made before discussing the quantitative results. Figures 2.6 and 2.7 show typical snapshots and density contours, respectively, of water droplets at their steady state on three different static surfaces: (a) silicon, (b) graphite sheet, and (c) the artificial super-hydrophobic surface. In

Fig. 2.6 the water molecules comprise red (oxygen) and white (hydrogen) atoms, the solid surface molecules are in brown (silicon), grey (graphite), and green (artificial super-hydrophobic surface). The water droplet relaxes from its initial rectangular configuration to roughly a capped spherical shape within the first 100 picoseconds in each simulation, and remains so for the rest of the simulation. The shape of the droplet at equilibrium is almost flat on the silicon surface, and hemispherical on the graphite. The water droplet adopts a near-perfect spherical shape on the artificial super-hydrophobic surface, and completely non-wets the surface from the molecular point of view. It can be also observed that the position of the water droplet remains almost unchanged during the simulation with the silicon surface, while the droplet becomes more mobile laterally as the hydrophobicity increases. From the density contours in Fig. 2.7, static microscopic contact angles for the silicon, graphite and the artificial super-hydrophobic surfaces are $\theta_s = 26.8^\circ$, 88.8° and 180°, respectively.

Figure 2.8 shows the density profiles of water droplets on the three different surfaces along the direction normal to the surface (i.e. the z-direction). The nanoscale droplet completely spreads on the silicon surface, which results in local oscillations in the density profile without reaching a constant value in the bulk. Oscillations around the bulk value for the first two or three hydration shells from the surface reflect a high degree of spatial ordering of water molecules in this region. A density higher than the bulk value for $z < 0.95$ also implies that the first water layer may form a relatively tight boundary at the interface. The water density profile on the graphite surface follows the same trend as the silicon for $z < 0.95$. At larger distances from the surface, the water density levels off to the uniform bulk density, which is a typical indication of a random isotropic distribution of the molecules. For the case of the super-hydrophobic surface, water molecules are not seen at all up to $z = 10$, although for higher values of z the density increases monotonically to reach its bulk value.

The water depletion layer, which is defined as the vertical region between the surface and the height where the water density falls below half the bulk density, can also be evaluated from Fig. 2.8. The depletion layer thickness is negligible: less than 0.95 for both the silicon and graphite surfaces (around the size of two water molecules). This is consistent with the results of other recent studies, which show that the thickness of the

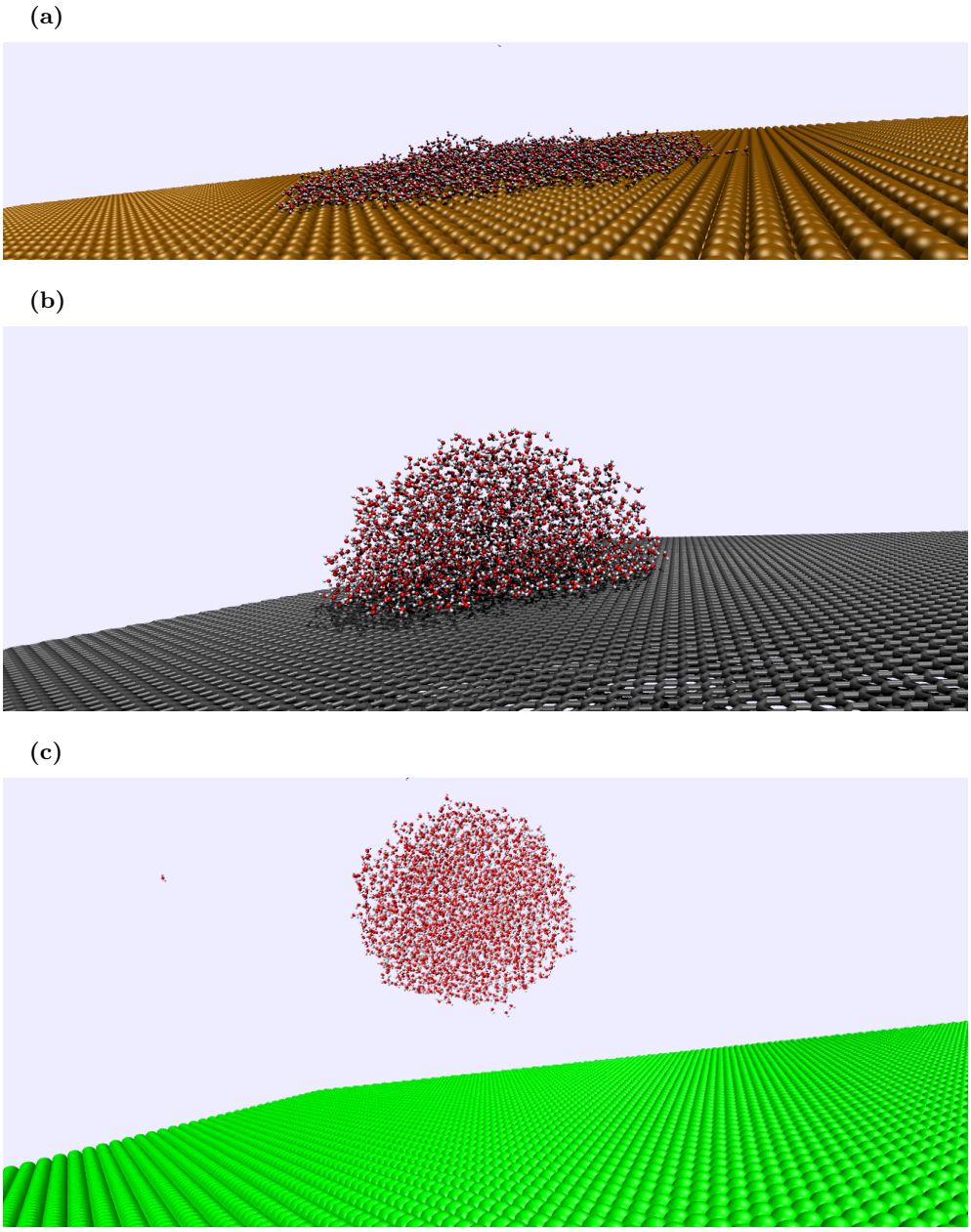

Figure 2.6: Typical snapshots of MD simulations of water nanodroplets at their equilibrium state on three different surfaces: (**a**) silicon, (**b**) graphite, (**c**) artificial super-hydrophobic wall. The atoms comprising the water molecules are shown in red (oxygen) and white (hydrogen), while the solid surface atoms are in brown (silicon), grey (graphite) and green (artificial super-hydrophobic surface).

depletion zone can be a few angstroms for both hydrophilic and weakly hydrophobic surfaces [116]. However, for the super-hydrophobic surface, the thickness of the water depletion layer is found to be around 12, which is well outside the water-solid molecular interaction range. In other words the water-wall molecular interactions are so weak

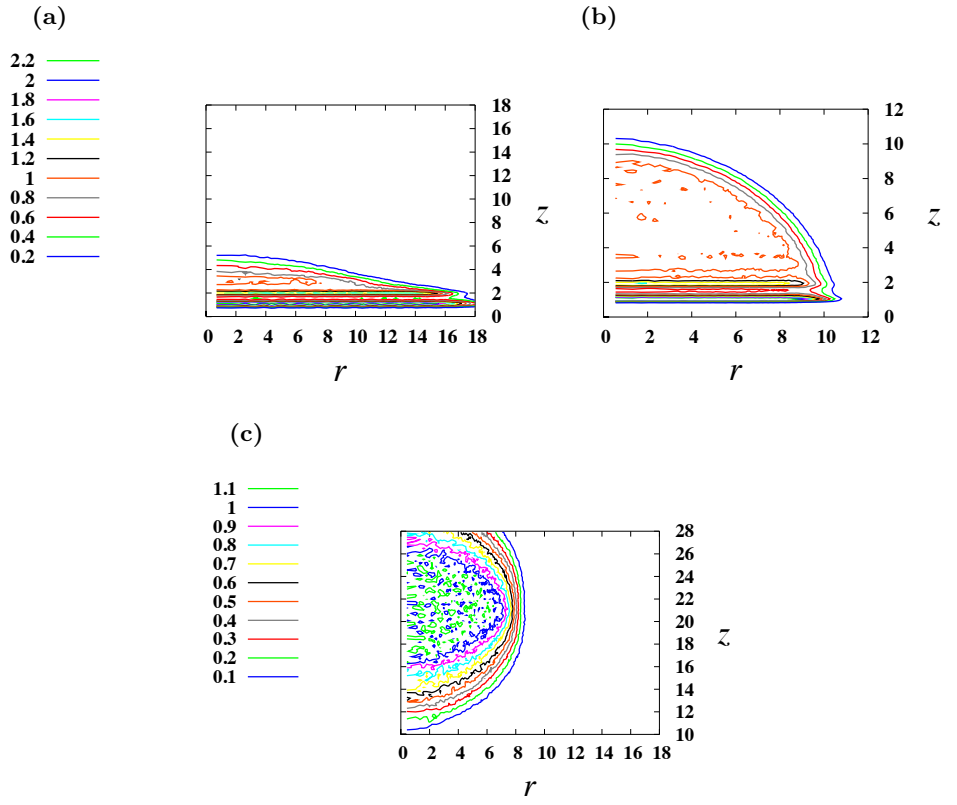

Figure 2.7: Density contours of water droplets (due to symmetry only half droplets are shown) at their equilibrium state for (**a**) silicon, (**b**) graphite, (**c**) artificial super-hydrophobic surfaces. Figures (**a**) and (**b**) share the same legend. All quantities are labelled in reduced units. Static microscopic contact angles are evaluated when the solid surfaces are at rest.

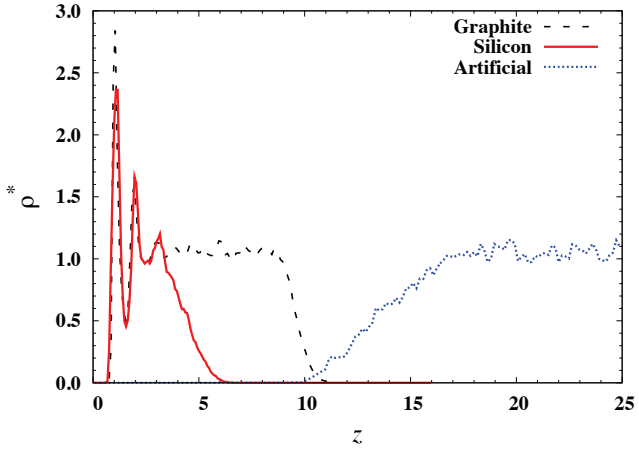

Figure 2.8: Water density varying with the normal distance from the surfaces (z-direction), through the centre of mass of each droplet on different surfaces ranging from hydrophilic to hydrophobic. Density ρ^* and length z are in reduced units.

that the water droplet can move away from the wall. This depletion layer causes liquid droplets to effectively slip over strongly hydrophobic surfaces, and is observed experimentally [117]. In general, the existence of a vapour like layer near the interface is more likely for a super-hydrophobic surface. Once the nucleation barrier is exceeded, either an incipient depletion layer is formed on the solid surface or, in more realistic conditions, gas molecules can be trapped in the gap between the liquid and solid layers. This effect acts to prevent the liquid from being directly exposed to the wall surface. In such cases, the liquid is not likely to experience the presence of the wall directly and may smoothly "sail over" the intervening depletion layers, instead of being in proximate contact with the wall.

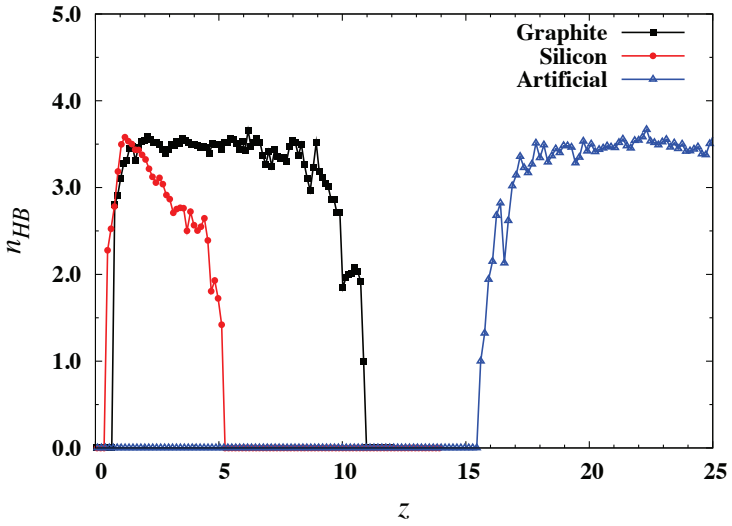

Figure 2.9: The average number of hydrogen bonds per water molecule n_{HB} along the direction z normal to the surface, for the different surfaces.

Figure 2.9 shows the average number of hydrogen bonds per water molecule n_{HB} along the direction normal to the surface, for the different surfaces. The profiles for silicon and graphite surfaces reveal that the first peak in n_{HB} is located between the first and the second peaks in the water density profile (see Fig. 2.8). The number of hydrogen bonds drops quickly near the surface as the very first layer of water molecules cannot form hydrogen bonds in the direction towards the surface. The rise in the number of hydrogen bonds between the first and second layer of water molecules indicates a locally tight structure of these two water layers. For the artificial super-hydrophobic surface case, the number of hydrogen bonds per water molecule is shown to be zero up

to a distance of 15 and then increases before reaching its constant bulk value.

2.5 Nanoscale droplets on moving walls

As mentioned in section 2.3, size effects are important when contact angle measurement is considered. The modified Young's equation (see Eq. (2.3)) [111] correlates the microscopic dynamic contact angles θ and ϕ (or denoting θ_D for a microscopic dynamic contact angle) to the macroscopic ones θ_∞ and ϕ_∞, respectively. In the following figures and results, the contact angles are always the microscopic ones.

All the competing forces during dynamic wetting are introduced at this point in order to help the reader understand the different mechanisms involved in that process. These equations form a qualitative analysis and additional simulations and measurements should be performed in the future. The first type of forces that is present on both static and moving droplets is the surface tension:

$$\mathbf{F}_{st} \sim \gamma. \tag{2.6}$$

This force is not affected by the motion of the solid wall and is constant throughout the following numerical experiments. The second type is the viscous force induced by the moving wall onto the water droplet, and also between the water layers;

$$\mathbf{F}_{vis} = \mu A \frac{du_r}{dz}, \tag{2.7}$$

where μ is water's viscosity and A is the contact surface area between two interfaces (e.g. solid-liquid and liquid-liquid). This force is highly affected by the capillary number and intermolecular interactions which define slip effects on the various interfaces. If the water droplet is moving as a bulk, and there is high slip velocity between the first water layer and the solid wall, then this force can be considered negligible. Finally, inertial forces can be significant for high solid wall velocities:

$$\mathbf{F}_{iner} = (1/2)\rho u_S^2 A, \tag{2.8}$$

where u_S is the velocity of the wall and ρ is the density of the water droplet. Both viscous and inertial forces depend on the contact area, meaning the size of the water droplet. This is why in the case of nanodroplets these forces are expected to play a minor role.

Figure 2.10 presents the variation of the normalised advancing (θ/θ_s) and receding (ϕ/θ_s) dynamic contact angles with capillary number (Ca), for water droplets on moving silicon and graphite surfaces. The majority of the dynamic angles measured on the moving silicon surface (Fig. 2.10a) are smaller than the static one (θ_s). For Ca rising from 0.01 to 0.1, the advancing normalised angle reduces from 1.04 to 0.78. It then increases to 0.93 by $Ca = 0.2$ and then decreases slowly with further increases in Ca. The receding normalised angle increases from 0.88 to 1.02 as Ca increases from 0.01 to 0.025, but for higher values of Ca it fluctuates between 0.85 and 0.95. On the other hand, Fig. 2.10b indicates that the contact angle of nanoscale droplets on graphite surfaces does not show a large variation with the capillary number. Independent of the velocity of the graphite wall, both the dynamic advancing and receding contact angles are close to the static contact angle value.

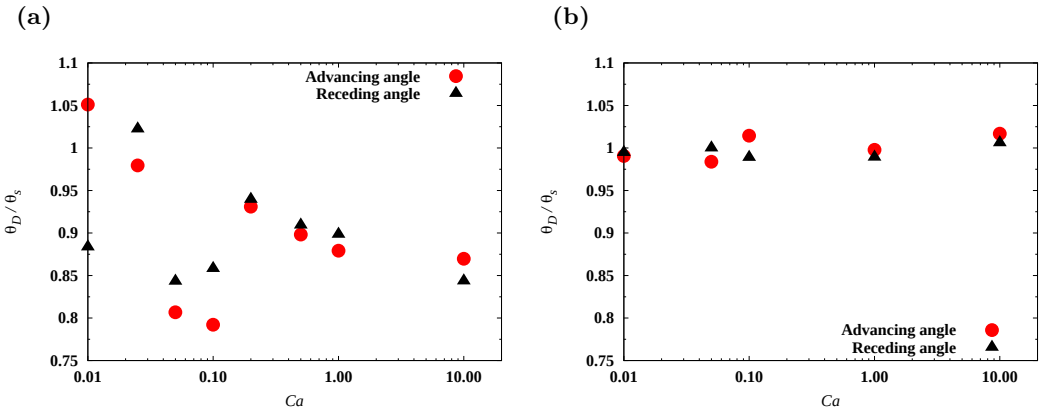

Figure 2.10: Variation of the normalised advancing and receding dynamic contact angles (θ_D/θ_s) with capillary number (Ca), for water droplets on moving surfaces: (**a**) silicon $(\theta_s = 26.8^\circ)$ and (**b**) graphite $(\theta_s = 88.8^\circ)$.

Figure 2.11 shows the normalised contact angle hysteresis ($H = \theta - \phi$) variation with Ca for water droplets on moving surfaces. Normalised hysteresis values for the graphite surface are close to zero, with only small fluctuations. For the silicon surface, however, normalised hysteresis values decrease from 0.17 to -0.07 as Ca increases from 0.01 to 0.1, and they increase to 0.02 with further increase in Ca.

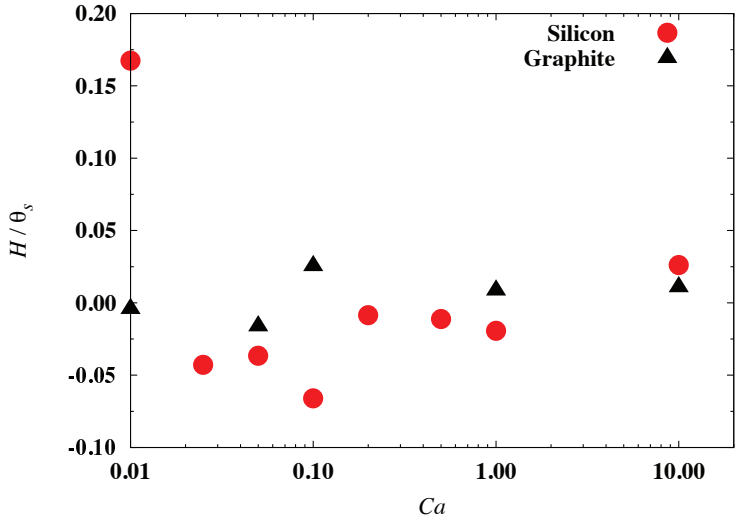

Figure 2.11: Normalised contact angle hysteresis (H/θ_s) variation with capillary number (Ca) for water droplets on moving silicon and graphite surfaces.

For the silicon surface, Fig. 2.10 and Fig. 2.11 indicate that the Ca range can be classified into three distinctive regimes: the first for Ca smaller than 0.1, the second for values between 0.1 and 0.2, and a third for higher Ca values. In the first regime, surface tension forces dominate over viscous stresses that are induced through the boundary movements. In the second regime, both viscous and inertial forces are equally important and stronger than surface tension forces, and in the third regime inertial forces dominate both the surface tension forces and the viscous forces. For the graphite surface, molecular displacements at the contact line are purely influenced by interactions with the solid surface (i.e. surface tension forces), and both the viscous dissipation effects and inertial forces are negligible.

Figures 2.12 and 2.13 show the normalised water density profiles with the normalised distance from the surfaces (the z-direction) for silicon and graphite, respectively. In the case of silicon, the profiles are nearly identical for all capillary numbers. However, deviations can be noticed around the first peak in the density profiles as shown in

Fig. 2.12b. At a given z, in the range $0.01 < Ca < 0.1$, density increases with an increase in Ca, while it decreases for $Ca > 0.1$. Denser packing of water molecules in the first layer causes a relatively tight boundary at the interface, which may lead to a decrease in the contact angle. This finding is also consistent with the measurements in Fig. 2.10a, where the contact angle decreases from $Ca = 0.01$ to 0.1 but increases with further increase in Ca. In the case of graphite, the density profiles are negligibly affected by variations in the capillary number, although minor deviations can be noticed around the first peak and trough.

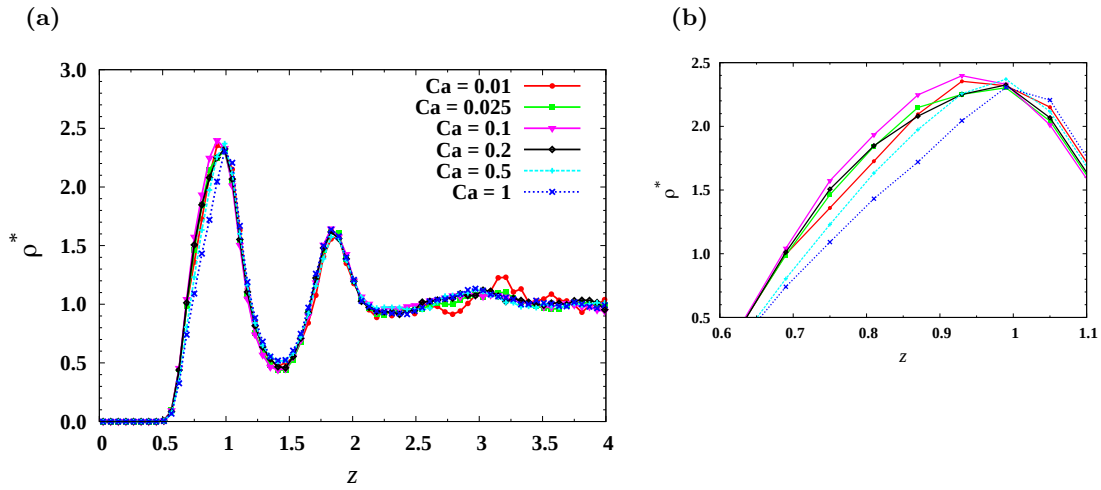

Figure 2.12: (**a**) Water density varying with distance from the surface (z-direction) through the centre of mass of the droplet, for a silicon surface, for various capillary numbers; (**b**) close-up of the first density peak. Density ρ^* and length z are in reduced units.

Figures 2.14 and 2.15 show the average number of hydrogen bonds per water molecule along the direction normal to the silicon and graphite surfaces, respectively. For silicon, there are no hydrogen bonds up to a normalised distance of 0.35 from the surface. For $Ca = 0.01$, the number of hydrogen bonds then increases monotonically to its bulk value. For the $Ca = 0.025$, 0.05 and 0.2 cases, however, a rise in the number of hydrogen bonds is seen before the first layer ($z < 0.8$) of water molecules (see Fig. 2.14b). This means a relatively tighter binding of water molecules with the surface through the extra hydrogen bonds in this near-wall region. This may lead to better wetting conditions for water droplets and a decrease in the contact angle. A further increase in Ca leads again to a monotonic increase in the number of hydrogen bonds to its bulk value, without any local peak near the surface. In the case of graphite,

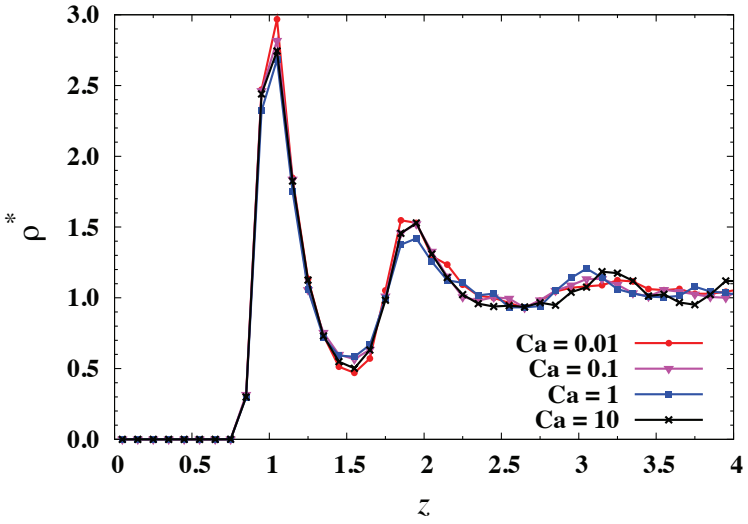

Figure 2.13: Water density variation with distance from the surface (z-direction) through the centre of mass of the droplet, for a graphite surface, for various capillary numbers.

Fig 2.15, the number of hydrogen bonds is zero up to a normalised distance of 0.7, i.e. twice that for the silicon surface. This means there are poor wetting conditions near the surface, irrespective of the capillary number. Viscous forces have a negligible effect on the number of hydrogen bonds in both the first and second layers (i.e. $0.8 < z < 2$) of water molecules, and in the bulk region ($z > 2$).

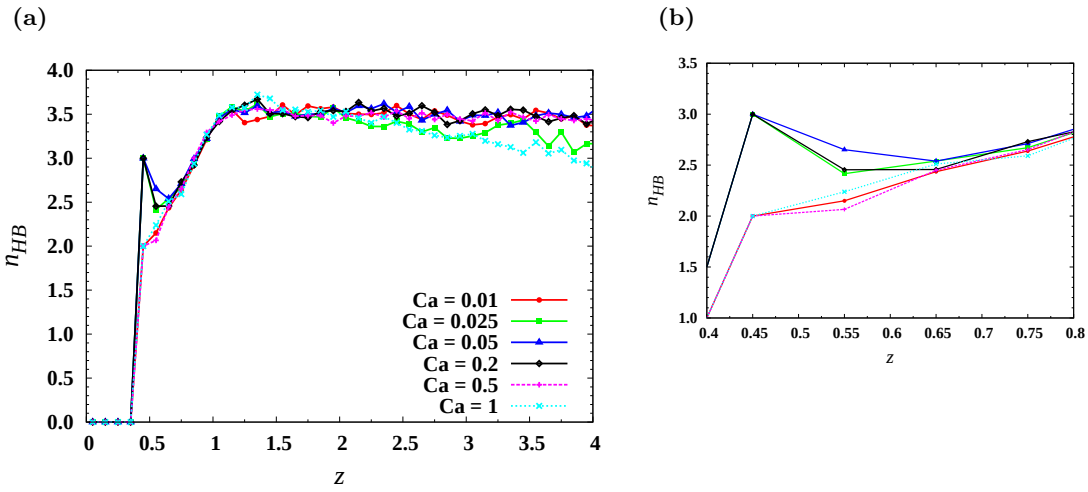

Figure 2.14: (**a**) The average number of hydrogen bonds (n_{HB}) per water molecule along the direction normal to the silicon surface for various capillary numbers. (**b**) Close-up of the region around the first non-zero value for n_{HB}.

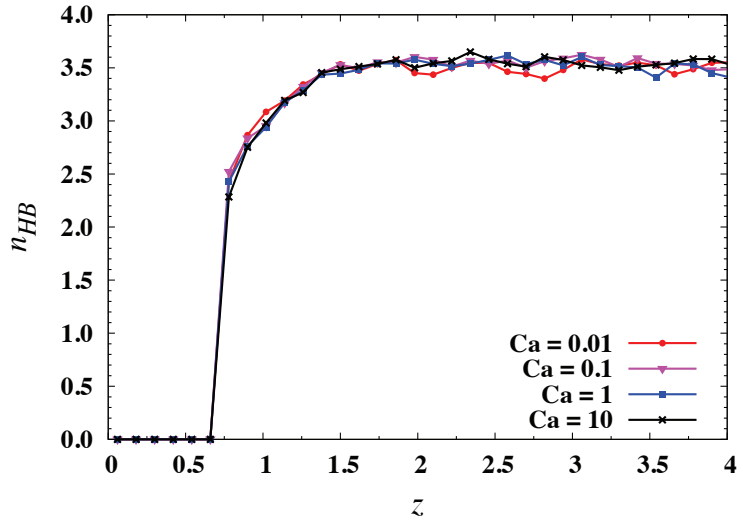

Figure 2.15: The average number of hydrogen bonds per water molecule along the direction normal to the graphite surface for various capillary numbers.

2.6 Summary

This chapter presented the calibration of the interaction potential between the TIP4P/2005 water model and a graphitic surface. It showcased the importance of size effects when measuring the wetting contact angle of nano-droplets. In addition, it showed that interaction parameters calibrated for one water model should not be used with other water models without further validation.

Molecular Dynamics simulations of nanoscale water droplets on different static and moving surfaces were then presented. Silicon, graphite and an artificial material modelled hydrophilic, and weakly and strongly hydrophobic surfaces, respectively. Water density and hydrogen bonding profiles were extracted from the simulations, and both the effect of solid-liquid interactions on the formation of water depletion layers and the cohesive strength of water molecules was discussed. A large depletion layer is formed near the super-hydrophobic surface, primarily because water molecules next to a super-hydrophobic surface have significantly fewer hydrogen bonds, and as a result the cohesive strength of the water is reduced.

Finally, the effects of solid-liquid interaction and viscous dissipation were also investigated by moving the silicon and graphite surfaces. This type of dynamic wetting, which is relevant to a range of industrial applications, was investigated for the first time with the use of MD. It was found that, for nanoscale droplets, the solid-liquid interac-

tions play a vital role in determining the wetting dynamics, while viscous dissipation effects induced by the moving surface were found to be only slightly important for the silicon surface and negligible for the graphite surface. These observations are different from the wetting dynamics of macroscale droplets, which show a significant dependence on the capillary number. For a silicon surface, the advancing contact angle initially decreases with an increasing capillary number through $0.01 < Ca < 0.1$, then there is a significant increase for $Ca = 0.2$ and finally it slowly decreases for $0.2 < Ca < 1$. In the first regime, surface tension plays a key role, while in the latter both viscous and inertial forces are important. In the case of the graphite surface, solid-liquid interactions play the major role irrespective of capillary number.

Chapter 3

Water orientation and structure in carbon nanotubes

Όλοι οι άνθρωποι από τη φύση τους επιθυμούν την γνώση.
- Αριστοτέλης (384-322 π.Χ.)

All men by nature desire knowledge.
- Aristotle (384-322 B.C.)

Recent advances in material science have meant that the study of water within carbon nanotubes (CNTs) is a fast growing research topic [118]. In particular, computational and experimental studies of water flow inside aligned CNT membranes have shown the potential for creating filtration membranes with very promising capabilities [9]. Very narrow CNTs, of around 0.8 nm diameter, have attracted particularly strong interest as they resemble biological water channels such as aquaporins, proton pumps, and protein cavities in Lysozyme or Alzheimer's Aβ amyloids. The filling process, and the structure and orientation of water inside this type of nanotube has therefore been studied extensively, both with and without electric fields present [119–121]. In these narrow channels, the simple one-dimensional chain of water molecules can be represented as a hydrogen bonding network.

However, this thesis focuses on wider nanotubes, with a diameter of around 2.0 nm, where up to 6 water molecules can be accomodated across the diameter. In such systems, a high density, structured outer layer is formed close to the CNT walls, while

toward the centre of the tube the water exhibits bulk behaviour. The near-wall layer seems to be the key to the high flow rates observed in previous studies [19, 122, 123], as water can easily slip over the solid surface with minimal friction losses. These wider nanotubes resemble other important biological channels, such as the protein cavity inside tetrabrachion [121], ion channels [124], and orifices created by membrane electroporation [125].

Using Molecular Dynamics (MD), the behaviour and properties of water are simulated under this type of nano-confinement. The characterisation of water is extended beyond the usual dipole moment, and a new measurement method is introduced that uses two order tensors **Q** and **B**, often used in the theory of liquid crystal ordering. This method enables a fuller description of a system of biaxial molecules such as water [126, 127]. In section 3.1 these order tensors are defined, along with details on how they are constructed and the useful information they provide in addition to existing measurement methods.

The use of these order tensors enables the elucidation of the effect of static electric fields on the average orientation and packing of water inside aligned CNT membranes. It is observed that a rise in anisotropy is correlated to the flow rate of the water through the nanotube. It is also demonstrated that the application of an external electric field close to the entrance of the membrane preorders water molecules before they enter the CNT, significantly decreasing the entrance losses and consequently increasing the flow rate through the nanotube for the same applied pressure difference.

3.1 Water, liquid crystals and order tensors

The liquid crystal phases of matter have properties between the crystalline solid and isotropic liquid states. For instance, the calamitic nematic liquid crystal phase consists of elongated molecules with no positional order (as in an isotropic liquid) but which, on average, point in one direction (as in a typical crystal structure). This nematic phase can have two sub-phases: the uniaxial phase (the simplest and most commonly observed) and the more recently discovered, and still disputed, biaxial phase [128–130]. In the uniaxial nematic phase the molecules can be thought of as, at least on average, elongated rods that tend to align along a single direction, termed the director and

denoted by a unit vector $\mathbf{n}$, which forms an axis of complete rotational symmetry. In the biaxial nematic phase the molecules order so that there is no axis of complete rotational symmetry, and an orthogonal triad of directors $\mathbf{n}$, $\mathbf{l}$ and $\mathbf{m}$ must be specified to describe the local average molecular configuration. If there are no external forces, the orientational symmetry group of the phase is a subset of the orientational symmetry group of the constituent molecule. So uniaxial molecules (i.e. a linear arrangement of atoms) must form a uniaxial nematic phase, if a liquid crystal phase is formed at all.

It might be expected that a biaxial phase is more likely to be formed by biaxial molecules and, to date, all reported observations of biaxial phases are derived from biaxial molecules [128]. However, as a 50-year search for a biaxial phase has demonstrated, not all biaxial molecules form biaxial phases [128]. In comparison to bulk biaxiality, localised biaxiality is relatively easy to induce through the application of external forces such as electric fields, or through confinement and proximity to surfaces which reduce the inherent symmetry of the bulk. In the case of induced biaxiality it is possible for both uniaxial and biaxial molecules to exhibit biaxial ordering [131]. A water molecule is molecularly biaxial, i.e. the molecular orientation must be defined by an orthogonal set of molecular directions. It is perhaps the simplest biaxial molecule that naturally occurs, so a biaxial ordering might expected to be possible.

In previous studies, the structure and average orientation of water close to solid surfaces or inside CNTs have usually been presented in terms of the density, radial distributions, hydrogen bonding, and dipole moments [132–135]. These measures provide an adequate description of the spatial structure of the water and the presence and position of layers. The angle between the direction $\mathbf{l}_m$ (the dipole moment vector) and an axis (such as the flow direction or an electric field direction) defines the dipole moment, the distribution of which can provide an average orientation and a measure of directional ordering.

For a more complete description of the ordering of biaxial molecules, three orthogonal molecular directions $\mathbf{n}_m$, $\mathbf{l}_m$ and $\mathbf{m}_m$, must be defined such as those for the water molecule shown in Fig. 3.1. The direction $\mathbf{n}_m$ corresponds, by convention in the liquid crystal field, to the molecular long axis; $\mathbf{l}_m$ is along the molecular short axis, which coincides with the molecular dipole direction; and $\mathbf{m}_m$ is orthogonal to $\mathbf{n}_m$ and $\mathbf{l}_m$ (i.e.

$\mathbf{m}_m = \mathbf{n}_m \times \mathbf{l}_m$). With these directions the symmetric, traceless, second-rank tensors can be constructed:

$$\mathbf{q} = \mathbf{n}_m \otimes \mathbf{n}_m - \frac{1}{3}\mathbf{I}, \tag{3.1}$$

and

$$\mathbf{b} = \mathbf{m}_m \otimes \mathbf{m}_m - \mathbf{l}_m \otimes \mathbf{l}_m, \tag{3.2}$$

where $\mathbf{I}$ is the second-rank identity tensor.

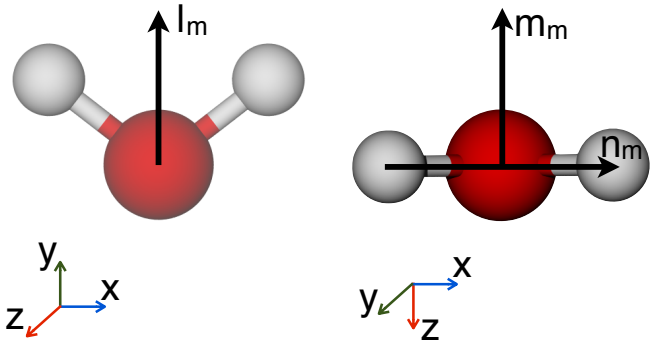

Figure 3.1: Principal directions in the water molecule. The three directions $\mathbf{n}_m$, $\mathbf{l}_m$ and $\mathbf{m}_m$ defined in the TIP4P/2005 water model.

The average orientation of an ensemble of these biaxial molecules can then be represented by the two order tensors $\mathbf{Q}$ and $\mathbf{B}$, the ensemble averages of their microscopic counterparts $\mathbf{q}$ and $\mathbf{b}$. The exact form of the averaging varies; here both the radial (measured from the CNT axis) and axial (along the CNT axis) dependence of the order tensors is measured, i.e. $\mathbf{Q}(r)$ and $\mathbf{Q}(z)$ (no statistically significant dependence of the order tensors with respect to the polar angle θ is found). The ensemble averages for $\mathbf{Q}(r)$ and $\mathbf{Q}(z)$ (and similarly for $\mathbf{B}(r)$ and $\mathbf{B}(z)$) are constructed over bins in the streamwise axial direction and the radial direction, respectively. The macroscopic tensors are therefore,

$$\mathbf{Q} = \frac{1}{\tilde{\tau}N}\sum_{i=1}^{\tilde{\tau}}\sum_{j=1}^{N}\mathbf{q}_{i,j}(r,\theta,z), \tag{3.3}$$

$$\mathbf{B} = \frac{1}{\tilde{\tau}N}\sum_{i=1}^{\tilde{\tau}}\sum_{j=1}^{N}\mathbf{b}_{i,j}(r,\theta,z), \tag{3.4}$$

where N is the number of water molecules inside the axial or radial bin and $\tilde{\tau}$ is the

number of MD time-steps over which the system is sampled. When the water density ρ is small the statistics of $\mathbf{Q}$ and $\mathbf{B}$ will be unreliable and so only measurements for $\rho > 100$ kg/m^3 are considered here. It will be shown that these order tensors provide information in addition to a standard dipole moment calculation, the information for which is in fact contained within one of the eigenvalue/eigenvector pairs of the tensor $\mathbf{B}$.

Interpreting the measured values of $\mathbf{Q}$ and $\mathbf{B}$ is done through an investigation of their eigenvalues and eigenvectors. The tensors are symmetric and traceless so that two of the total three eigenvalues are independent, and the set of eigenvectors forms an orthogonal triad, for each tensor. It is the eigenvectors that describe the principal axes of the averaged molecular axes, and the eigenvalues measure the spread of molecular deviation from the eigenvector: $\mathbf{Q}$ provides information about the long molecular axis, and $\mathbf{B}$ describes the effects of molecular biaxiality on the ensemble average properties. Both tensors are zero in the isotropic phase (i.e. bulk water), but any loss of isotropy will lead to non-zero eigenvalues and a sensitivity to the direction of the average orientation of the molecular directions.

If the molecular direction $\mathbf{n}_m$ forms a uniaxial arrangement then $\mathbf{Q}$ will have two equal eigenvalues; similarly for $\mathbf{B}$. In uniaxial cases, the eigenvector corresponding to the distinct eigenvalue indicates the orientation of the director, revealing a radial, angular or axial uniaxial nematic phase. If the distinct eigenvalue is negative then the molecular axis is, on average, oriented randomly in a plane with a director oriented orthogonal to this plane.

On the other hand, biaxiality is present if all three eigenvalues of either $\mathbf{Q}$ or $\mathbf{B}$ are different, with the former case indicating that the molecular direction $\mathbf{n}_m$ has a biaxial configuration and the latter case revealing a biaxial nematic phase due to the molecular shape. Since the bulk phase of water is isotropic, if there is any form of anisotropic order, uniaxial or biaxial, it has been induced by the confining CNT or the applied electric field, or both. Such a situation is termed paranematic ordering.

Convenient, and commonly used, measures of the presence of anisotropy and biax-

iality are through the parameters [136, 137]:

$$\alpha_Q = \frac{3}{2}\mathrm{tr}\left(\mathbf{Q}^2\right), \tag{3.5}$$

$$\alpha_B = \frac{3}{2}\mathrm{tr}\left(\mathbf{B}^2\right), \tag{3.6}$$

$${\beta_Q}^2 = 1 - \frac{6\left[\mathrm{tr}\left(\mathbf{Q}^3\right)\right]^2}{\left[\mathrm{tr}\left(\mathbf{Q}^2\right)\right]^3}, \tag{3.7}$$

$${\beta_B}^2 = 1 - \frac{6\left[\mathrm{tr}\left(\mathbf{B}^3\right)\right]^2}{\left[\mathrm{tr}\left(\mathbf{B}^2\right)\right]^3}. \tag{3.8}$$

Non-zero values of α_Q or α_B indicate the presence of anisotropic ordering, while non-zero values of ${\beta_Q}^2$ or ${\beta_B}^2$ indicate that a biaxial paranematic state has been induced. The singularity present in ${\beta_Q}^2$ and ${\beta_B}^2$ as the system becomes isotropic (where $\mathbf{Q} = \mathbf{0}$, $\mathbf{B} = \mathbf{0}$) is avoided by only performing the biaxiality calculation when the $\alpha_{Q,B}$ values are sufficiently different from zero (in this thesis it is insisted that $\alpha_{Q,B} > 0.02$). The anisotropy and biaxiality parameters vary in the intervals $[-0.5, 1]$ and $[0, 1]$ respectively, with $\alpha_{Q,B} = 0$ and $\alpha_{Q,B} = 1$ corresponding to isotropy and perfect alignment, respectively, and ${\beta_{Q,B}}^2 = 0$ and ${\beta_{Q,B}}^2 = 1$ corresponding to uniaxial and maximally biaxial states, respectively.

3.2 Simulation details

3.2.1 System geometry and MD setup

A 12.5 nm long CNT connects two water reservoirs, with graphene sheets (10.5×10.2 nm) acting as the separating walls. This CNT is long enough to produce a fully developed flow inside it within a reasonable simulation time. The chirality of the CNT, (15,14) in this case, defines its diameter D according to:

$$D = \sqrt{3}\mathrm{L}_{C-C}\frac{\sqrt{ch_1^2 + ch_2^2 + ch_1 ch_2}}{\pi}, \tag{3.9}$$

where $\mathrm{L}_{C-C} = 0.2461$ nm is the carbon-carbon bond length and ch_1, ch_2 are the magnitudes of the chiral vectors. Periodic boundary conditions are applied in all directions,

and the temperature is maintained at a constant 298 K in the two reservoirs by applying Berendsen thermostats. A characteristic snapshot of the simulated system is shown in Fig. 3.2.

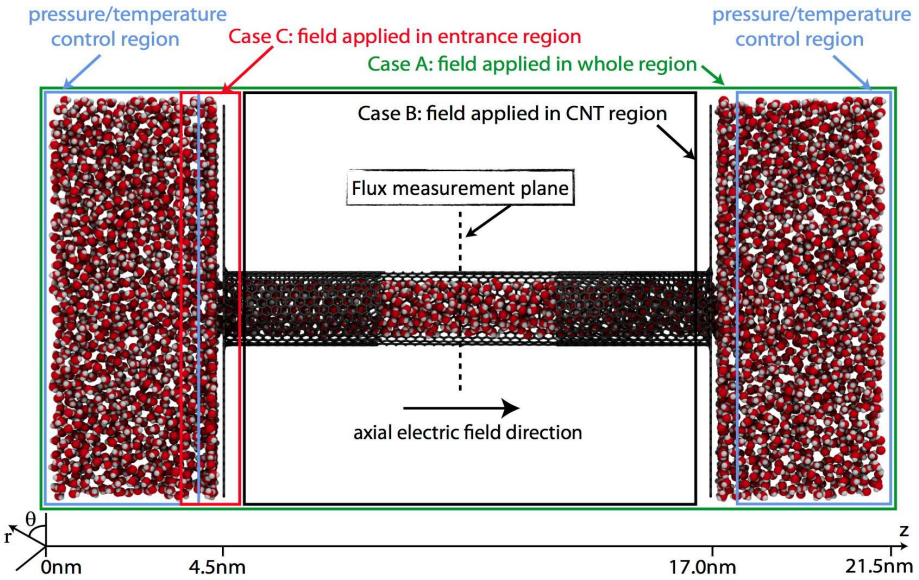

Figure 3.2: Characteristic snapshot of the simulated CNT flow system. In the blue boxed areas temperature and pressure are controlled in order to maintain a constant temperature of 278 K and create a 100 MPa pressure difference between the water reservoirs. When an axial electric field is present it is applied across: the whole system, green box from $z = 0$ nm to $z = 21.5$ nm (Case A); the CNT region alone, black box from $z = 4.7$ nm to $z = 16.7$ nm (Case B); or only the entrance region, red box from $z = 3.2$ nm to $z = 4.7$ nm (Case C). Black dashed line indicates the position of the flux measurement plane.

In this application every case is initially equilibrated for at least 4 ns, and during the first 800 ps of the equilibration run density is also controlled inside the blue boxed regions using the FADE density controller [59]. The target densities can be calculated according to the compressibility equation

$$\rho = \frac{\rho_0}{1 - (P_1 - P_0)/E_{bm}} \tag{3.10}$$

where $\rho_0 = 997.5$ kg/m^3 is the density of water under atmospheric pressure at 298 K, $E_{bm} = 2.15 \times 10^9$ N/m^2 is the bulk modulus fluid elasticity of water, $P_1 = 100$ MPa and $P_0 = 0.1$ MPa are the high and low (atmospheric) pressures in the corresponding reservoirs, respectively. The calculated density from Eq. (3.10) for the high pressure reservoir is 1046 kg/m^3. After the equilibration, each simulation contains around 33000 water molecules. Production runs are then performed for a minimum duration of 4 ns,

during which all measurements are sampled and averaged in order to achieve better statistics. This required at least 110 computational hours on a GPU.

For this setup, both LJ and Coulomb interactions are truncated at a cutoff radius of $r_{cut} = 1.0$ nm which combines acceptable accuracy and computational efficiency [18, 32], while Coulomb interactions are also shifted in order to avoid introducing spurious effects [18, 47, 49]. The solid atoms in the CNT and graphitic sheets are kept fixed, which is a common simplification in MD simulations that contributes significantly to computational savings with only minor effects on the results [3, 19, 20, 48, 138].

In cases where an external homogeneous static electric field $\mathbf{E}$ is applied along the $z-$axis of the system, it is implemented as an additional force $\mathbf{F}_i = q_i \cdot \mathbf{E}$, where q_i is the partial charge on atom i [139, 140]. It has previously been shown that this is a valid MD representation of the influence of an electromotive force exerted by a voltage difference between two electrodes [141, 142]. It has also been used to impose a potential difference across a membrane in simulations of electroporation of lipid bilayers [143].

3.2.2 Pressure difference imposition and mass flow rate measurement

After an equilibration time of at least 2 ns, a pressure difference of 100 MPa is imposed and maintained between the two water reservoirs. This pressure difference, although high by experimental standards, is common practice in MD simulations, as no major spurious effects appear when compared to the low-pressure-difference case that is closer to actual operating conditions [18, 32, 144–147]. The resulting high flow velocity, however, improves the signal-to-noise ratio in velocity profile measurements.

In previous publications, for a standalone nanotube (no reservoirs) with periodic boundary conditions in the flow direction pressure difference control has been achieved by imposing a uniform body force to all liquid molecules in the nanotube [148–150]. For more complex geometries, like the membranes in this thesis, the overall cross-sectional area is not uniform (i.e., from reservoir to nanotube to reservoir) and so the pressure gradient will vary; fundamentally, a uniform body forcing is not capable of reproducing flows that are hydrodynamically equivalent to those generated by a pressure difference over the same geometry. Previous studies of systems similar to that considered here have used moving walls, acting as pistons, in order to control the pressure difference be-

tween the reservoirs, however this option breaks the computationally useful periodicity in the flow direction [18, 33].

In all simulations presented in this thesis, a pressure difference is imposed between the two reservoirs by applying a Gaussian-distributed force over cross-sectionally uniform regions in the reservoirs only (see the blue boxed regions in Fig. 3.2). This essentially creates a user-defined pressure drop over the entire system. This Gaussian forcing approach is a development of previous publications [144, 151] in which step-forcing was used to create the necessary pressure difference. Gaussian forcing, however, creates a spatially smooth imposition of momentum to the MD fluid, while maintaining the simplicity of using periodic boundary conditions. The magnitude of the imposed force in the blue boxed regions in Fig. 3.2 is:

$$F_z(z) = \begin{cases} \bar{F} \exp\left\{-z^2/2\sigma_s^2\right\} & \text{if } z_1 \leq z \leq z_2, \\ 0 & \text{otherwise,} \end{cases} \tag{3.11}$$

where σ_s is the standard deviation of the distribution and $\bar{F}$ is its peak value, i.e.

$$\bar{F} = \frac{\Delta p}{\rho_n \sigma_s \sqrt{2\pi}}, \tag{3.12}$$

with ρ_n the average number density inside the two reservoirs and Δp the desired pressure difference between them. The standard deviation σ_s can take any value provided that it is significantly smaller than the distance $z_2 - z_1$, which is the total length of the blue boxed regions. In all the applications presented in this thesis $\sigma_s = 2.5$ nm and $z_2 - z_1 = 8.2$ nm. A more detailed description of this Gaussian-forcing method is provided by Borg *et al.* [58].

The applied pressure difference creates a net mass flow rate $\dot{m}$ (kg/s) along the nanotube, which is measured on a plane at the middle of the membrane system (see Fig. 3.2). The mass of the total number of molecules that cross the target flux-plane in the $z-$direction is counted as positive, and the mass of those which cross in the opposite direction is counted as negative. The mass flow rate is then calculated by dividing the

total mass flow counted by the time over which the averaging is performed [32, 58], i.e.,

$$\langle \dot{m} \rangle = \frac{1}{\Delta t_{av}} \sum_{i}^{\delta N} m_i \, \mathrm{sgn} \left(\boldsymbol{u}_i \cdot \hat{\boldsymbol{n}}_z \right), \tag{3.13}$$

where $\hat{\boldsymbol{n}}_z$ is the unit vector in the $z-$direction perpendicular to the flux-plane, $\boldsymbol{u}_i$ and m_i are the velocity vector and the mass of molecule i crossing the flux plane, and δN is the total number of molecules that cross the plane in either direction during the time $t \to t + \Delta t_{av}$. The function sgn () provides the crossing direction. The volumetric flow rate $\dot{Q}_{MD}$ is calculated by simply dividing $\langle \dot{m} \rangle$ by the water bulk density ρ.

3.3 Water confined in nanotubes

The anisotropy and biaxiality of water transported in the z-direction along a CNT by a pressure difference is considered here, along with the subsequent changes in ordering when an axial electric field is applied. The electric field magnitudes that are examined are within the range 0.01 to 1 V/nm, which are typical of those produced by charged electrodes, ion channels, ionic biomolecules or assemblies, and electroporation [125, 152–154]. In biological membranes during the process of electroporation, for example, the typical electric field range is $0.3 - 0.5$ V/nm [155, 156].

When an electric field in the range 0.01 to 1 V/nm is applied to water in a nanotube, the density and hydrogen bonding profiles are all almost identical to the reference zero-field case. In contrast, a number of previous MD studies have used much higher electric fields (> 1.5 V/nm) so that water shows a strong structural ordering, similar to that of ice [134, 139, 157]. Other recent studies have also shown an ordering effect due to applied electric fields, inducing or promoting the liquid to solid phase transition [140, 158]. In all the cases presented here the water remains in a liquid phase.

In the reservoirs, and within the bulk region inside the CNT, water is isotropic ($\alpha_Q \approx 0$, $\alpha_B \approx 0$). However, even without an applied electric field, a biaxial paranematic state arises close to the CNT walls. Figure 3.3(a) indicates a weak uniaxial state for the molecular direction $\mathbf{n}_m$, since there is one distinct eigenvalue of $\mathbf{Q}$, at a radial distance of approximately 0.65 nm from the CNT axis, where the density is at a maximum. Figure 3.3(b) shows that, at this same location, the $\mathbf{B}$ tensor exhibits a degree

of biaxiality, since all eigenvalues are different.

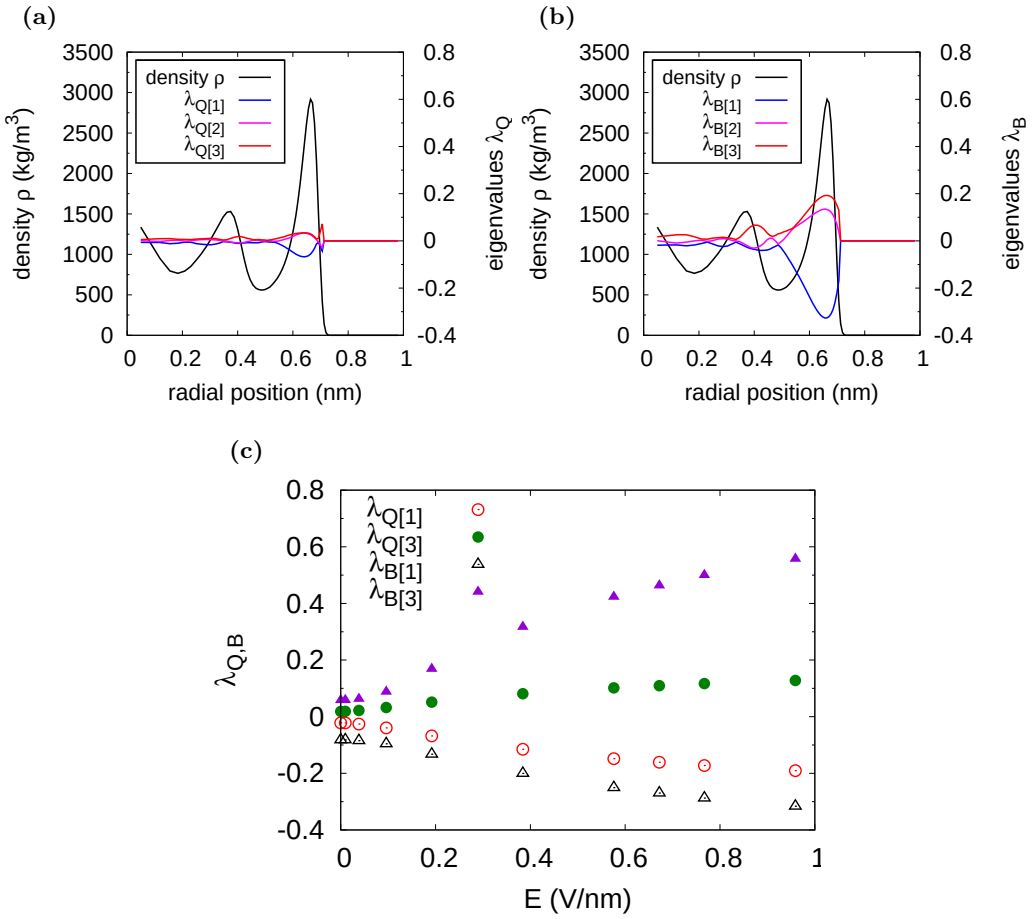

Figure 3.3: Eigenvalues of the order tensors inside the CNT. Eigenvalues are labelled in ascending order, with $\lambda_{Q[1]}$ and $\lambda_{B[1]}$ being the smallest. The water density profile is also shown with a black line. **a,** Eigenvalues λ_Q of the order tensor $\mathbf{Q}$; **b,** eigenvalues λ_B of the order tensor $\mathbf{B}$; **c,** maximum and minimum eigenvalues $\lambda_{Q,B}$ of the order tensors when the electric field is applied over the whole system (Case A). Standard error of the mean (SEM) with 95% confidence interval is smaller than the symbol.

An investigation of the eigenvectors of the tensors in Figs. 3.4a and 3.4b indicate that the preferred orientation of $\mathbf{l}_m$ is radial to the nanotube walls. In detail, the eigenvectors of the highest eigenvalues have to be studied in order to find the preferred orientation. For both tensors the first eigenvalue ($\lambda_{Q[1]}$ and $\lambda_{B[1]}$) has the largest absolute value, meaning that eigenvectors $\boldsymbol{\xi}_{Q[1]}$ and $\boldsymbol{\xi}_{B[1]}$ will reveal the preferred average direction of the water molecules inside the CNT. In both eigenvectors the radial component (black diamonds on Fig. 3.4) is the dominant one within the high density and high anisotropy region near the wall. At first this may seem contradictory as $\mathbf{Q}$ and $\mathbf{B}$

are orthogonal by construction. But as both of the largest absolute eigenvalues ($\lambda_{Q[1]}$ and $\lambda_{B[1]}$) are negative (see Fig. 3.3a and 3.3b) then the molecular axis is, on average, oriented randomly in a plane with the eigenvector oriented orthogonal to the plane. Combining all the above, it can be concluded that the average preferred orientation of the dipole moment vector $\mathbf{l}_m$ is radial to the nanotube walls.

If an electric field is applied over the entire system, anisotropy rises and water molecules are expected to start aligning their dipole moment vector along the same direction as the applied electric field. For the largest applied field tested ($\mathbf{E} = (0, 0, 0.959)$ V/nm), $\lambda_{Q[1]}$ still has the highest absolute value among the $\mathbf{Q}$ eigenvalues, while $\lambda_{B[3]}$ has the highest absolute value of the $\mathbf{B}$ eigenvalues, as Fig. 3.3c shows. From the corresponding eigenvectors shown in Fig. 3.5 ($\boldsymbol{\xi}_{Q[1]}$ and $\boldsymbol{\xi}_{B[3]}$), and following the theory presented above it can be clearly observed that the average preferred orientation of $\mathbf{l}_m$ has changed from radial to the nanotube walls to axial along the CNT, in the flow direction, and the direction of the applied electric field.

In order to further analyse the structure of water molecules inside the CNT, without an external electric field, radial profiles of density and the average number of hydrogen bonds (n_{HB}) are presented in Fig. 3.6. Towards the centre of the CNT both the density and hydrogen bonding have values close to the bulk values. However, there is a high density water layer formed close to the CNT walls where the number of hydrogen bonds is significantly reduced, as expected due to the presence of the solid wall. This highly dense and oriented water layer promotes water flow inside the nanotubes, essentially acting as a lubrication film between the bulk water phase and the solid walls.

Three cases are considered in which the water molecules experience an electric field in different regions. In the first situation, Case A, all molecules in the system experience the axial electric field. Figures 3.7a and 3.7c show that anisotropy (i.e. $\alpha_{Q,B}$) increases with increasing field magnitude. The biaxiality of $\mathbf{Q}$ also increases (Fig. 3.7b), but the biaxiality of $\mathbf{B}$ initially increases and then decreases as the field magnitude increases (Fig. 3.7d). This decrease in biaxiality is due to the aligning effects of the high magnitude applied field (which is a forcing that has uniaxial symmetry) that tends to prefer uniaxial ordering of the molecular dipole along the z-axis, in competition with the zero-field alignment of $\mathbf{l}_m$ along the radial direction. Figure 3.8 shows that for Case A,

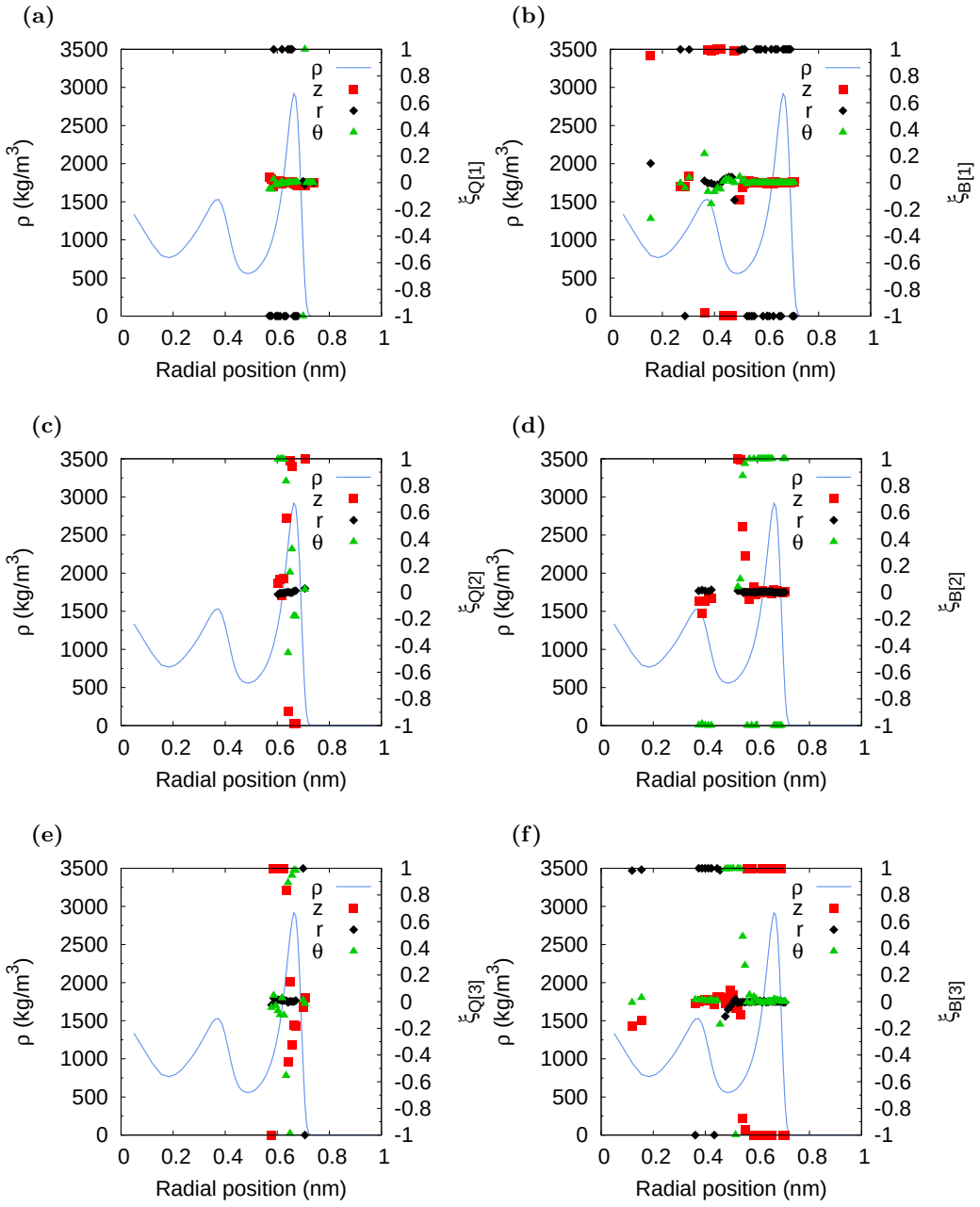

Figure 3.4: z, r, θ components of the eigenvectors $\boldsymbol{\xi}$ for all the eigenvalues of the order tensors **Q** and **B**. Radial density profile is also plotted in blue in order to highlight water layering. Eigenvector components are plotted only when the corresponding eigenvalue is bigger than 0.02, in order to show areas with significant anisotropy and to reduce noise.

with the electric field applied across the whole system, the mass flux $\dot{m}_E$ (normalised by the zero-field flux $\dot{m}_0$) does not appreciably change. Although anisotropy is increasing significantly as the field magnitude is increased, the mass flow rate remains almost constant for E < 0.7 V/nm. For higher electric fields up to E = 0.959 V/nm the flow

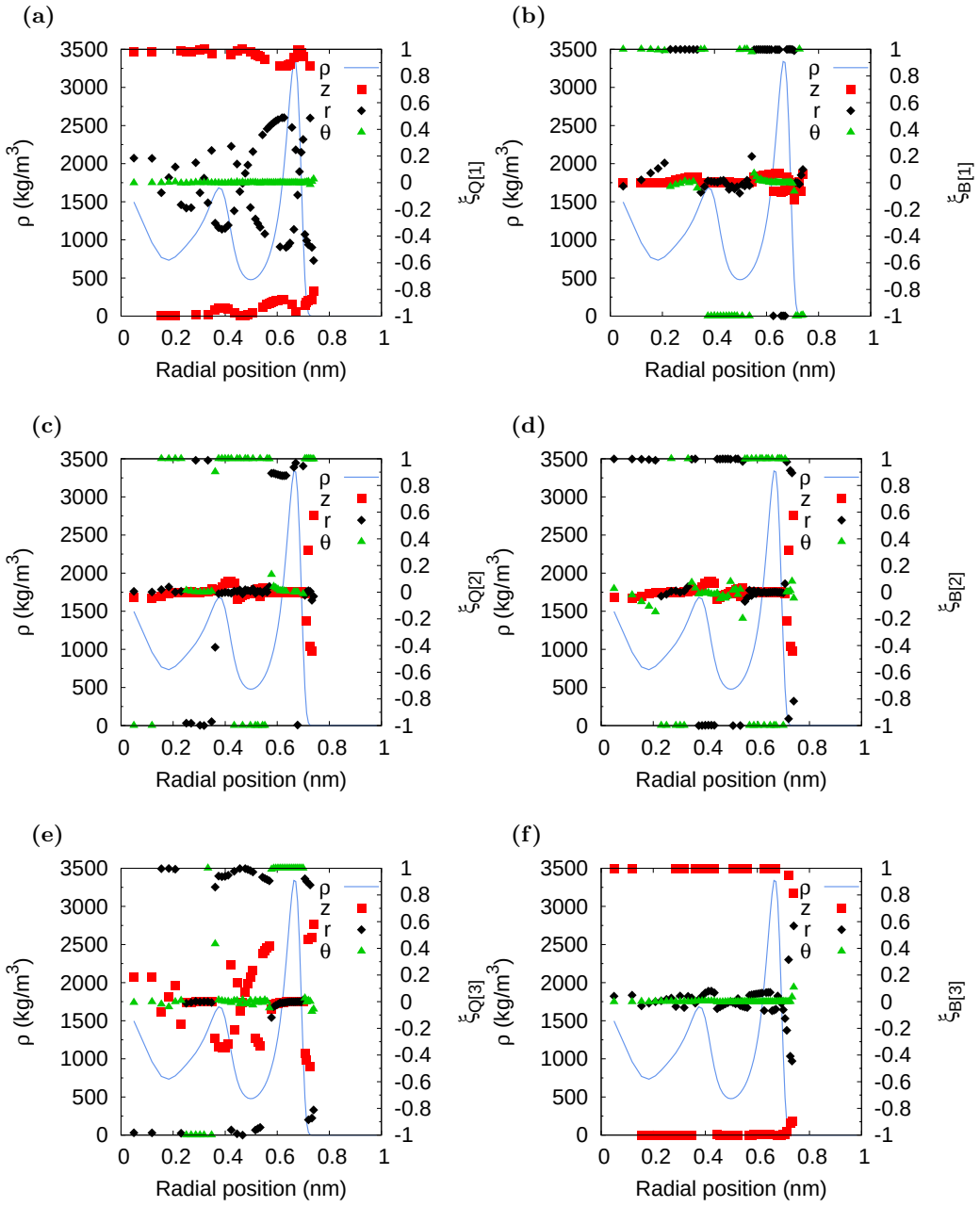

Figure 3.5: z, r, θ components of the eigenvectors $\boldsymbol{\xi}$ for all the eigenvalues of the order tensors $\mathbf{Q}$ and $\mathbf{B}$. Radial density profile is also plotted in blue in order to highlight water layering. A static electric field of $(0, 0, 0.959)$ V/nm is applied over the whole system. Eigenvector components are plotted only when the corresponding eigenvalue is bigger than 0.02, in order to show areas with significant anisotropy and to reduce noise.

rate only increases by around 10% compared with the zero-field case.

In Case B, an axial electric field is applied across the CNT region only (from $z = 4.7$ nm to $z = 16.7$ nm as shown in Fig. 3.2). The resulting anisotropy and biaxiality

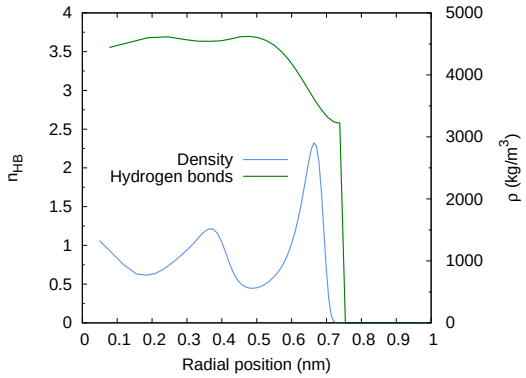

Figure 3.6: Radial density profile and average number of hydrogen bonds per water molecule (n_{HB}) inside the CNT without an external electric field.

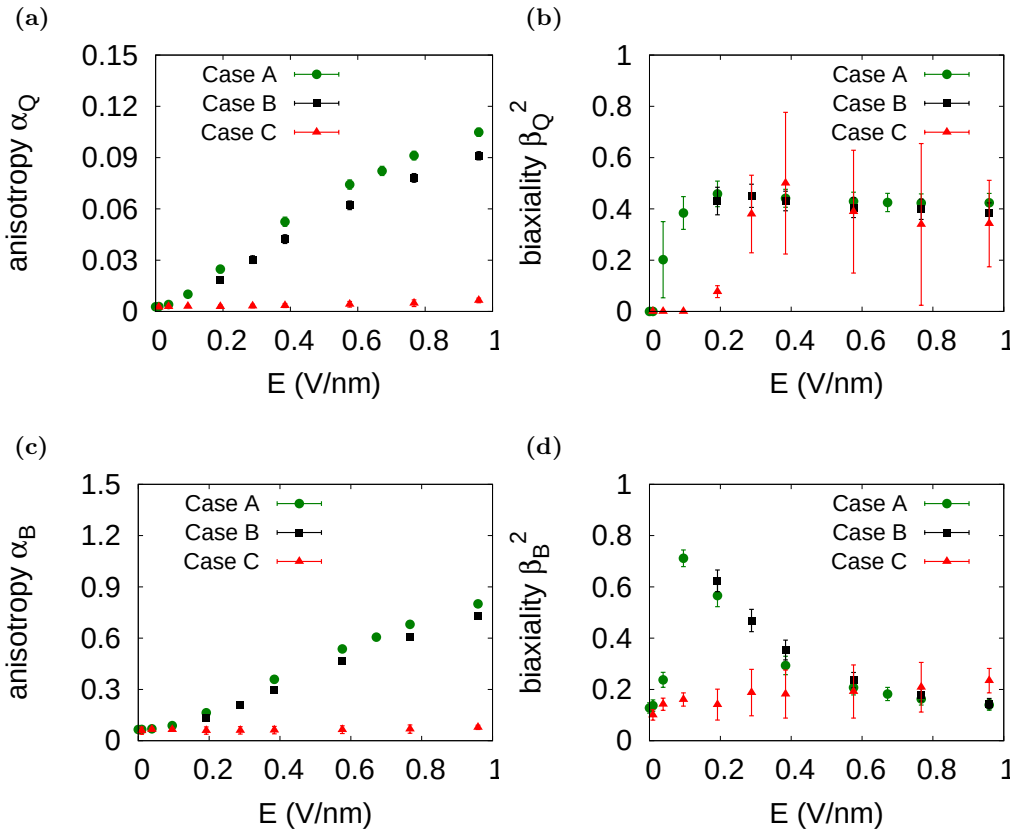

Figure 3.7: a, b, c, d, Mean values of $\mathrm{tr}(Q^2)$, β_Q^2, $\mathrm{tr}(B^2)$ and, β_B^2, respectively, varying with the applied field **E**. Measurements along the nanotube are made in a cylinder with radius 0.7 nm, centred on the nanotube axis, in the streamwise direction. Errorbars show two STDs of the samples (95% confidence interval).

parameters are similar to Case A, as shown in Fig 3.7. However, for this case, Fig. 3.8 does show a change in mass flow rate with increasing field magnitude, with a decrease of around 30% at the highest field magnitudes. This decrease in flux indicates that

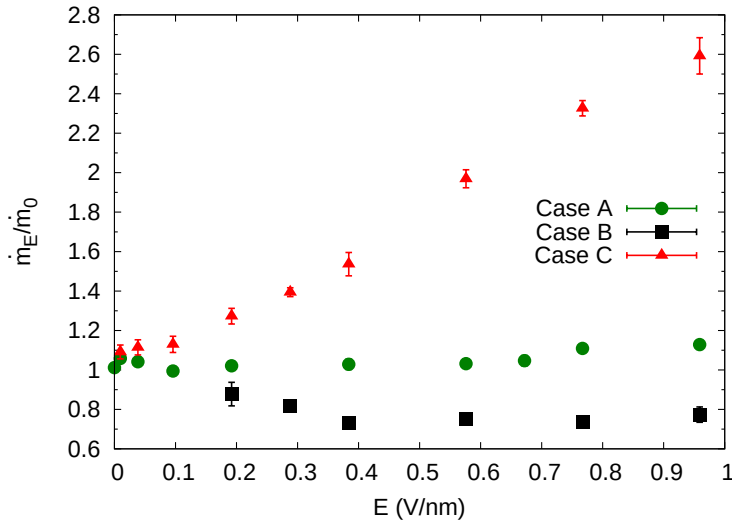

Figure 3.8: Reduced mass flow rate $\dot{m}_E/\dot{m}_0$ measured for various electric field magnitudes E in all three simulated cases. Measurements along the nanotube are made in a cylinder with radius 0.7 nm, centred on the nanotube axis, in the streamwise direction. Errorbars show two STDs of the samples (95% confidence interval).

the changes in order within the CNT are actually causing an increase in the effective friction.

In Case C, the electric field is only applied across the entrance region of the CNT (from $z = 3.2$ nm to $z = 4.7$ nm as shown in Fig. 3.2). Figure 3.7 shows that the mean values of anisotropy remain relatively low, since the orienting field only affects a limited region. Biaxiality does seem to occur but the error bars are large since the anisotropy (which occurs in the denominator of ${\beta_{Q,B}}^2$) is small. To highlight the differences between Cases A and C, Fig. 3.9 shows contour plots of the highest eigenvalues of $\mathbf{Q}$ and $\mathbf{B}$ with an applied electric field $\mathbf{E} = (0, 0, 0.384)$ V/nm in both cases. The anisotropy rise at the entrance of the CNT in Case C, in contrast to the high anisotropy along the CNT in Case A, seems to significantly affect the flow rate (as Fig. 3.8 shows). This localised application of an electric field leads to a super-linear increase of the flow rate with field magnitude. At the strongest field magnitude studied, flow rates of more than twice the zero-field flow rate were measured, even though the cross-membrane pressure difference remains constant.

When an electric field is applied anywhere in the system the orienting effect of the field on the molecular dipole will alter the anisotropy and biaxiality as shown in Fig. 3.7. However, as reported in previous publications [134, 139, 157], the structural

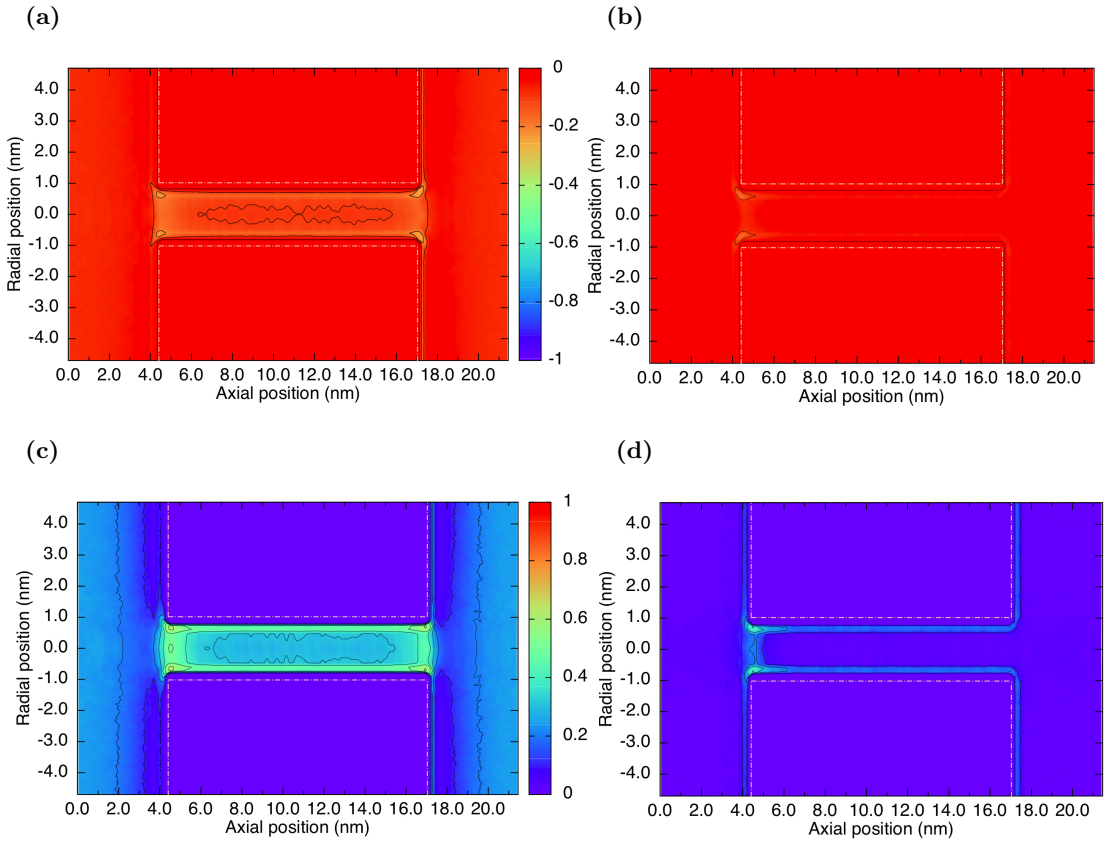

Figure 3.9: **a** and **c** are contour plots of the highest eigenvalue of **Q** and **B**, respectively, for Case A; **b** and **d** are the equivalent for Case C. The colour range of Case A figures applies to the equivalent Case C figures too. The electric field here is $\mathbf{E} = (0, 0, 0.384)$ V/nm. The dashed white lines show the position of the membrane walls and the CNT.

nature and liquid phase of water under these conditions is not altered, and so it would be impossible to uncover this change in the average orientation of the water molecules from examining the density and hydrogen bonding measurements alone. In fact, for the range of electric field magnitudes applied here, the shapes of the radial density and hydrogen bonding profiles are identical to those in the zero-field case, as a few characteristic field magnitudes show in Figs. 3.10a and 3.10c. Figure 3.10b, however, shows that the peak value of the density profile increases by approximately 15% as a stronger electric field is applied, and reaches a maximum for an electric field of 0.959 V/nm. From the hydrogen bonding measurements in Fig. 3.10d it can be observed that the maximum difference between the high-field case and the zero-field case is lower than the maximum density difference, in fact it is close to the level of statistical error.

To understand the orienting effects of the patterned fields in each of the above cases

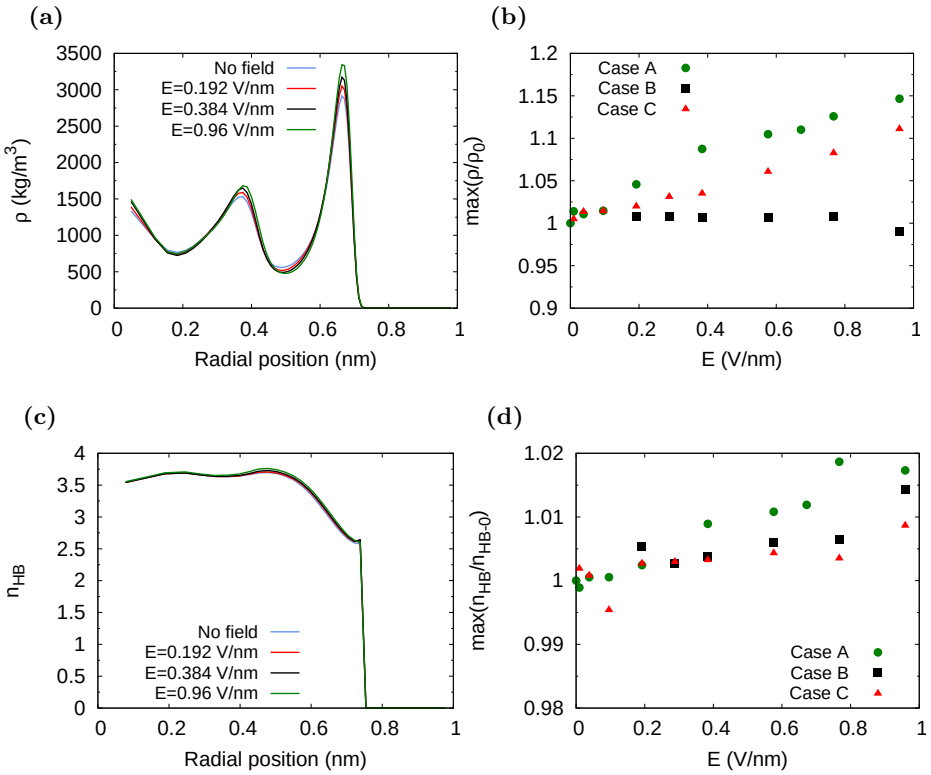

Figure 3.10: **a**, Radial density profiles for various magnitudes of electric fields (Case A). **b**, Maximum density ratio for the three studied cases relative to the reference no field case. **c**, Radial hydrogen bonding profiles for various magnitudes of electric fields (Case A). **d**, Maximum hydrogen bonding ratio for all the three studied cases relative to the reference no field case. The density and the number of hydrogen bonds are sampled inside the nanotube only.

the author considers the variations in pressure, velocity, anisotropy and biaxiality along the axial direction z. Figures 3.11 and 3.12 include plots of these profiles through the system — from the inlet reservoir, through the CNT, to the outlet reservoir — for the case of zero field as well as Cases B and C with $\mathbf{E} = (0, 0, 0.384)$ V/nm, which were shown to reduce and increase flow rates, respectively.

The pressure and velocity profiles in Fig. 3.11 show that the atomistically smooth CNT (without an electric field) transports water with minimal frictional losses, although entrance losses are quite significant. The entrance losses have the greatest impact on the water velocity inside the CNT, and as a consequence to the flow rate. Preordering the water molecules with an electric field (Case C) before they enter the CNT almost halves the entrance pressure losses and this is also shown at the equal increase of the fluid velocity. However, the application of an electric field around the CNT only (Case

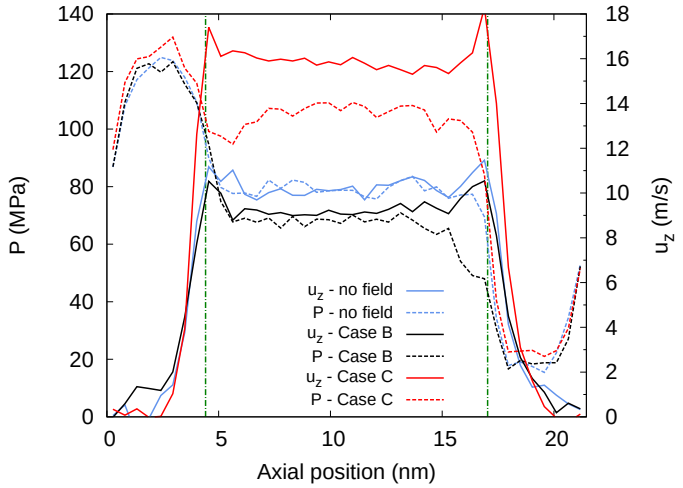

Figure 3.11: Performance analysis for various application regions of the electric field. Comparison of axial profiles of pressure and streaming velocity along the CNT axis. The vertical dot-dashed green lines indicate the entrance and exit of the CNT. In all cases the electric field is fixed to be $\mathbf{E} = (0, 0, 0.384)$ V/nm.

B) increases the entrance and frictional losses leading to a reduced water velocity in the CNT.

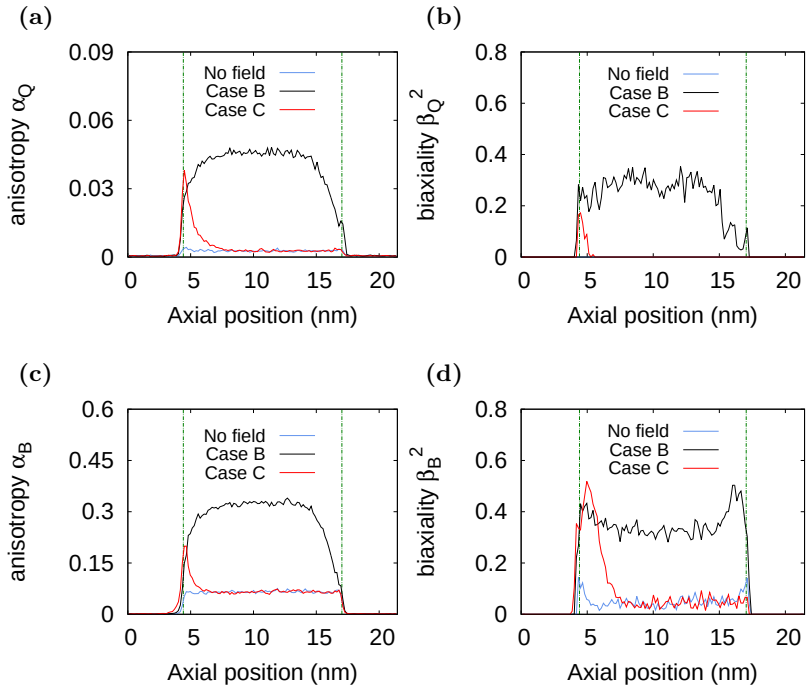

Figure 3.12: a,b, c, d Axial development of $\mathrm{tr}(Q^2)$, β_Q^2, $\mathrm{tr}(B^2)$, and β_B^2, respectively, along the whole system. The vertical dot-dashed green lines indicate the entrance and exit of the CNT. In cases B and C the electric field is fixed to be $\mathbf{E} = (0, 0, 0.384)$ V/nm.

Figure 3.12 shows that the application of an electric field only over the nanotube (Case B) increases the anisotropy and biaxiality of the water, and given the results in Figs. 3.8 and 3.11, this increased order increases the entrance and frictional losses within the CNT, leading to a reduced flow rate. However, in Case C, the ordering within the bulk of the CNT is unchanged from the zero-field case but the anisotropy and biaxiality has been increased in a region close to the entrance of the CNT (see Fig. 3.12). The corresponding significant reduction in the entrance pressure losses enables the flow to be driven in the CNT with a higher pressure. At the exit of the nanotube, expansion to the reservoir leads to a sudden decrease in pressure and velocity. Although this expansion is more severe in Case C, the effect on the flow velocity is minimal compared to the gains in velocity due to the reduced entrance losses.

3.4 Electric field and flow enhancement limitations

This last section investigates the effect of even higher fields in Case C simulations and discusses the maximum flow rate enhancement achievable by using fields of very high magnitude. The magnitude of these fields is much greater than those commonly observed in biological processes or in electromechanical devices. In section 3.1 it was mentioned that extreme fields (> 1.5 V/nm) do change the properties of water from liquid to solid (crystalline), and can induce or enhance the liquid-to-solid transition in low temperature environments.

Figure 3.13 shows the maximum flow rate increase that can be achieved with a static electric field applied close to the CNT entrance (case C). For fields greater than 2 V/nm, the water state change (solidification) hinders any gains from the preordering effect. A crystalline (ice) layer forms at the entrance of the CNT, blocking the flow of water molecules.

The water phase change can be verified by the density and hydrogen bonding measurements presented in Fig 3.14. This figure shows a sudden density decrease in the region where the electric field is applied, while hydrogen bonding increases. For electric fields bigger than 1 V/nm the density decrease is more significant, to around 950 kg/m^3 — the density of ice and not liquid water. In addition, the average number of hydrogen bonds per water molecule is increased, from 3.6 in the no-field region to 3.7. For fields

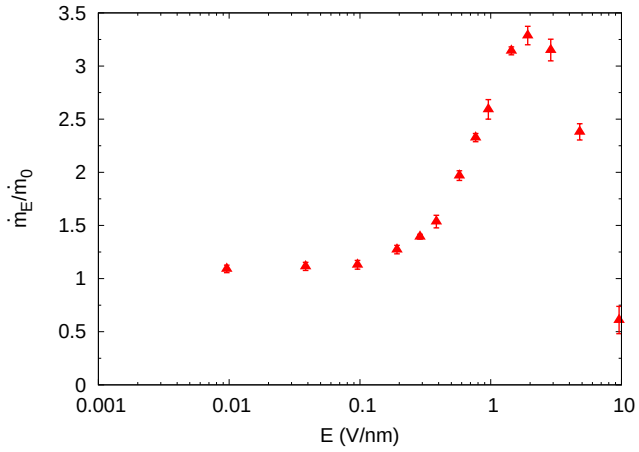

Figure 3.13: Reduced mass flow rate $\dot{m}_E/\dot{m}_0$ measured at various electric field magnitudes **E** for Case C simulations. Measurements along the nanotube are made in a cylinder of radius 0.7 nm, centred on the nanotube axis, in the streamwise direction. Errorbars show two STDs of the samples (95% confidence interval).

stronger than 3 V/nm there is a further increase indicating the complete solidification of water in that region. In combination with the flow rate results in Fig. 3.13 it can be concluded that the optimum flow conditions are achieved when density is low but the number of hydrogen bonds has not increased significantly. The average orientation of water molecules is strongly altered in the presence of an electric field. This is shown in Fig. 3.14, where the number of hydrogen bonds suddenly decreases just before water molecules enter the electric field region.

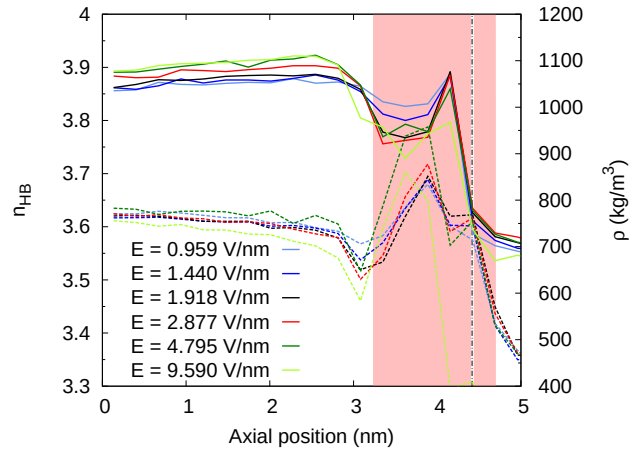

Figure 3.14: Axial density profiles (continuous lines) and average number of hydrogen bonds per water molecule (n_{HB}, dashed lines). Pink shaded area shows where the electric field is applied, while the vertical dot-dashed black line indicates the entrance of the CNT.

Finally, as expected anisotropy and biaxiality also increase in the region where the

electric field is applied, as Fig. 3.15 shows. Figures 3.15a and 3.15b show that for field magnitudes up to 3 V/nm the maximum value of anisotropy is measured inside the entrance of the CNT, while for higher electric fields anisotropy is higher outside the CNT and in the electric field region. The shape of the anisotropy curve is altered and the affected region becomes wider when the field is stronger than 3 V/nm. Although biaxiality is highly affected (see Figs. 3.15b and 3.15d) the increase is not monotonic with the magnitude of the applied field. The value of parameter β^2 initially decreases when the electric field increases from 0.959 V/nm to 3 V/nm. A further increase of the electric field magnitude then significantly increases the biaxiality parameter $\beta^2_{Q,B}$.

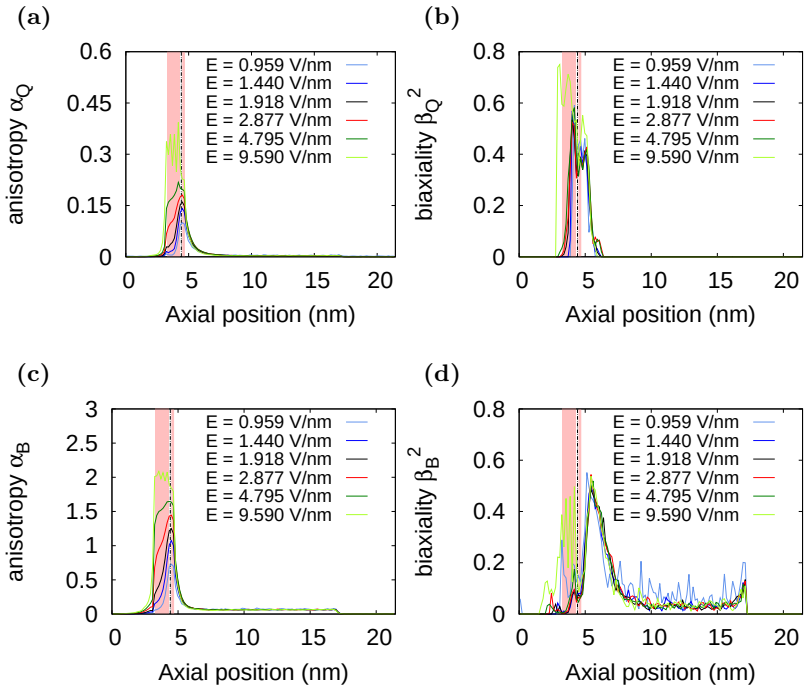

Figure 3.15: a, b, c, d, Axial development of $\mathrm{tr}(Q^2)$, β^2_Q, $\mathrm{tr}(B^2)$, and β^2_B, respectively, along the whole system. Pink shaded area shows where the electric field is applied, while the vertical dot-dashed black line indicates the entrance of the CNT.

3.5 Summary

This chapter presented the development of a method that can offer a more complete description of the ensemble order at the molecular scale. Using the order tensors in this method, an anisotropic/biaxial ordering of water inside and close to the entrance of a

carbon nanotube was revealed. Finally, it was demonstrated that spatially-patterned axial electric fields can be used to either enhance or diminish the pressure-driven flow of water in nanotubes.

The results presented indicate a super-linear growth in flow rate as a function of alignment, up to an electric field magnitude of 2 V/nm. For this high electric field an increase of over 300% in the flow rate, compared to the zero-field case, was observed. There are of course physical limits to the magnitude of the electric field that can be applied, and a further increase showed that a phase change occurred which hinders or even prohibits flow through the CNT. Other methods for causing molecular alignment might also exist. For instance, a tailored local surface polarisation or CNT inlet geometry may further enhance field-induced pre-ordering effects and suggest numerous routes for future investigations.

Chapter 4

Water flow inside nanotubes of different materials

Πάντα ρει και ουδέν μένει.

- Ηράκλειτος (535-474 π.Χ.)

Everything flows and nothing stays.

- Heraclitus (535-474 B.C.)

While there is now compelling evidence, from both experiments and molecular dynamics (MD) simulations, that liquid flow enhancement does indeed occur in nanotubes and other nanochannels, the origin of this phenomenon and how to control it is still subject to debate [8]. Some aspects are now generally accepted, including the nanotube diameter threshold below which the conventional continuum fluid mechanics model can no longer be applied [20], the presence of a reduced viscosity or depletion layer near the tube wall due to solid-liquid molecular interactions [19, 122], that the flow enhancement is proportional to the tube length [32], and that losses are mainly confined to the entrance region of the tube [18, 32, 159].

Another important aspect is the nanotube wall structure and chemistry. While the effect of roughness on fluid flow is not clear, there is compelling evidence that modifying the surface chemistry can alter the flow velocity, and so the flow enhancement. MD simulations have shown that imposing hydrophilic potentials on a CNT structure would significantly reduce the flow enhancement [19]. A similar result can be obtained

when introducing defects to the CNT structure [145]. Experiments have shown that functionalization of the entrance of CNT membranes can significantly alter capillary filling and flow enhancement [160], and that surface modification of the CNTs can be used to control their ability to imbibe liquids of different nature [161, 162]. Chapter 3 showed how static electric fields can control the water flow rate in CNTs. MD simulations have also shown that functionalization of the CNT tips could be used to control selective permeation of ions through CNT membranes [163], which is important for their potential use in water filtration and desalination applications [9].

This latter aspect, in particular, has led to the development of models to understand the effect of the solid-liquid interactions on fluid flow in nanotubes. Initial developments focussed on relating the flow enhancement to the wetting behavior of the nanotubes, via the slip length [164]. Others have attributed the enhancement effect solely to a reduced fluid viscosity at the wall [122, 165]. In contrast to this, a model based on the macroscopic Navier friction coefficient, calculated using a constant value of density and viscosity, has been recently proposed [30, 31, 166]. Each of these models is able to capture only some of the flow enhancement data in the literature, and they also make use of a number of fitting or semi-empirical parameters.

In this chapter, new MD simulations of water flowing in CNTs, boron nitride nanotubes (BNNTs) and silicon carbide nanotubes (SiCNTs) are presented in order to investigate the effect of the solid-liquid molecular interactions on the flow. The choice of these materials is motivated by the recent interest in constructing BNNT [167–169] and SiCNT [22, 170] membranes, as first modelling results show that they could be strong competitors to CNT-based membranes in terms of permeability and selectivity [171–180]. Further, the MD results presented here are analyzed using a model recently developed by Mattia *et al.* [1] that makes explicit the dependence of the flow enhancement on both the tube geometry and the interactions between the nanotube wall and the flowing liquid. The combination of MD results and model sheds new light on the different physical effects that can help guide researchers in developing future nanotube membranes for specific applications.

4.1 Simulation setup

Molecular dynamics simulations of systems consisting of a membrane separating two water reservoirs that contain at least 25000 water molecules are conducted. The geometry of the simulated systems in this chapter is similar to the one presented in Chapter 3 (see Fig. 4.1). The main difference is that the membrane is made of either carbon, boron nitride or silicon carbide. The investigated nanotubes have a chirality of (15,15) in the case of CNTs and BNNTs, and (12,12) for SiCNTs. Taking into account the differences in bond lengths between these materials, the given chiralities correspond to a tube radius of 1.017 nm for the CNT, 1.036 nm for the BNNT, and 1.031 nm for the SiCNT. The thickness of the simulated membranes (i.e. the length of the nanotubes) is varied from 2.5 nm up to 50 nm. Periodic boundary conditions in all directions are applied, and the temperature in the reservoirs is controlled by Berendsen thermostats at a constant 298 K; in the longer (>25 nm) BNNTs and SiCNTs the z-component of the velocity is also thermalized along the nanotube in order to avoid excessive viscous heating. It takes around 7 days to simulate 1 ns of problem time on 24 CPU cores for nanotubes smaller than 12.5 nm, or 48 CPU cores for all other cases. The problem time for each of the MD simulations ranges from 10 ns to about 25 ns.

After an equilibration time of at least 5 ns, a pressure difference of 200 MPa between the two water reservoirs is imposed and then maintained constant. This high pressure difference enables steady state of the fluid flow to be reached in a reasonable time, thus reducing the computational cost of the simulations [18, 32, 144–147]. The Gaussian forcing method presented in Chapter 3 is used here in order to create the required pressure difference.

The LJ parameters of the water-carbon interactions for the CNT membranes are those calibrated in Chapter 2 (see Tables 4.1 and 4.2), chosen specifically for the TIP4P/2005 water model in order to reproduce the macroscopic contact angle of a water droplet on a graphitic surface, following the methodology of Werder *et al.* [48]. Water molecules interact more strongly with BNNTs and SiCNTs, compared to CNTs, due to the electrostatic forces caused by the materials' polarity. For the much weaker Van der Waals forces, represented here by Lennard-Jones interactions, the parameters used are from previously reported force fields and *ab initio* calculations for BNNTs [172]

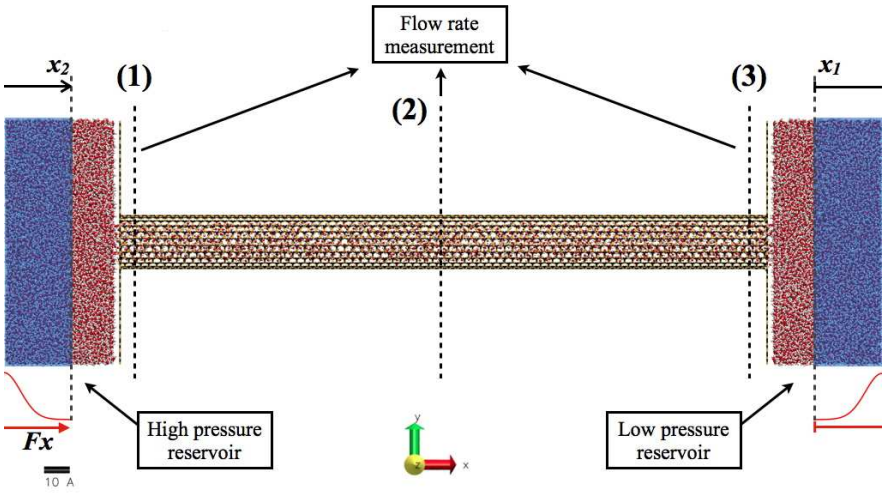

Figure 4.1: The flow system for MD simulation: a nanotube connects two reservoirs, with water flowing along the nanotube from the high pressure side (left) to the low pressure side (right). Blue shaded areas are the MD control regions, where temperature and pressure are controlled. During equilibration runs, the density is also controlled in the same regions. In steady state conditions, flow rate measurements at the indicated measurement planes perfectly match each other.

and SiCNTs [22, 180], along with Kong's mixing rules [181, 182].

Table 4.1: Lennard-Jones parameters between interacting atoms.

Interaction pair	σ (nm)	$\varepsilon \times 10^{21}$ (J)
O-O	0.315890	1.286750
C-O	0.319000	0.709302
C_{SiC}-O	0.327776	0.705867
N-O	0.326169	1.135040
B-O	0.330352	0.919718
Si-O	0.329339	2.201310

It is common in MD simulations not to have available potential parameters for mixtures of fluids or complex systems, like the one studied here, where a fluid interacts with a realistic, multicomponent solid surface. To overcome this problem, researchers use mixing (or combining) rules, until proper calibration of parameters is achieved from *ab initio* calculations and/or experiments. These rules predict the potential parameters characterising the interactions of two unlike molecules from parameters characterising each of the individual molecules. The most commonly used mixing rules are the

Lorentz-Berthelot (LB), which use the arithmetic mean in order to calculate the collision diameter:

$$\sigma_{ij} = \frac{\sigma_{ii} + \sigma_{jj}}{2}. \tag{4.1}$$

This rule is exact if the interacting molecules are hard spheres. The LB rules use the geometric mean for the calculation of the well depth:

$$\varepsilon_{ij} = \sqrt{\varepsilon_{ii}\varepsilon_{jj}}. \tag{4.2}$$

More sophisticated mixing rules like those of Kong [181] are:

$$\sigma_{ij} = \frac{\left[(\varepsilon_{ii}\sigma_{ii}^{12})^{1/13} + (\varepsilon_{jj}\sigma_{jj}^{12})^{1/13}\right]^{13/6}}{2^{13/6}(\varepsilon_{ii}\varepsilon_{jj})^{1/12}(\sigma_{ii}\sigma_{jj})^{1/2}}, \tag{4.3}$$

$$\varepsilon_{ij} = \frac{\varepsilon_{ii}\varepsilon_{jj}\sigma_{ii}^{6}\sigma_{jj}^{6}}{(\varepsilon_{ii}\sigma_{ii}^{12})/2^{13}\left[1 + \left((\varepsilon_{jj}\sigma_{jj}^{12})/(\varepsilon_{ii}\sigma_{ii}^{12})\right)^{1/13}\right]^{13}}, \tag{4.4}$$

and have been found to work better than other mixing rules, especially for predicting the correct viscosity of a mixture of fluids [182].

Table 4.2: Charges on atoms of polar molecules [22, 50, 172, 180].

Atom	q (e)
O	–
M	-1.1128
H	0.5564
C	–
C_{SiC}	-0.6000
N	-1.0500
B	1.0500
Si	0.6000

4.2 Measurement techniques

A series of flow property measurements are performed during each MD simulation at every time-step, and the reported steady-state results have always been time-averaged over at least 2.5×10^6 time-steps. Flux measurement planes are placed as shown in

Fig. 4.1 to measure the net mass flow rate $\dot{m}$ (kg/s) along the nanotube. The mass flow rate is calculated according to Eq. (3.13).

Representative examples of the mass flow rate measurement are given in Fig. 4.2. The examples in this figure are from nanotubes of various lengths, and for all the materials studied here. The values shown in the figure are not the final ones reported and used in the following sections, but, they clearly show that after steady state conditions have been reached measurements for a given nanotube at all three planes in Fig. 4.1 agree.

In order to compare the water flow performance of the various nanotube materials, the mass flow rate in every system was measured under the same conditions. Temperature, pressure and density control in the reservoirs lead to the desired target values, within 0.5% accuracy, for all the different nanotube systems simulated here. Table 4.3 lists the equilibrium values inside the high and low pressure reservoirs for simulations of membranes consisting of all the different materials studied here.

Table 4.3: Averaged pressure, density and temperature inside the high and low pressure reservoirs. The reported values are for all the studied materials of nanotubes.

	CNT		BNNT		SiCNT	
	High	Low	High	Low	High	Low
$\bar{P}$ (MPa)	228	29	220	19	223	23
$\bar{\rho}$ (kg/m^3)	1072.2	998.1	1073.1	997.8	1074.4	999.4
$\bar{T}$ (K)	298.0	298.1	298.1	298.1	298.1	298.1

Characteristic axial profiles of temperature, pressure and density, along with the streamwise velocity profile measured and averaged across the nanotube's diameter are given in Fig. 4.3. The presented profiles are from simulations of 25 nm long nanotubes of all the tested materials here. Figure 4.3a shows the minimal frictional losses inside the CNT, compared to the losses in the two other types of nanotube, and highlights that most of these pressure losses are attributable to entrance effects. Although the water density in the CNT is lower than in the BNNT and SiCNT (see Fig. 4.3b), so there are fewer water molecules at any given time inside the nanotube, the measured flow rate is higher as they travel with a much higher streaming velocity (see Fig. 4.3c). The results shown in Fig. 4.3 are from an early stage of the steady-state sampling period, and those for the CNT are averaged over fewer time-steps compared to the

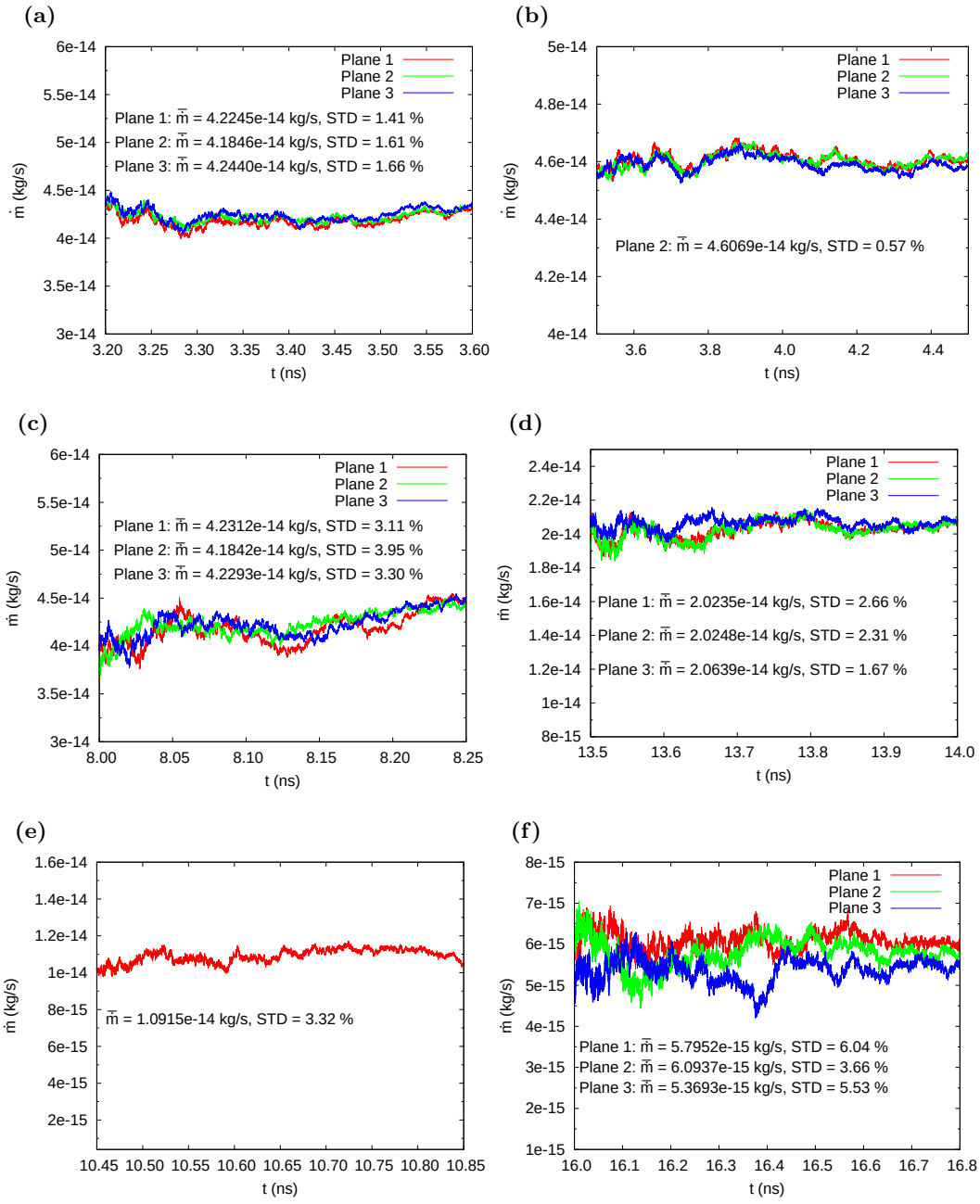

Figure 4.2: Mass flow rate measurements for various nanotube lengths and materials. When only one line is presented, this is from the middle plane (2) in Fig. 4.1. **a, b, c,** CNT membranes of thickness 12.5, 25 and 50 nm, respectively; **d, e,** BNNT membranes of thickness 12.5 and 50 nm, respectively; **f** SiCNT membrane of thickness 50 nm.

other materials, explaining the larger oscillations. At the final stage of the sampling period the equivalent profiles are significantly less noisy, while the mean value of each quantity is not altered.

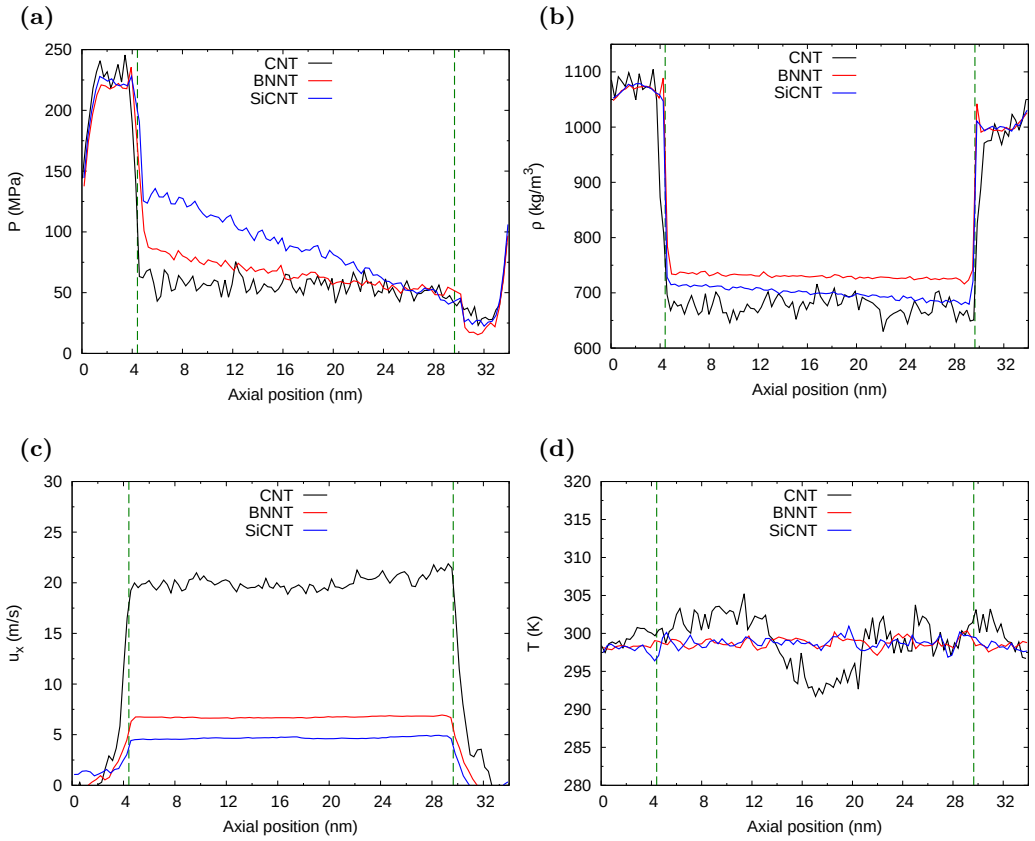

Figure 4.3: Axial profiles of different water quantities in 25 nm long nanotube membranes made from all the studied materials. The green dashed vertical lines show the positions of the entrance and exit of the nanotube. **a, b, c, d** Pressure, density, streaming velocity and temperature profiles, respectively, along the nanotube axis.

Radial density and velocity profile measurements provide further insight into the water structure inside the nanotubes and how the various tube materials affect the flow behavior. Each nanotube is divided into 100 radial cylindrical bins, and the density and the velocity are measured inside every bin over the full length of the nanotube, from the first flux measurement plane up to the third one. The results are averaged over a large number of MD time-steps.

Water axial self-diffusivity is also measured inside the nanotubes under equilibrium MD simulations, before any pressure difference is applied. Two equivalent methods to calculate the self diffusivity of a liquid or gas are often used [36], the first one based on the time integration of the velocity autocorrelation function, and the second based on calculating the mean-squared displacement. In this thesis the former was chosen, and

D_s is calculated with the Green-Kubo expression:

$$D_s = \frac{1}{3N} \int_0^\infty \sum_{i=1}^{N} \langle u_{i,x}(t) \cdot u_{i,x}\left(t + t'\right) \rangle dt', \tag{4.5}$$

where $u_{i,x}(t)$ is the axial centre of mass velocity of molecule i at some time t, and $\langle ... \rangle$ denotes the ensemble average. Equation (4.5) is an average over all N water molecules. The autocorrelation function decays quite quickly, and then fluctuates around zero, so a small time window of a few time-steps is enough to calculate D_s. A production simulation contains thousands of sampling time windows, and the reported values of D_s are averaged over all the collected samples. The same measurements are then repeated in steady flow conditions under an applied pressure difference, and show no significant difference. So pressure-driven flow inside nanotubes does not further alter water's self diffusivity [146], beyond that of the effect of confinement (see also Section 4.3 below). From its self-diffusivity, the water viscosity μ can be calculated by using the Stokes-Einstein relation [122, 177, 183]:

$$\mu = \frac{k_B T}{3\pi\omega D_s}, \tag{4.6}$$

where k_B is Boltzmann's constant, T is the water temperature, and $\omega = 1.7\,\text{Å}$ is the effective hydrodynamic diameter of a water molecule, which is calculated from the average positions of hydrogen atoms and charge sites relative to the oxygen atom in the TIP4P/2005 water model [52, 183].

Finally, the work of adhesion W_A, which is the potential energy from the interaction of the first water layer with the nanotube atoms divided by the nanotube surface area, is easily measured. The potential energy of every atom is readily available in MD simulations, as this is at the core of the MD algorithm. As a result, no special measurement technique is needed beyond a summation of the potential energy of water molecules due to their interaction with the nanotube atoms in an annular region close to the nanotube wall.

4.3 Results and discussion

Figure 4.4(a) shows the structure of the water molecules inside carbon, boron nitride and silicon carbide nanotube cross-sections, taken from characteristic simulations of membranes with 25 nm long nanotubes. In all cases, a highly ordered and packed layer of water molecules is formed close to the inner nanotube walls. This is more apparent from the radial density profiles in Fig. 4.4(b). This arrangement lends itself to the idea of modeling water inside the nanotubes as a two-fluid system, with a fluid viscosity in the annular region close to the wall that is distinct from the bulk fluid viscosity close to the tube's axis. The thickness of the annular region is very similar for all nanotube materials studied at $\delta = 0.5$ nm, which includes the "empty" (depletion) region along with the first high-density water layer (Fig. 4.4), in agreement with previous MD work [19, 183]. The averaged velocity profile across each nanotube is presented in Fig. 4.4(c). It is seen that water flows with minimum viscous losses and has a plug-like velocity profile for all three simulated materials. This is reflected in the variation of the flow rate with the pressure gradient for the three materials tested (Fig. 4.5), with CNTs showing a significantly higher flow rate than BNNTs and SiCNTs. The deviations in this figure for the shortest tube lengths are attributed to a dominating effect of entrance losses in short tubes, as shown in the recent literature [18, 32, 159].

To understand the difference in flow rates for the different nanotube materials, the MD results are analysed using a model recently developed by Mattia *et al.* [1] that makes explicit the relationship between flow enhancement (defined as the ratio of the measured MD flow rate to the conventional Hagen-Poiseuille prediction with no-slip boundary conditions, $\epsilon = \dot{Q}_{measured}/\dot{Q}_{HP}$) and the strength of the solid-liquid interactions occurring at the nanotube walls:

$$\epsilon = \left(\frac{R-\delta}{R}\right)^4 \left(1 - \frac{\mu_{Bu}}{\mu_W}\right) + \frac{\mu_{Bu}}{\mu_W}\left(1 + 8\mu_W \frac{\mathrm{L}}{R^2}\frac{D_s}{W_A}\right), \tag{4.7}$$

where L is the length of the nanotube, R its radius, μ_{Bu} is the bulk viscosity of the fluid, μ_W is the viscosity of the fluid in the annular region near the tube wall (where the effect of the solid-liquid molecular interactions is strongest), and D_s and W_A are the self-diffusivity of water molecules and the work of adhesion between the liquid and

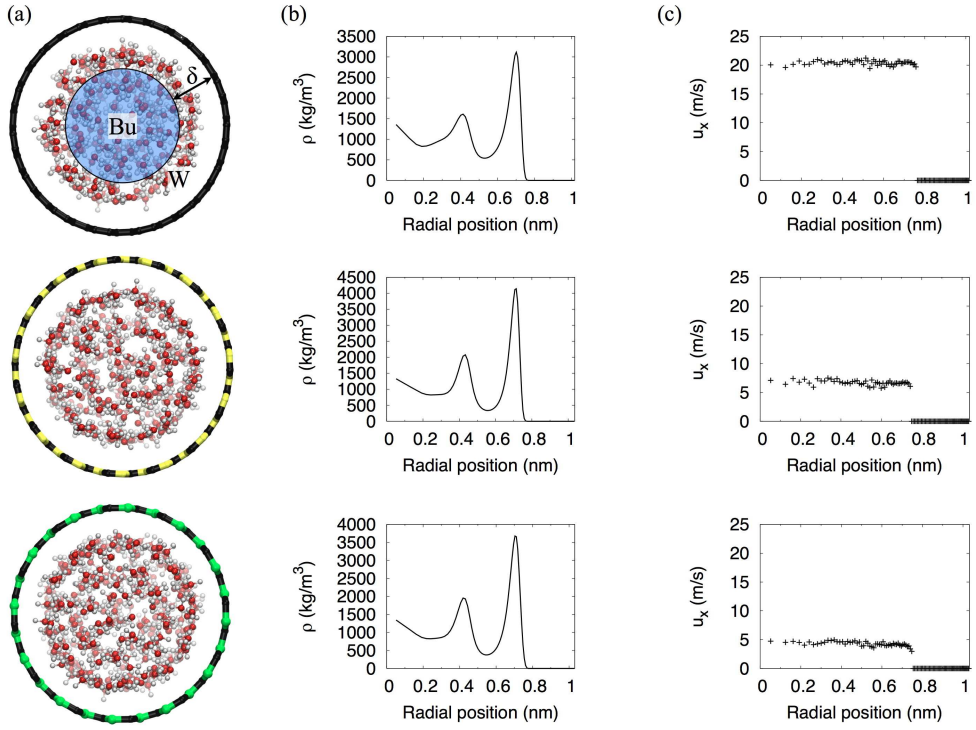

Figure 4.4: (a) Cross-section snapshots of the three different nanotubes transporting water molecules. The nanotube material of the top snapshot is carbon, the middle is boron nitride, and the bottom is silicon carbide. The bulk region (Bu) is illustrated with light blue shading, and the annular region (W) (where the viscosity is reduced) has a thickness $\delta = 0.5$ nm, constant for all materials. (b) Water density profiles across the nanotube radii showing the concentric water ring structure. (c) Velocity profiles across the nanotubes for the same applied pressure difference of 200 MPa.

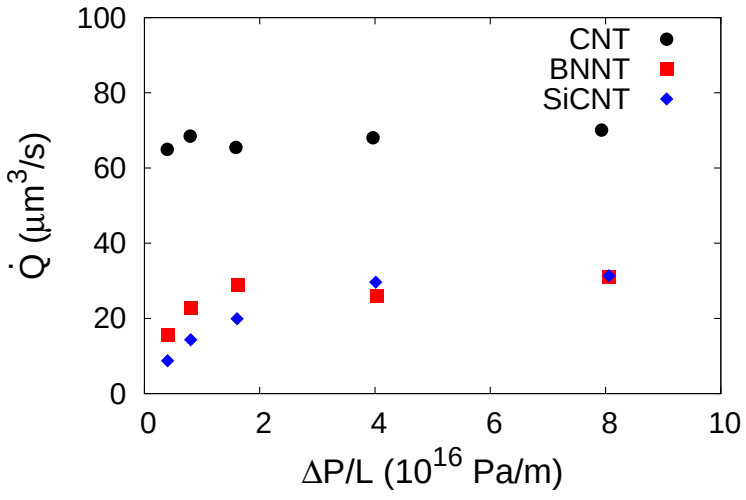

Figure 4.5: Volumetric flow rate ($\dot{Q}$) versus pressure gradient ($\Delta P/\mathrm{L}$) for the three nanotube materials tested. CNTs show a 2- and 4-fold higher flow rate than BNNTs and SiCNTs, respectively, for the same pressure gradient. Standard deviation of all data points is smaller than 5%, with error-bars covered by the data-point symbols themselves. The standard error of the mean is smaller than 0.01% for all reported values.

the channel wall, respectively. This model is based on the Hagen-Poiseuille equation but takes into account the molecular solid-liquid interactions, the tube geometrical characteristics, and water properties inside the nanotube. It has shown good agreement with previously-reported experimental and computational results for carbon [1] and inorganic [184] nanotube materials. Details of the derivation of Eq. (4.7) can be found in Ref. [1].

This equation contains no fitting parameters: as noted above, δ has been found to be the same for all three cases (Fig. 4.4), while D_s and W_A are constant values for any given solid-liquid couple and flow conditions. Both can be measured experimentally (for example, W_A can be measured via immersion calorimetry) or calculated via MD as shown in Fig. 4.6. The viscosities μ_{Bu} and μ_W are calculated from MD results using the Stokes-Einstein relation for water in both the bulk and the annular regions close to the wall, respectively, following an established MD methodology [122, 183]. Table 4.4 reports the averaged values calculated from MD for each nanotube material. This table shows that the fluid viscosity close to the nanotube wall is always lower than the viscosity calculated in the center of the tube (the bulk flow). Furthermore, the bulk values differ from the value measured for the same water model in an unconfined environment [51], so it can be deduced that confinement has a significant effect on the water viscosity [122].

A measure of the reliability of calculating D_s and W_A through MD simulations can be obtained by comparing the MD results for CNTs of this chapter in Fig. 4.6 and Table 4.4 with published data [1]: W_A for water on graphite (measured via immersion calorimetry) is 97×10^{-3} N/m; D_s for water on graphene and through graphitic slit pores has been found to be $2-4\times10^{-9}$ m^2/s [185]. To the author's knowledge, independent measures of these properties for boron nitride and silicon carbide are not yet available in the literature. However, Fig. 4.6 clearly shows that MD is able to retrieve the values for water on carbon.

Table 4.4: Average water properties calculated via MD for each nanotube material.

Material	$D_s \times 10^9$ (m^2/s)	$W_A \times 10^3$ (N/m)	$\mu_W \times 10^4$ (Pa s)	μ_W/μ_{Bu}
Carbon	3.14 ± 0.18	98.7 ± 0.42	7.02	0.29
Boron nitride	2.48 ± 0.10	184.0 ± 1.76	9.09	0.56
Silicon carbide	2.33 ± 0.06	164.5 ± 1.53	10.27	0.73

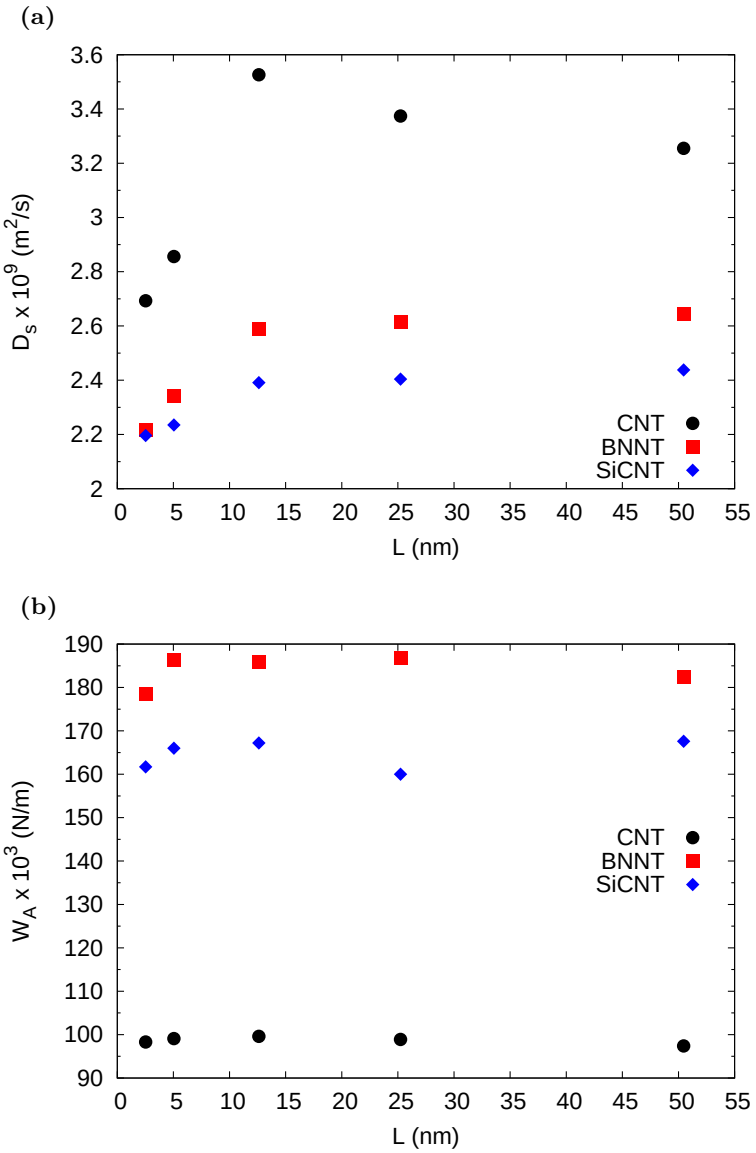

Figure 4.6: **a,** Total self diffusivity of water inside the nanotubes for all the studied nanotube materials and lengths. **b,** Work of adhesion as measured for all the cases studied in this chapter.

In Fig. 4.7 the flow enhancement data is plotted against the ratio D_s/W_A, which represents the strength of the solid-liquid interaction for each of the nanotube materials tested. A reasonable linear fit through all data points confirms what MD, experimental results and Eq. (4.7) have previously suggested: the more hydrophobic the material comprising the nanotube walls, the higher the flow enhancement (for a polar liquid such as water).

In Fig. 4.8 the flow enhancement data for the three nanotube materials is re-plotted

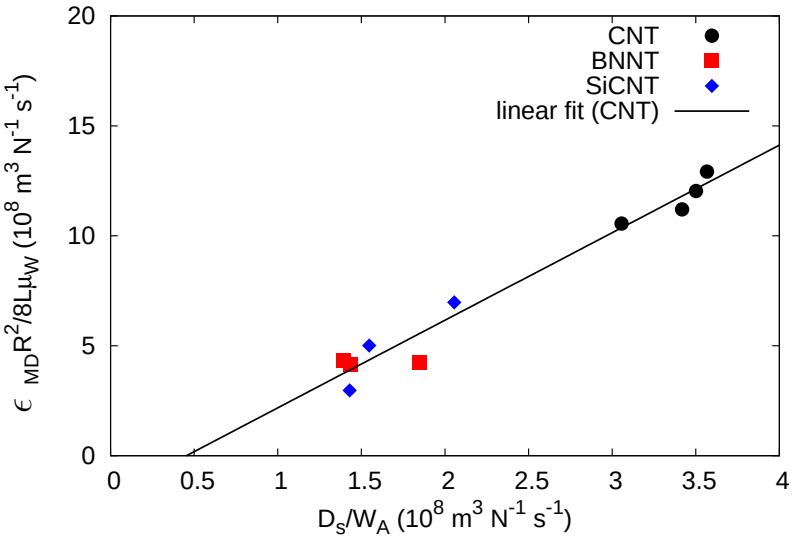

Figure 4.7: Normalized flow enhancement as a function of the strength of solid-liquid interactions (represented by the ratio D_s/W_A).

as a function of the tube aspect ratio (L/D) to highlight the linear dependence shown by both the MD results and the model. A deviation between the two for the shortest tubes is explained by the significant entrance losses, as previously discussed. This same linear dependence has been observed in MD results for CNTs of comparable lengths [32]. Whether the dependence remains linear for much longer tubes is still a matter of debate: experimental results for very long tubes have shown proportionately high enhancement values ($\sim 60,000$ for $125\,\mu$m CNTs [186], and $\sim 400,000$ for 4 mm long CNTs [187]). A recent publication, on the other hand, indicates that, while the dependence is linear for tubes of comparable length to the ones analysed here, there is a plateau in the flow enhancement for micrometer (or longer) CNTs. This is attributed to a combination of entrance/exit losses and internal losses due to friction [18]. A further development of the model Eq. (4.7) to include entrance/exit losses may serve as a better flow prediction tool in nanotubes of various materials. Addressing this issue requires further MD and experimental investigation; some of the former are presented in Chapter 6 from hybrid MD-continuum simulations.

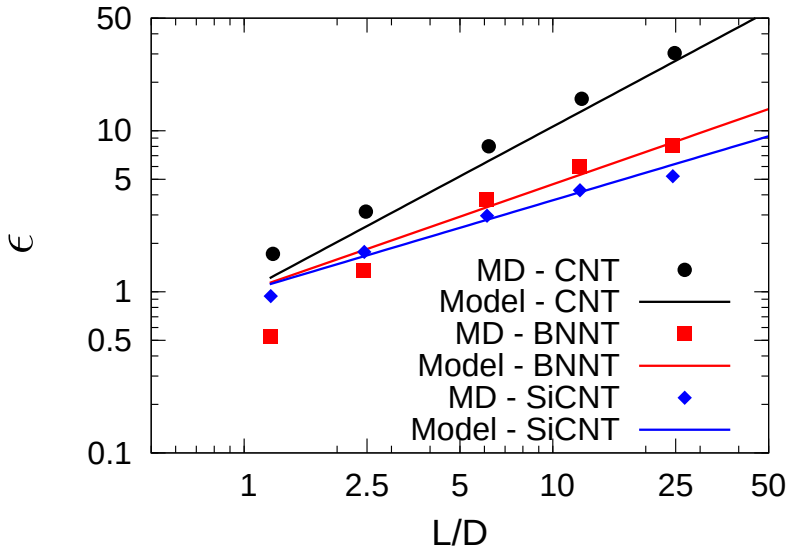

Figure 4.8: Flow enhancement ϵ as a function of tube aspect ratio L/D for CNTs, BNNTs and SiCNTs of comparable diameter ($\sim$2 nm). The model results for each material have been calculated using Eq. (4.7) and data from Table 4.4. Standard deviation of all MD data points is smaller than 5%, with error-bars covered by data-point symbols themselves. The standard error of the mean is smaller than 0.01% for all reported values.

4.4 Summary

This chapter presented MD simulations of water flow in nanotube membranes made of three different materials, carbon (CNT), boron nitride (BNNT), and silicon carbide (SiCNT). Water flow properties were analysed and the effect of solid-liquid molecular interactions on them was highlighted. The favorable flow conditions inside the CNTs resulted to higher flow rates than those observed in BNNTs and SiCNTs under the same external conditions. Finally, an analytical model was tested against the MD results giving satisfactory predictions of the flow enhancement factors for nanotube membranes of small thickness. However, additional development of the model is needed in order to be applicable to membranes with a nanotube length of practical engineering interest.

Chapter 5

Multiscale hybrid simulations

Πάντα κατ' αριθμόν γίγνονται.
- Πυθαγόρας (580-490 π.Χ.)

All is number.
- Pythagoras (580-490 B.C.)

High-accuracy molecular approaches like the MD technique are limited to the study of very small systems, $\mathcal{O}(100\ \mathrm{nm}^3)$, for very short timescales, $\mathcal{O}(100\ \mathrm{ns})$ due to the high computational cost. Because of this, multiscale methods have recently been developed in order to retain the accuracy of MD within simulations of much larger systems for longer times. In this chapter, a short review of two major multiscale techniques — the Domain Decomposition Method (DDM) and the Heterogeneous Multiscale Method (HMM) — is presented.

Despite their extensive study and development, both DDM and HMM are not able to efficiently simulate the applications addressed in this thesis. An additional multiscale method, specifically designed to study flows in nanoscale networks, is therefore presented in section 5.4. This recent method, named the Internal-flow Multiscale Method (IMM), is applied in the following chapter to the problem of water flowing in very long nanotubes.

5.1 Introduction to multiscale methods

The idea of combining different numerical methods or mathematical models in order to address problems that cannot be efficiently and/or accurately modelled is not new [188–199]. The resolution of conventional CFD is not sufficient to capture phenomena that occur close to the molecular level, even though these can significantly alter the macroscopic fluid behaviour. On the other hand, high accuracy methods that are able to capture molecular interactions (such as MD) demand great computational resources. In addition, the small time-step ($\delta t \sim 10^{-15}$ s) of the MD simulations often does not allow a simulation to reach problem times that some phenomena in macroscale applications typically require.

Various multiscale models have been proposed, with the majority of them requiring a spatial scale separation between the micro and the macro solver. Spatial scale separation exists when microscale phenomena are only weakly coupled to the behaviour of macroscale phenomena. Under these conditions, the macro solver is able to resolve the flow on the larger scale in one part of the simulation domain of size X, while the micro solver resolves microscale phenomena in another part x, with $X \gg x$. Equivalently, time scale separation exists when microscale phenomena evolve much faster than macroscale ones. Time scale separation can be exploited through each solver using its own time-step and, as a consequence, resolving the different time scales of the simulated problem [200].

The commonly-used domain decomposition methods (DDM) rely heavily on spatial scale separation, with the computational domain divided into overlapping regions. In one region the conventional CFD solver is applied, and in the other the high-accuracy method, i.e. MD. A detailed presentation of this method will be given in section 5.2.

A more recent method that decouples both spatial and temporal scales has been proposed by E *et al.* [201–204], called the heterogeneous multiscale method (HMM). This method differs from the domain decomposition method in that the whole domain is covered by the macro solver grid. The micro solver enters as a local refinement at the nodes of the macroscopic domain and provides the data needed (e.g. stress tensor, slip velocity) by the macro solver. A key advantage of this approach is that if the problem is time scale separated then the two solvers in this method can evolve with different

time-steps, naturally decoupled, and so large scale dynamical problems can be studied. A detailed presentation of this method and its advantages and disadvantages will follow in section 5.3.

The final multiscale method, presented in section 5.4, is the internal-flow multiscale method (IMM) developed by Borg *et al.* [58, 60] for high-aspect-ratio channel or pipe geometries. Based on the same principals as the HMM, the IMM can successfully decouple both space and time scales (for time scale separated problems) in order to provide significant computational savings. In this method, long channels in a network are replaced by much smaller, but representative, MD simulations. Junction components, however, do not exhibit the necessary length-scale separation, and so they are entirely simulated using MD. In IMM, all network elements are coupled together within the same simulation by using continuum conservation laws.

To the author's knowledge, there is no single multiscale approach that will outperform all others for any given problem. A common differentation between multiscale problems is that according to E and Engquist [201]. *Type A* problems are those where the macro solver is capable of producing an accurate solution for most of the domain, and the micro solver is only needed locally around singularities or close to interfaces. Examples include contact line dynamics, problems with complex fluid-solid interactions, and chemical reactions. In *Type B* problems the micro solver is needed everywhere in order to complement the macro solver. The simulation of non-Newtonian fluids is a characteristic example of a *Type B* problem. So DDM is well suited for *Type A* problems, while HMM can handle both *Type A* and *Type B*, or a mixture of the two problems.

Because there are numerous studies and variations of each multiscale method, this chapter will focus on the main principals of each approach, and only reference the latest developments. The multiscale methods presented here are also called *hybrids* as different type of solvers can be involved, with any mix of models being possible. For clarity in this thesis the micro solver refers to MD, while the macro solver refers to a continuum fluid solver. In addition, both isothermal and non-isothermal, compressible and incompressible problems can be addressed with the presented methods. However, as the main purpose of this thesis is the study of water flow inside or over nanostructures

for applications such as desalination and filtration membranes, the methods will be presented under the hypothesis of incompressible and isothermal flows.

5.2 Domain Decomposition Method (DDM)

The DDM is based on a simple intuitive idea, well suited to *Type A* problems. The computational domain is divided into smaller subdomains and a separate solver is used in each subdomain, ensuring that the solutions match each other at their spatial interfaces. In order to achieve this, a proper coupling is required between the highly distinct fluid descriptions and this is the principal challenge of this multiscale approach. The physical fluid quantities (density, momentum, and energy) as well as their fluxes are continuous across the interfaces, with the subdomains providing each other with boundary conditions. The spatial and temporal averages of quantities can be easily calculated during the MD simulations and these values can be imposed as boundary conditions on the continuum solver. However, defining boundary conditions for the MD solver through continuum values is not as straightforward.

In this section a description of the two main types of DDM is given, distinguished from each other by the coupling approach between the continuum and the MD subdomains: state variable coupling, or flux exchange coupling. In order to avoid generating local structuring in the fluid due to domain termination, the MD domain is allowed to overlap the continuum domain at their interface. Therefore three regions exist: a region of pure MD (Ω_A), a region of pure continuum solver (Ω_C), and an overlapping region (Ω_O), as illustrated in Fig. 5.1 for a state-based coupling approach. In this overlapping region, both descriptions should be valid and consistent. The extent of Ω_O is crucial, as is ensuring the continuity of thermodynamic and transport properties across the solvers' interfaces [198].

For isothermal flows, the major challenge in state-based coupling is in linking the continuum stress field to a representative atomistic description in order to accomplish momentum continuity. The atomistic representation of stress is based on the momentum flux of molecules across a surface element moving at the local velocity, and also on the forces acting between the molecules on either side of the surface. These two compose the kinetic and the virial terms of the microscopic stress tensor [34]. In this

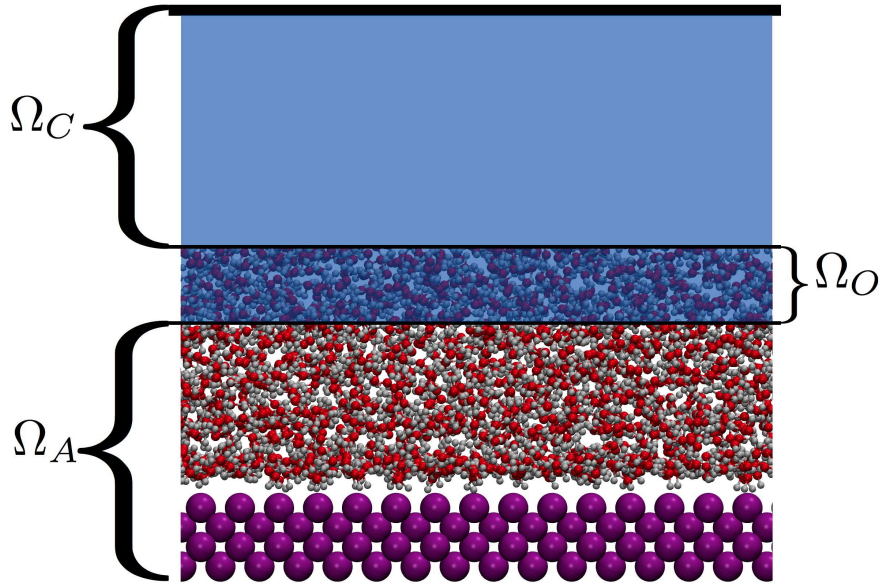

Figure 5.1: Illustration of a DDM (state variable coupling) for water flow over a solid wall. Light blue shading indicates the region where the continuum solver is applied, while the MD subdomain is indicated by the atomistic representation of the fluid and wall molecules; Ω_C is the continuum subdomain, Ω_A is the MD subdomain, and Ω_O is the overlap region.

type of method, the length scales and magnitudes of the corrective forces that must be applied to the molecules are important in order to fulfill stress continuity. To ensure that the velocity fields are consistent, the average momentum of the molecules in the overlapping region is relaxed to that of the corresponding continuum solver by constraining the molecular velocities. More details of the application and performance of the multiscale DDM are given in O'Connell and Thompson [205].

This approach has two serious limitations: it cannot cope with mass transfer across the interface, and the timescales of the solvers are fully coupled (with both using the micro solver's time-step). Hadjiconstantinou and Patera [206] address these problems with a DDM for incompressible flows that can deal with mass transfer across the coupling interface and that, more crucially, allows timescale decoupling due to the use of the alternating Schwarz method. The overlapping region permits the exchange of information between the continuum and MD subdomains in the form of Dirichlet boundary conditions. Initially a guess is made for the boundary conditions of the continuum solver and a steady-state solution is obtained. This is then used to generate boundary conditions to the MD subdomain from which a steady state solution is obtained. The iterations continue, with steady-state continuum solutions obtained using bound-

ary conditions taken from micro MD simulations, and MD solutions obtained by using boundary conditions taken from the continuum subdomain. A single Schwartz iteration consists of this two-way exchange of boundary conditions. A number of Schwartz iterations are performed until convergence is achieved, i.e. the solutions obtained by the macro and micro solver in the overlapping region are identical. This approach is suitable for steady-state problems, but the Schwartz coupling method could be extended to dynamic problems if the solution proceeds in steps of quasi-steady-state solutions.

Another difference between the two approaches outlined above is how they achieve consistency of velocity field inside the overlapping region. Instead of constraining the molecular velocities in order to impose the continuum velocity boundary condition, Hadjiconstantinou and Patera's method draws molecular velocities from a Maxwellian distribution with a mean and a variance consistent with the continuum fluid velocity and temperature. Such a "Maxwell Demon" approach was found to perform better than restricting molecular velocities.

The last state variable coupled DDM that will be described here was presented by Werder *et al.* [207]. These researchers introduced a new expression for the boundary force applied on the molecules inside the overlapping region. (This force prevents the molecules from flying away from the overlapping region.) Contrary to the common practice of using periodic boundary conditions in pure MD simulations, some hybrid models require non-periodic boundaries. Ideally, these boundary conditions would guarantee that the correct mean pressure is applied to the MD subdomain and also that any local field disturbances are minimised. While the application of the mean pressure is a compulsory requirement for proper modelling, the minimisation of local field disturbances strongly influences the size of the overlapping region, and as a consequence the computational cost.

The major innovation of the model proposed by Werder *et al.* [207] is that the boundary force accounts for the local structure of the fluid. This is achieved by incorporating the radial distribution function $g(r)$ as a weighting function for the forces applied normal to the interface between the overlapping and the continuum regions. Essentially, using the weighting $g(r)$ substitutes for the missing interatomic forces and potential energy contributions from molecules that would be present if the MD region

did not end at the interface limit and was further extended in the continuum subdomain.

Even after the application of the boundary force, molecules might still leave the overlapping region. To prevent this, a specularly reflecting wall condition is applied at the boundary of the overlapping region: the molecular velocity component normal to this wall condition is reversed on molecular impact. Such an impermeable wall ensures that the overall number density of molecules in the MD subdomain remains constant. The specular wall can be viewed as a plane of symmetry, where the reflected molecules represent those entering from a virtual reservoir. In this hybrid method the continuity of velocity across the solver interface is based on constraining the molecular velocities, as in the approach given in [205].

The other main type of DDM is based on the direct exchange of fluxes, and was first introduced by Flekkoy *et al.* [208]. Figure 5.2 shows a representative illustration of the MD (Ω_A), continuum (Ω_C) and overlapping (Ω_O) domains. Molecular fluxes are imposed on the continuum solver inside the region $\Omega_A \rightarrow \Omega_C$, while the continuum fluxes are applied on the molecules in the region $\Omega_C \rightarrow \Omega_A$. In this way, flow out of one subdomain flows into the other. This includes mass and momentum fluxes and so conservation laws are naturally fulfilled. The addition of a buffer region between the subdomains, where fluxes are exchanged, was later added in an improved version of this DDM [209]. The number of molecules is kept constant inside the buffer region by molecule addition, or removal, depending on the molecular flow between the buffer region and Ω_A. In addition, a force is applied on the molecules in the buffer region in order to enforce momentum boundary conditions into Ω_A.

The DDM was the first approach towards a multiscale hybrid solver that would combine the accuracy of MD with the computational efficiency and simulation sizes of continuum fluid dynamics. A detailed review of all the variations of DDMs presented in this section, including algorithmic details, example cases and an extensive reference list, was presented by Mohamed and Mohamad [198]. Although this method is well suited to solve *Type A* problems, it cannot handle *Type B* problems nor the problems this thesis addresses. However, aspects of this approach, such as the communication between the micro and macro solvers (and vice versa), are used in more recent multiscale methods

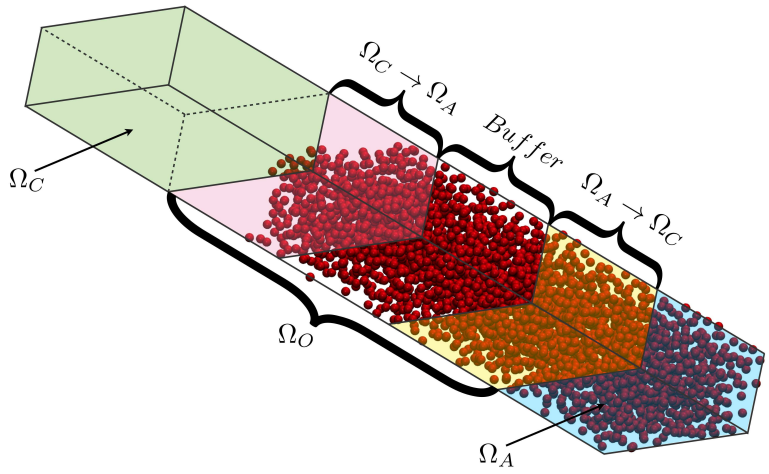

Figure 5.2: Representative illustration of the DDM based on direct flux exchange. The continuum solver is applied in the green region (Ω_C), and the MD solver in the blue region (Ω_A). An overlapping region (Ω_O) exists between Ω_C and Ω_A. Subdomain Ω_O is further divided into three regions, namely $\Omega_C \rightarrow \Omega_A$, $\Omega_A \rightarrow \Omega_C$ and the buffer. The latter region is not present in all flux-exchange-based DDMs, as it was introduced more recently in [209].

that will be presented in sections 5.3 and 5.4.

5.3 Heterogeneous Multiscale Method (HMM)

As mentioned in section 5.1, *Type B* problems require the presence of a micro solver everywhere in the simulation domain, to complement the macro solver (see Fig. 5.3). A suitable approach for solving this type of problem is the Heterogeneous Multiscale Method (HMM) by E *et al.* [201], Yasuda and Yamamoto [210], and Asproulis *et al.* [211]. In this type of multiscaling the objective is to employ micro resolution rather than micro-macro decomposition. In other words, the domain is entirely described by the macro solver, with small isolated micro domains distributed across the domain that provide missing information to the macro solver locally. The HMM can, in fact, also be applied to *Type A* problems, or a combination of both *Types A* and *B*, without any performance or accuracy loss when compared to DDM [212].

HMM can be understood as fluid constitutive modelling through local isolated micro (i.e. MD) simulations. The macro model in the HMM approach is incomplete and no assumption is made regarding the unknown constitutive relations or boundary conditions. The microscale model is therefore invoked during the computation to supply whatever data is missing but required for the macro solver. The macrostate of the

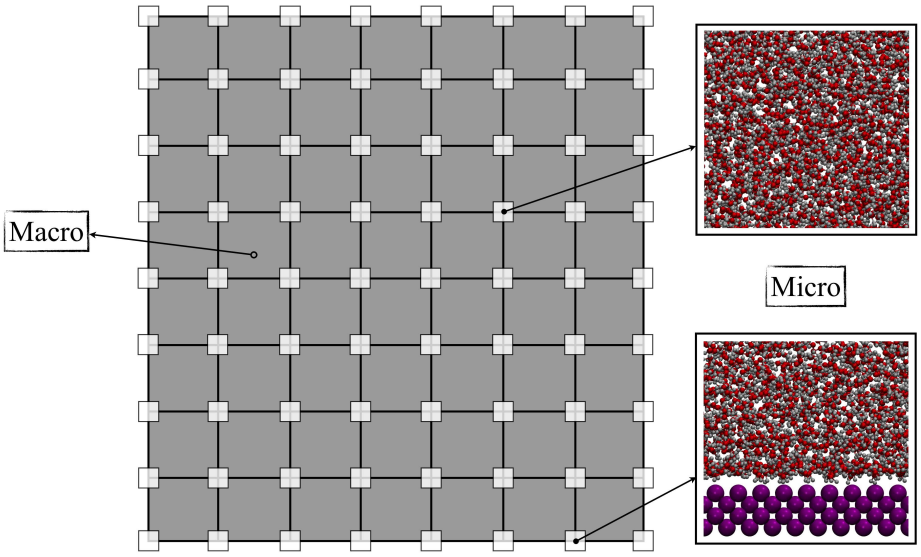

Figure 5.3: Schematic of the HMM. The grid of the continuum solver is represented by black lines while microscopic (MD) simulations are performed at every grid node (light grey squares). Characteristic snapshots of flow and wall micro simulations are shown in the insets.

microscale model should be the same as the macrostate the user is interested in and, as a consequence, the microscale model has to be constrained. In other words, the average momentum of the molecules is relaxed to that of the macro (i.e. continuum) solver, as it is done in the overlapping domain of the DDM. The HMM is therefore composed of the following two components:

(1) *A macroscopic solver.* Depending on available knowledge about the macroscale behaviour of the system, the form of the macroscale model can be assumed, for which a suitable macro solver can be selected. For instance, in the case of an incompressible isothermal polymeric fluid flow, the hydrodynamic conservation equations (for mass and momentum) are solved in order to obtain the macroscale velocity field. The unknown data in this case is the fluid stress.

(2) *A procedure for estimating the missing macroscale data using the microscale model.* Commonly this is done is two steps: namely the constraint of the microscale simulation, and the processing of the microscale data. At each computational grid point of the macro mesh where macroscale data is needed, a MD simulation is performed where molecular velocities are constrained by the local velocity gradient according to the continuum strain-rate field. Then, the results from the MD simulation are used to extract the macroscale data needed by the macro solver. In the example of polymeric

fluid flow, the shear stress is measured in MD simulations in the bulk of the fluid region, while MD simulations close to the wall provide accurate values of slip velocity and shear stress. Commonly, researchers employ the Irving-Kirkwood formula in order to calculate the shear stress during the MD simulations [37].

Spatial scale separation is exploited by observing that in the data estimation step, the computational domain for the microscopic model can be totally decoupled from the computational domain for the macro solver. MD simulations only have to be large enough to guarantee the required accuracy for the data and avoid any unrealistic correlations. For the same reason, there is no direct communication between the various MD simulations at different spatial locations; all communication is done through the macro solver.

Until this point the scale separation capabilities of the hybrid multiscale methods have been outlined without taking into account the possibility of time scale separation. The most common approach to time advancement in hybrid multiscale solvers is to set the time-step of the macro solver equal to that required by the micro solver. In this case temporal scale separation is not exploited, and the computational cost can be much higher than needed.

The first improvement is to increase the time-step of the macro solver and exchange macro/micro information less frequently. The macro time-step should be small enough to accurately resolve the macroscopic variation in coupling variables, but larger than the time-step required by the micro solver. Even with this improvement temporal scale separation is not exploited. The HMM approach introduces a further improvement when the time needed by the micro solver to reach a quasi steady state is much smaller than the required macro solver time-step. In this case a substantial number of micro solver time-steps can be skipped, leading to significant computational savings.

In HMM, the two solvers evolve using different time-steps, with the macro solver using a much bigger (commonly by a factor $\sim 10^{15}$) time-step Δt_M compared to the microscale one Δt_m. The MD simulation should be run until it is sufficiently relaxed. In the case of time scale separated problems, this requires less time than the macroscopic solver time-step. Then information is exchanged between the models and the macroscopic model can be advanced by Δt_M (see Fig. 5.4). A key drawback of the original

HMM approach, though, is the need for reinitialisation of the microscopic model every time that it is invoked.

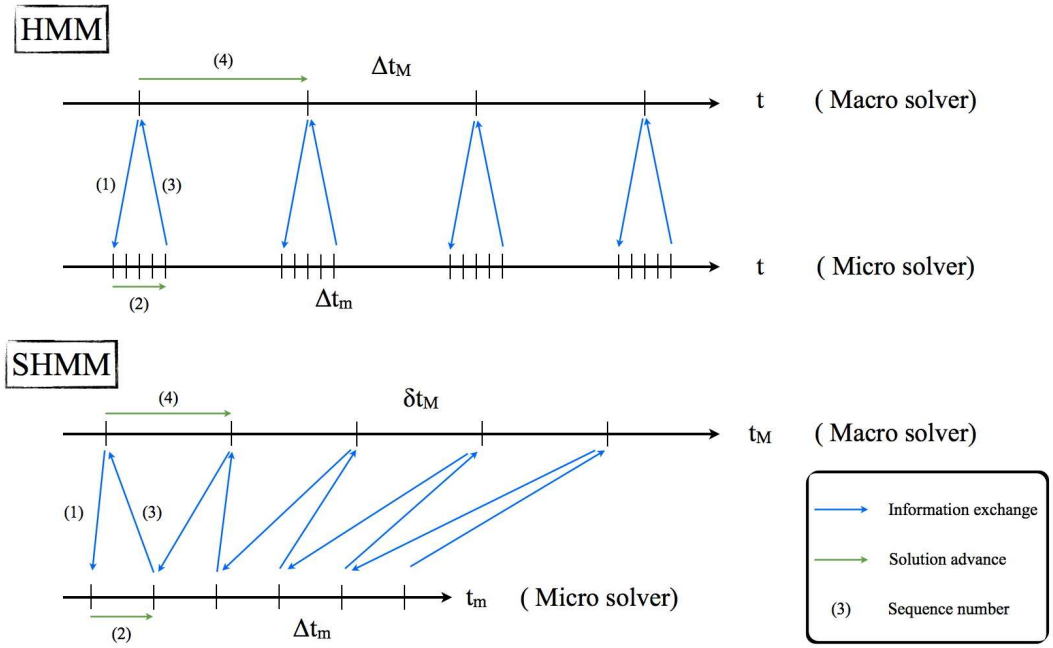

Figure 5.4: Schematic of the HMM and SHMM algorithms. In HMM both the macro and the micro solvers run with the same clock, leading to the same problem simulation time t. In SHMM the separate clocks of the solvers result in different simulation times t_M and t_m, with the macro solver's timescale (t_M) being the one the user is generally interested in.

In a further development of HMM, E *et al.* [212] simplified the algorithm and eliminated the reinitialisation requirement. To achieve this, the macroscopic time-step is given by $\delta t_M = \Delta t_M / M$, where M is a number larger than the number of steps the microscopic solver needs in order to reach its quasi-equilibrium state. In this seamless HMM (SHMM) approach, the two solvers exchange information at every time-step and no reinitialisation of the microscopic model is needed. Lockerby *et al.* [200] give a detailed description of this temporal scale separation approach, and propose a new scheme that combines the advantages of both of these methods and that can be applied in both DDM and HMM. In their proposed scheme, communication between the micro and the macro solver can vary from HMM to SHMM during a single simulation, adapting to variations in the flowfield and allowing a flexible number of micro solver time-steps to be performed between coupling instances.

In Fig. 5.4 a schematic of the HMM and SHMM algorithms is presented in order to

highlight their differences and their timescale separation capabilities (when the problem allows it). In HMM both the macro and the micro solvers use the same "clock", but the micro simulations occur over a small part of the macro solver time-step. On the other hand, in SHMM each solver has its own "clock", enabling the micro solver to proceed continuously without the need for reinitialisation every few time-steps. This comes at a higher cost for the macroscale simulations — a smaller time-step has to be used in order to accurately resolve the dynamics of the macroscale quantities. The smaller macroscale time-step δt_M is required in order to guarantee that the microscale model will have sufficient time to adapt to changes in the macro-state and relax sufficiently. The overall computational cost is not significantly increased, however, as the micro solver is always the most computationally demanding element.

It should be noted that in SHMM the user no longer obtains accurate information at the microscopic level, but only for the macro-state variables [212], which in most cases is the information needed for engineering problems. Finally, in HMM the user averages the microscopic data over time before transferring the necessary information to the macro solver; in SHMM explicit time averaging cannot be used, but the data is implicitly averaged over time, and the statistical error is comparable to that in HMM at equal cost [212].

5.4 Internal-flow Multiscale Method (IMM)

The multiscale problems that this thesis addresses, i.e. flows in high-aspect-ratio channel geometries, are neither *Type A* nor *Type B* problems. In these high-aspect-ratio geometries, the near-wall region is comparable to the whole simulation domain as the channel diameter is of $\mathcal{O}(1)$ nm. As a consequence, the use of DDM would be as expensive as trying to solve the whole problem with the micro solver exclusively. Likewise, in a HMM approach the micro solver regions would overlap each other, incurring a severe computational cost even higher than using a DDM approach. A new multiscale method is needed for this type of problems, which can be called *Type C* problems.

In Micro/Nano Electro Mechanical Systems (MEMS/NEMS), channel/tube components, if present, ordinarily are much longer in the streamwise direction than the cross section diameter. In addition, the fluid properties in the streamwise direction are

either uniform or only vary gradually. Consequently, it is justifiable to model these long channels by shorter periodic MD simulations, as first shown by Borg *et al.* [60]. Processes occurring on the small scale transverse to the flow direction are only loosely coupled with the macroscopic processes occurring in the streamwise direction. In such conditions, spatial scale separation exists and a macroscopic description of the flow on the larger scale can be adopted (e.g. the continuum conservation laws) coupled to MD simulations covering far smaller, and unconnected, regions in space. This Internal-flow Multiscale Method (IMM) achieves significant computational savings by applying this multiscale approach to any long channel components.

The method that is presented here and applied to a problem in chapter 6 is able to deal with this uni-directional scale separation class of problems. Although the IMM is closely related to the HMM, it has two major differences. First, in previous studies and applications of HMM, velocity fields or strain-rates have been imposed as constraints on the micro solver, and then measurements of stress are obtained from the micro solver and transferred back to the macro solver. In contrast, the IMM uses the more convenient and accurate approach of prescribing a stress or momentum flux into the micro solver and measuring the streaming velocity of mass flux from the micro model in return. Secondly, IMM avoids non-periodic boundary conditions or complex deformations on the MD domain; instead, simple periodic boundary conditions can be used in all the micro domains. This significantly increases the efficiency, along with the simplicity, of the method.

Figure 5.5 shows a schematic of the kind of multiscale fluidic networks that can be addressed with the IMM approach. In this network the inlet and outlet reservoirs are set at different pressures P_{in} and P_{out}, respectively. The pressure drop $\Delta P = P_{in} - P_{out}$ develops a flow through the long channel and the contraction at its midpoint. This contraction could be substituted by kinks, bends, mixers, pumping chambers, bifurcation channel connectors or a local defect in the material, for instance. For simplicity all such elements will be termed *junctions* hereafter. The other class of components, such as straight pipes, tubes and channels will be termed *channels*.

The network in Fig. 5.5b is decomposed according to the categorisation of *junctions* and *channels*. Note that each junction includes also an extra channel section long

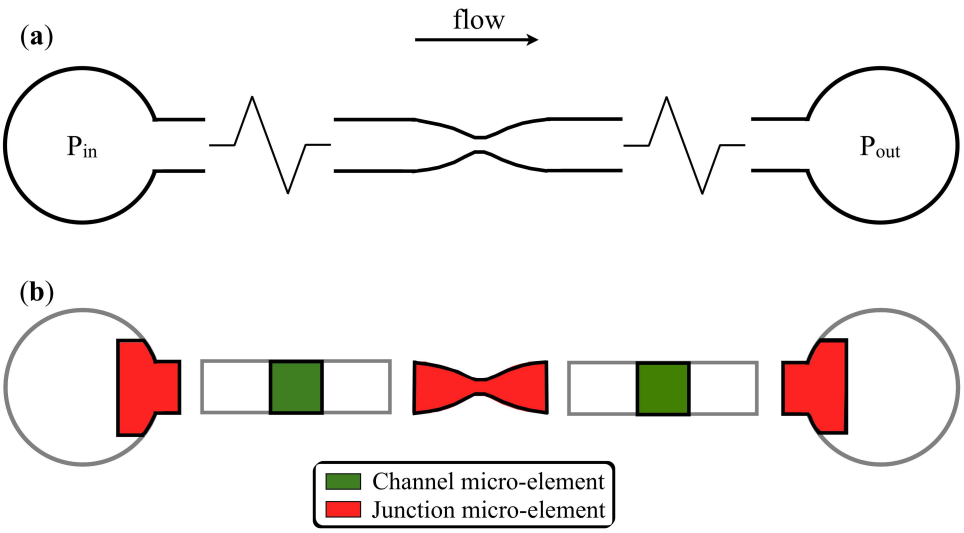

Figure 5.5: (a) Schematic of a simple nanofluidic serial network connecting two reservoirs. (b) The multiscale decomposition into separate micro-elements, where only the regions in green and red are simulated with the micro solver.

enough so that local entrance/exit effects are contained within the junction simulation. As in the previous multiscale methods presented in this chapter, the IMM models each junction and channel using MD as the micro solver (termed *micro-elements*). Each micro-element spans the entire cross section of the channel and includes a molecular description of both the solid bounding wall and the contained fluid. These micro-elements aim to provide an accurate prediction of the local mass flux and pressure loss caused by wall-liquid and liquid-liquid interactions.

As in the HMM approach, there is no direct communication between the micro-scopic simulations, only the constraints of the macroscopic solver provide an indirect communication. In addition, no constitutive relation or slip boundary conditions are required in the continuum definition as these are provided by the micro-elements. All the applications described later in this thesis are under the same flow assumptions as in the original presentation of the IMM by Borg *et al.* [58], i.e. that the flows are low speed, low Reynolds number, isothermal, incompressible and steady-state.

The macro to micro solver constraint consists of applying pressure drops across the micro-elements. The missing data required by the macro solver are measurements of mass fluxes through the disconnected micro-elements. In order to conserve overall mass flux, the applied pressure drops must subsequently be re-adjusted. Any computational

saving that the IMM can offer is achieved only from replacing long scale-separated channel sections with shorter, but hydrodynamically equivalent, periodic channels. The junction micro-elements provide no computational advantage, except that smaller MD simulations in the IMM approach can converge far quicker to steady state than they would in a large MD system.

At the heart of this multiscale method lies the conservation of mass. It is required that the mass flow rate through each micro-element must be identical for a steady state flow in the serial-type of network shown in Fig. 5.5, i.e.

$$\dot{\mathrm{m}}_{\mathrm{i}} = \frac{1}{\Pi} \sum_{j=1}^{\Pi} \dot{\mathrm{m}}_{\mathrm{j}} = \bar{\dot{\mathrm{m}}}, \tag{5.1}$$

where $\dot{\mathrm{m}}_{\mathrm{i}}$ denotes the mass flow rate measured in the i^{th} of Π micro-elements. The mean mass flow rate $\bar{\dot{\mathrm{m}}}$ along all of the elements can be considered as the principal output of the multiscale simulation. During the first iteration of the IMM, the mass flow rates in every micro-element are unequal, but as the following algorithm is applied a solution to Eq. (5.1) is approached.

According to the flow assumptions, a constant density and temperature are specified, while the total pressure difference ΔP between the two reservoirs is determined by the problem. The pressure drop across all the micro-elements can be correlated to the total pressure difference by:

$$\Delta P = \sum_{i=1}^{\Pi} \Delta P_i, \tag{5.2}$$

where ΔP_i is the pressure drop along the i^{th} micro-element.

In order to enforce the above constraints the iterative coupling scheme first proposed by Borg *et al.* [58] is used with a scaling factor f in the first step. At the first iteration $l = 0$, an estimation of the pressure difference along each micro-element is needed: $\Delta P_i = f\mathrm{L_i}\Delta P/\mathrm{L}$, where $\mathrm{L_i}$ is the streamwise length of the i^{th} micro-element, and L is the total length of the system. The relaxation (user defined) factor f is needed as the total pressure drop contains the entrance and exit losses, which will be explicitly included in the junction micro-elements. In addition, the relaxation factor increase the

stability of the method by avoiding over-corrections that may lead to a reversal of the flow direction. This relaxation factor solely affects convergence and does not alter the accuracy of the method or the final result. Then all the micro-element MD simulations are performed with the pressure differences (ΔP_i) calculated above until steady state is reached. Mass flow rate ($\dot{\mathrm{m}}_{\mathrm{i}}^{\mathrm{l}}$) measurements are then taken in all micro-elements.

At the next iteration $l+1$, the applied pressure difference (ΔP_i^{l+1}) at each micro-element is corrected. If it is assumed that, under the specified conditions, $\dot{\mathrm{m}}_{\mathrm{i}}$ varies monotonically with ΔP_i, the missing equation that will lead to a common mass flow rate in each of the micro-elements is provided by:

$$\Delta P_i^{l+1} = \Delta P_i^l + \psi_i \left(\bar{\dot{\mathrm{m}}}^{\mathrm{l+1}} - \dot{\mathrm{m}}_{\mathrm{i}}^{\mathrm{l}} \right), \tag{5.3}$$

where ψ_i is a relaxation coefficient for each micro-element. Relaxation is a technique used for improving stability or efficiency of a computation, particularly in solving steady-state problems. It works by limiting the amount which a variable changes from one iteration to the next, either by modifying the solution matrix and source prior to solving for a field, or by modifying the field directly. A relaxation factor between $0 \leq \psi \leq 1$ specifies the amount of under-relaxation, ranging from none at all for $\psi = 1$ and increasing in strength as $\psi \to 0$. The limiting case where $\psi = 0$ represents a solution which does not change at all with successive iterations. Under-relaxation is often employed to avoid divergence in the iterative solution of strongly nonlinear equations. On the other hand, for $\psi > 1$ the effect is over-relaxation that accelerates the variable changes. Here the coefficient ψ_i can be calculated based on the approximation of a linear relationship between ΔP_i and $\dot{\mathrm{m}}_{\mathrm{i}}$, viz.

$$\psi_i = \frac{\Delta P_i^l}{\dot{\mathrm{m}}_{\mathrm{i}}^{\mathrm{l}}}. \tag{5.4}$$

This approximation does not affect the accuracy of the converged solution, but solely the convergence speed. Then Eq. (5.3) can be reduced to a simpler form:

$$\Delta P_i^{l+1} = \Delta P_i^l \frac{\bar{\dot{\mathrm{m}}}^{\mathrm{l+1}}}{\dot{\mathrm{m}}_{\mathrm{i}}^{\mathrm{l}}}. \tag{5.5}$$

Before updating the pressure difference applied to each micro-element, a more accurate estimate of the mean mass flow rate $\bar{\dot{\mathrm{m}}}^{\mathrm{l}+1}$ is needed. This is accessible through the combination of Eqs. (5.2) and (5.5):

$$\bar{\dot{\mathrm{m}}}^{\mathrm{l}+1} = \frac{\Delta P}{\sum_{i=1}^{\Pi} \left(\Delta P_i^l / \dot{\mathrm{m}}_{\mathrm{i}}^{\mathrm{l}} \right)}. \tag{5.6}$$

The above steps are repeated until the following convergence criterion is met:

$$\zeta_i^{l+1} < \zeta^{tol}, \text{ with } \zeta_i^{l+1} = \frac{\| \bar{\dot{\mathrm{m}}}^{\mathrm{l}+1} - \dot{\mathrm{m}}_{\mathrm{i}}^{\mathrm{l}} \|}{\bar{\dot{\mathrm{m}}}^{\mathrm{l}+1}}, \tag{5.7}$$

where ζ^{tol} is a predetermined tolerance used for all micro-elements.

5.5 Summary

This chapter presented a review of some commonly used hybrid multiscale approaches, including the DDM in section 5.2 and the HMM in section 5.3. Although these methods are not suitable to simulate the problems addressed in this thesis, they constitute the foundation of a most recent mutiscale hybrid approach, the IMM. A detailed description of the IMM was given in section 5.4. This is the hybrid multiscale approach of choice, in that it can accurately and efficiently simulate the *Type C* problems that this thesis focusses on. In chapter 6, validation of the accuracy and efficiency of the IMM will be presented in comparison to results of full MD simulations. An attempt to produce results for very long nanotubes of engineering interest will then be made.

Chapter 6

Hybrid simulations of nanotube membranes

Χρόνου φείδου.

- Χείλων ο Λακεδαιμόνιος (6ος αιώνας π.Χ.)

Do not waste your time.

- Chilon of Sparta (6th century B.C.)

Chapter 3 presented results from MD simulations of water flow in carbon nanotubes, detailing the wall-induced biaxial ordering of water close to the CNT walls and how electric fields can promote or hinder the flow rate. Chapter 4 showed how different nanotube materials affect the flow rate, and a first attempt was made to predict the flow enhancement through nanotubes of any length. This chapter attempts to connect the physics and flow dynamics observed at the nanoscale with larger, macroscopic problems of direct engineering interest. In this application area, length scales in at least one dimension are up to 10^6 orders of magnitude greater than those investigated in previous chapters.

In multiscale problems where the diameter of the channel is at the nanoscale but the overall length of the device is up to a few millimeters, special hybrid methods such as those presented in Chapter 5 should be used. Otherwise a pure MD simulation of a 1 mm thick CNT membrane (with a system geometry similar to those presented in Chapters 3 and 4) would require more than a thousand years of simulation time using

current state-of-the-art MD codes on high performance computational facilities. A conventional macroscopic approach, such as the Navier-Stokes-Fourier (NSF) equations, is also inadequate for these types of problems. While the NSF equations have been shown to still be valid and accurate for Newtonian flows at the nanoscale, large inaccuracies arise for flows with unknown constitutive relations (non-Netwonian flows), flows dominated by surface effects, or flows that exhibit thermodynamic non-equilibrium due to high gradient processes in the bulk fluid.

Of the hybrid methods presented in Chapter 5, the IMM is the most appropriate as it was specifically developed for multiscale internal-flow problems with high aspect ratio in the streamwise direction, like the ones studied in this thesis. A number of recent publications have presented and validated this method for both compressible and incompressible flows of an atomistic Lennard-Jones fluid in complex geometries [58, 60, 213].

In this chapter the IMM will be applied to the water-CNT membrane systems. Initial simulations of membranes with a thickness up to 150 nm will serve for validation purposes. The main assumption in the IMM is the linear dependence of the mass flow rate on the pressure difference. The accuracy of the method is not affected even if this assumption does not perfectly represent the exact relation between pressure and flow rate, but the convergence of the method can be highly disturbed. This assumption sets the evolution of the relaxation coefficient ψ through Eqs. (5.3) and (5.4). This linear dependence assumption, and possible ways to improve the relaxation coefficient, will be investigated in section 6.2.

Simulations of long systems from 1 μm up to 1 mm will be presented in section 6.3. These longer systems are of strong engineering interest as shorter CNTs are not only harder to produce but the membrane will also be less rigid, making it unable to handle the required pressure differences. In section 6.3, one of the hybrid simulations will be directly compared with an experimental application, highlighting possible sources of errors and inaccuracies in both the experimental and computational approaches. This comparison may not give clear and definitive answers, as experimental results are also affected by assumptions and errors during the measurement procedure. These are often great discrepancies in the experimental results for similar membranes [18, 160, 186, 214,

215]. The linear dependence of the flow enhancement with the length of the CNT, that was initially addressed in Chapter 4, will be discussed further alongside the results from the hybrid simulations.

6.1 Simulation setup

Every hybrid simulation presented in this chapter consists of 2 micro-elements: a junction and a channel, as defined in Chapter 5. For convenience, the two water reservoirs are combined in one junction micro-element , instead of two separate ones. This enables the use of periodic boundary conditions to be used in all directions. The reservoirs are separated by a CNT membrane. Its walls are graphene sheets with dimension 10.5×10.2 nm, while the connecting tube is a 12.6 nm long single-wall (15,15) CNT. The chirality of the CNT defines its diameter according to Eq. (3.9) and for all the presented hybrid simulations $D = 2.034$ nm unless a different value is specifically defined in a case. A characteristic snapshot of the simulated junction micro-element is given in Fig. 6.1.

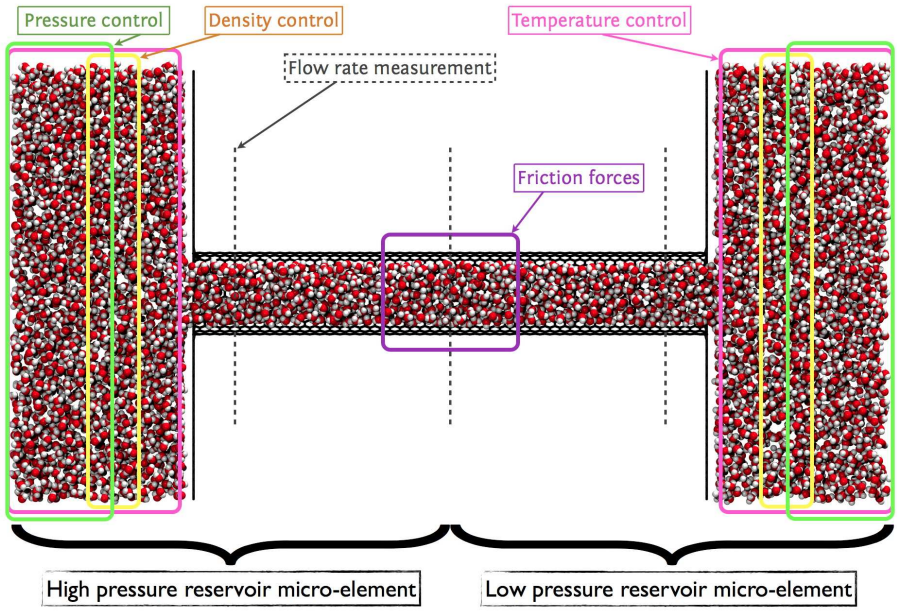

Figure 6.1: Snapshot of the simulated junction micro-element, which is a combination of the two water reservoirs. Black dashed lines show the mass flow rate measurement planes. Pink, yellow and green boxes highlight the temperature, density and pressure control regions, respectively. The purple box shows the region where the Gaussian forcing method emulates the pressure drop from the missing length of the CNT. Positive water flow is considered from the left (high pressure reservoir) to the right (low pressure reservoir). Periodic boundary conditions in all directions are considered.

Inside the reservoirs, temperature and pressure are controlled during the whole simulation. A Berendsen thermostat is used to control the temperature, rescaling only the velocity components of each molecule that are normal to the flow. The target pressure difference of 200 MPa is created using the Gaussian forcing method [58], as described in Chapter 3. An additional forcing region in the middle of the CNT is necessary in order to replicate the frictional forces from the missing length of the CNT. A FADE density controller [59] is also applied during the first 0.5 ns of the equilibration run. Figure 6.1 highlights the control and forcing regions as well as the flow rate measuring planes. Equilibration runs of at least 2 ns were performed before the production runs in order to create a fully developed flow inside the CNT. Production runs of at least another 2 ns followed and until the termination criterion have been met. This criterion is based on the standard deviation (STD) of the mass flow rate measurement: when this was $< 5\%$ the simulation could be terminated.

Figure 6.2 shows a snapshot of the simple channel micro-element. In this case, temperature and density are controlled over the length of this CNT but only during the equilibration time. Frictional heating during production runs is minimal (< 5 K) due to the fact that the sampling time is quite short and pressure differences inside the channel micro-element are very small, compared to the overall pressure difference of the full system. The Gaussian forcing method is applied in the highlighted regions during the simulation in order to create the required pressure drop at each iteration. This pressure difference, along with the one at the middle of the junction micro-element, are calculated at every iteration of the hybrid algorithm according to Eq. (5.5).

The number of water molecules in the channel micro-element is defined according to the density measured at the middle of the junction micro-element in the same iteration. This procedure increases the overall simulation time of the hybrid method, (as will be shown and explained in section 6.2.2), but it also increases the accuracy of the results. The mass flow rate is measured in a flow plane at the middle of the CNT, as well as with an additional measurement tool that takes into account all the water molecules' velocities in the CNT. The two approaches are in agreement, with the measured results having a variation of $< 1\%$. Simulation times, boundary conditions and termination criteria are the same as for the junction micro-element.

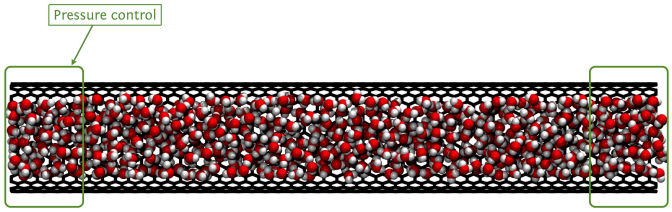

Figure 6.2: Snapshot of the simulated channel micro-element. Due to the periodic boundary conditions the length of the channel can be considered as infinite. The Gaussian forcing method applied in the highlighted green regions reproduce the required pressure drop, as this would be in the equivalent central part of the pure MD simulation of the full membrane.

The pressure drop at the middle of the junction micro-element in reality replicates the frictional losses due to the missing length of the CNT. In a similar way, the pressure drop applied in the channel micro-element is scaled down compared to the one that should be applied in the full channel length. This way the same pressure gradient is achieved inside the channel while significant computational savings are achieved as only a fraction of the full membrane thickness is simulated. This fraction is constant independent of the full scale size of the original membrane under investigation, leading to increased computational savings as the membrane size is increased.

Pure MD simulations are also performed for the validation of the hybrid IMM for the specific problem studied here. The setup of these validation MD simulations is the same as for the junction micro-elements. The only differences are that the length of the CNT can vary from 50 to 150 nm, and there is no forcing region in the middle of the CNT.

6.2 Hybrid code accuracy and performance benchmarking

The hybrid IMM has already been validated and tested for a simple Lennard-Jones atomistic fluid and various geometries, from a converging-diverging channel [60] to a membrane-like geometry [58], and lately in a network of nano-channels [213]. These

studies showed the high accuracy of the method when compared to pure MD simulations (error $< 5\%$), while the convergence of the method was exceptional (fewer than five iterations are needed to fulfill the convergence criterion). Non-linear pressure and density profiles were observed in some of these investigations [60, 213] due to the geometry of the channel, the nature of the fluid, and the very high pressure difference applied. On one occasion, the inclusion of additional channel micro-elements further improved the accuracy of the results [60], while in another an empirical equation of state was used in order to include fluid compressibility [213].

This chapter presents validation simulations of the IMM for the flow of a more complex and realistic fluid (i.e. water) in CNT membranes. Pure MD simulations of the full length CNT membranes will be considered as the accurate, reference cases. The mass flow rate measurement is the main comparison property, but additional measurements and comparisons of pressure, temperature, density and velocity profiles will also be presented.

6.2.1 IMM validation with pure MD

The validation simulations consist of three systems with varying CNT length (or thickness of membrane), from 50 nm up to 150 nm long. These lengths are chosen so that pure MD simulations can be performed in reasonable time. Figure 6.3a shows how accurately the mass flow rate can be predicted by the IMM in this type of systems. The initial linear assumption of the pressure drop along the CNT seems to be very efficient for these systems as the predicted mass flow rate after 1 iteration differs less than 5% from the pure MD simulation. The error-bars show 1.96 standard deviations (STDs) of the sampled mass flow rate. Long production runs of at least 2 ns ensure that the mass flow rate and all the other properties have been measured for over 10^6 samples, leading to small STDs of the samples. The stability of the method can be also observed and although the measured mass flow rate can deviate at one iteration, it converges to a more accurate value at the next iteration.

The development of the axial profile of pressure from the high pressure reservoir — to the middle of the CNT — to the low pressure reservoir is observed in Fig. 6.3b . The hybrid IMM result is in excellent agreement with the pure (full) MD simulation.

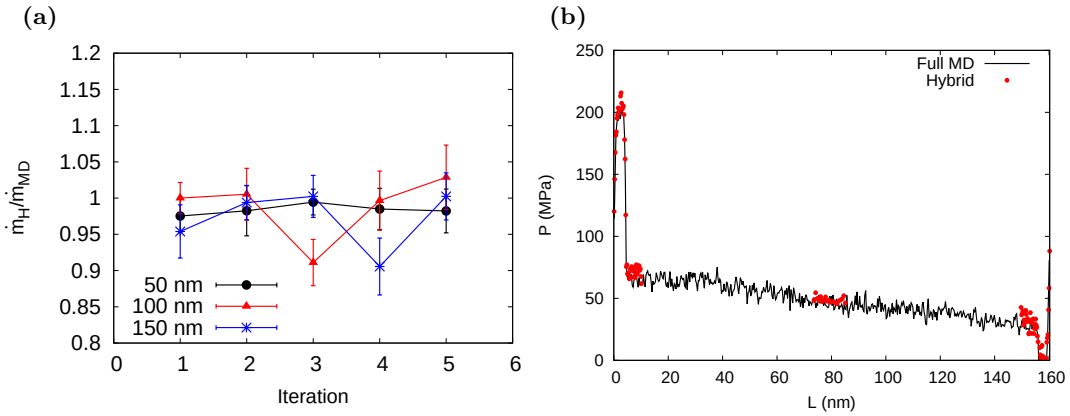

Figure 6.3: **a**, Mass flow rate measurements $\dot{m}_H$ from the IMM simulation of three different lengths of CNT, normalised by the equivalent measurements from the reference pure MD simulations $\dot{m}_{MD}$. Errorbars show 1.96 STDs of the samples (95% confidence interval). **b**, Axial profile of pressure along the 150 nm CNT membrane. Hybrid IMM results are the combination of the values measured in the junction and channel micro-elements.

In this validation case the pressure profile shows a linear drop along the CNT, so no compressibility effects are expected. While this figure supports the initial assumption of linear pressure drop along the CNT, the significant entrance losses should be noted as they are not taken into account explicitly by a simple linear assumption of the pressure drop along the whole system (from reservoir to CNT to reservoir). This was the reason a relaxation factor f was introduced in Chapter 5 for the initial calculation of the pressure difference along each micro-element.

Figure 6.4a shows the convergence of the IMM for the three validation cases that is calculated according to Eq. (5.7). The convergence limit chosen was $\zeta^{tol} = 0.1$ which is larger than that chosen in previous implementations of the IMM. The relaxation factor ψ, which can vary for each micro-element as well as from iteration to iteration, seems to be responsible for the non-monotonic convergence. This relaxation factor is calculated according to Eq. (5.4) and can switch between under- and over-relaxation. The accuracy of the method is not affected, as shown in Fig. 6.3, however convergence seems to significantly oscillate. Further study of the relaxation factor and its impact on convergence is needed, while the effect of a constant under- or over-relaxation factor must be also considered. A more sophisticated expression for the relaxation factor ψ, that includes more information regarding the simulated system, such as the ratio of the micro-element length to the full length of the system, could be a future development

of the method.

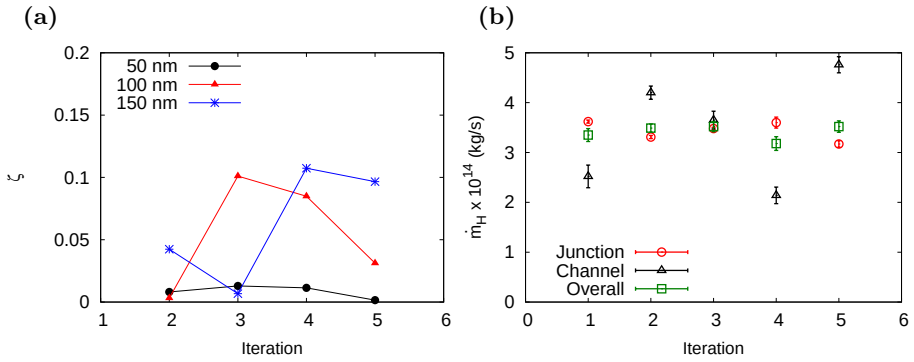

Figure 6.4: **a**, Convergence of the hybrid IMM simulations of the three validation cases; the convergence value ζ is calculated according to Eq. (5.7). **b**, Mass flow rate measurements $\dot{m}_H$ from the IMM simulation of the 150 nm long CNT membrane. The figure includes the values from the junction and channel micro-elements, as well as the overall mass flow rate calculated according to Eq. (5.6). Errorbars show 1.96 STDs of the samples (95% confidence interval).

The evolution of the mass flow rate measurements at each iteration (and each micro-element) is shown in Fig. 6.4b for the case with the 150 nm long CNT. The errorbars are again 1.96 STDs of the sample and the overall mass flow rate and STD are those previously used in Fig. 6.3a. In these validation cases, entrance and exit effects dominate the flow, while frictional losses become more significant for longer systems ($>$ 1 μm). Because of this, the junction micro-element contributes more to the final overall flow rate. In addition, the oscillation in the measurements from the channel micro-element does not alter the overall measurement significantly. Both these observations from Fig. 6.4b can be understood by examining Eq. (5.6), where at a converged stage the mass flow rates can be (almost) equal to each other while pressure drops can differ significantly.

Figures. 6.3a and 6.4 show that two iterations are enough for systems with a CNT length up to 100 nm, while for longer systems up to 150 nm a third iteration is necessary. The convergence and accuracy analysis above leads to an additional convergence criteria. This is to impose a minimum number of iterations, i.e. a hybrid simulation of a membrane with a CNT length of 300 nm should perform at least three iterations before the convergence tolerance ζ^{tol} is also considered.

In addition to the mass flow rate comparison between the pure MD and the IMM, Fig. 6.5 presents radial and axial density profiles inside the CNT and along the sim-

ulated system, respectively. These plots show excellent agreement between the pure MD and the hybrid IMM results and capture the pronounced non-continuum effects, i.e. molecular layering in the radial density profiles. In every simulated case the IMM channel micro-element reproduces the same density values and gradient as those measured in the central part of the pure MD simulation. This can be attributed to the correct water density initialisation of each channel micro-element, as described in section 6.1.

Further validation of the multiscale method was made by plotting cross-channel and streamwise velocity and temperature profiles in Figs. 6.6 and 6.7, respectively. Very good quantitative agreement with the pure MD reference results is obtained, which includes non-equilibrium effects like the high slip in the velocity profiles. The velocity profile inside the CNT is plug-like and difficult to predict with conventional macroscopic equations as the amount of slip and other phenomena (e.g. density rise and viscosity reduction close to the wall) are unknown parameters. However, the hybrid multiscale approach manages to reproduce the velocity profiles very accurately because it includes molecular-level information from the individual micro-element simulations.

The temperature profiles in Fig. 6.7 show that both the reference MD simulations and the hybrid IMM are performed under the same conditions. The radial temperature profile shows excellent agreement between the two simulation approaches. It should be noted that the temperature is not controlled inside the channel micro-element during the sampling period. Frictional heating is minimal, as expected, due to the small pressure gradients inside the CNT. In the reference MD simulations and the junction micro-elements, temperature is controlled only inside the reservoirs. This explains the larger oscillations along the full MD CNT, especially for the longer case.

All the above measurements and comparisons between the reference pure MD results and the hybrid IMM results show the ability of the multiscale method to reproduce all the important flow phenomena and capture the values of interest with high accuracy. Despite the more complex nature of the fluid used here (water) compared to that in previous studies (a LJ fluid) the IMM shows the same advantages in tackling these kinds of multiscale problems. The oscillations observed in the convergence of the method are attributed to the variable nature of the relaxation factor ψ used here and should be further investigated in the future. However, this does not affect the accuracy of

the method but solely the convergence speed and the definition of proper termination criteria for the iterative IMM.

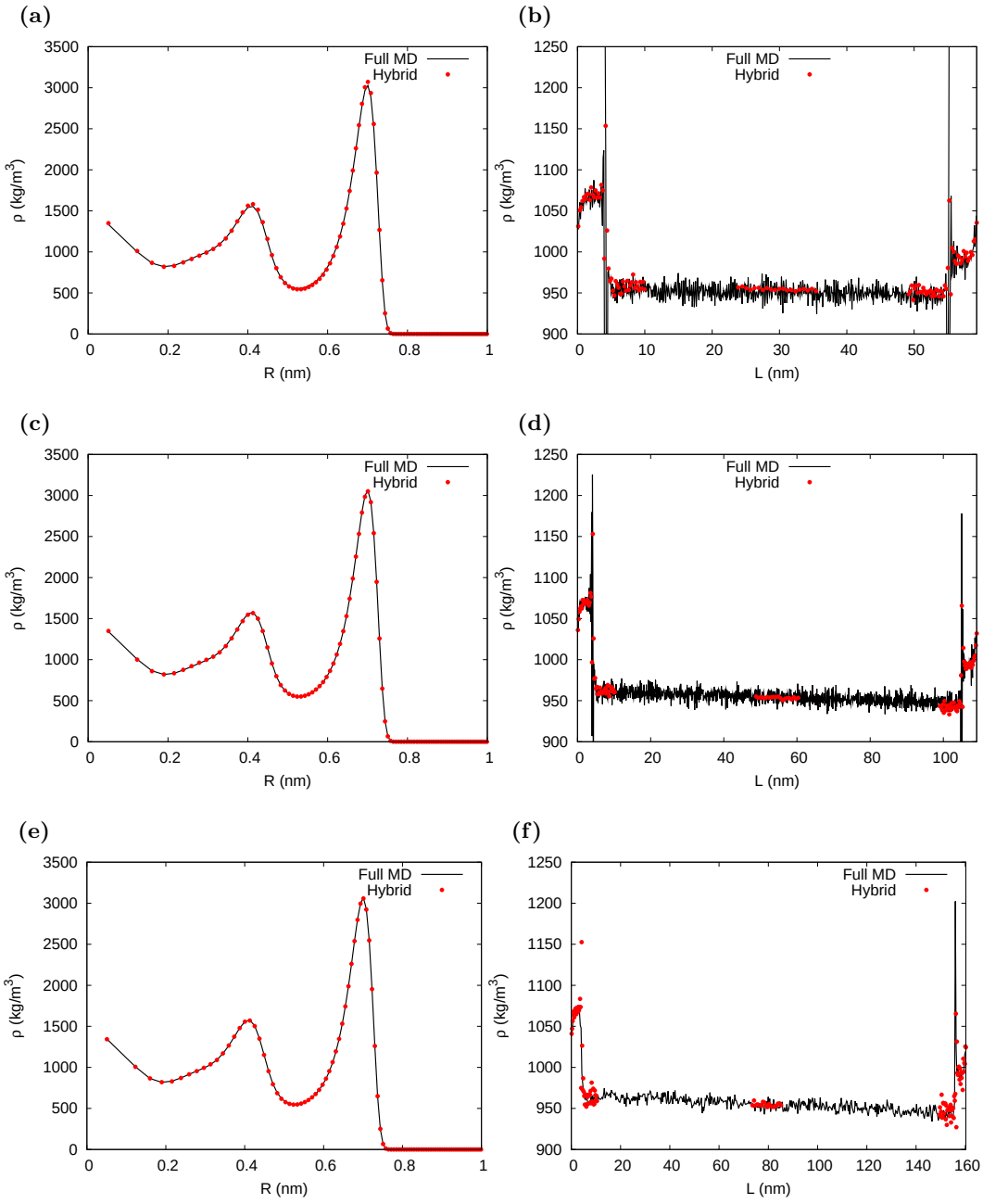

Figure 6.5: **a, c, e,** Radial density profiles across the CNT for the 50, 100 and 150 nm thick membranes, respectively. The density was measured and averaged over the length of the channel micro-element in the case of the IMM simulations. **b, d, f,** Axial density profiles along the simulated systems. The IMM points include measurements from both the junction and the channel micro-elements.

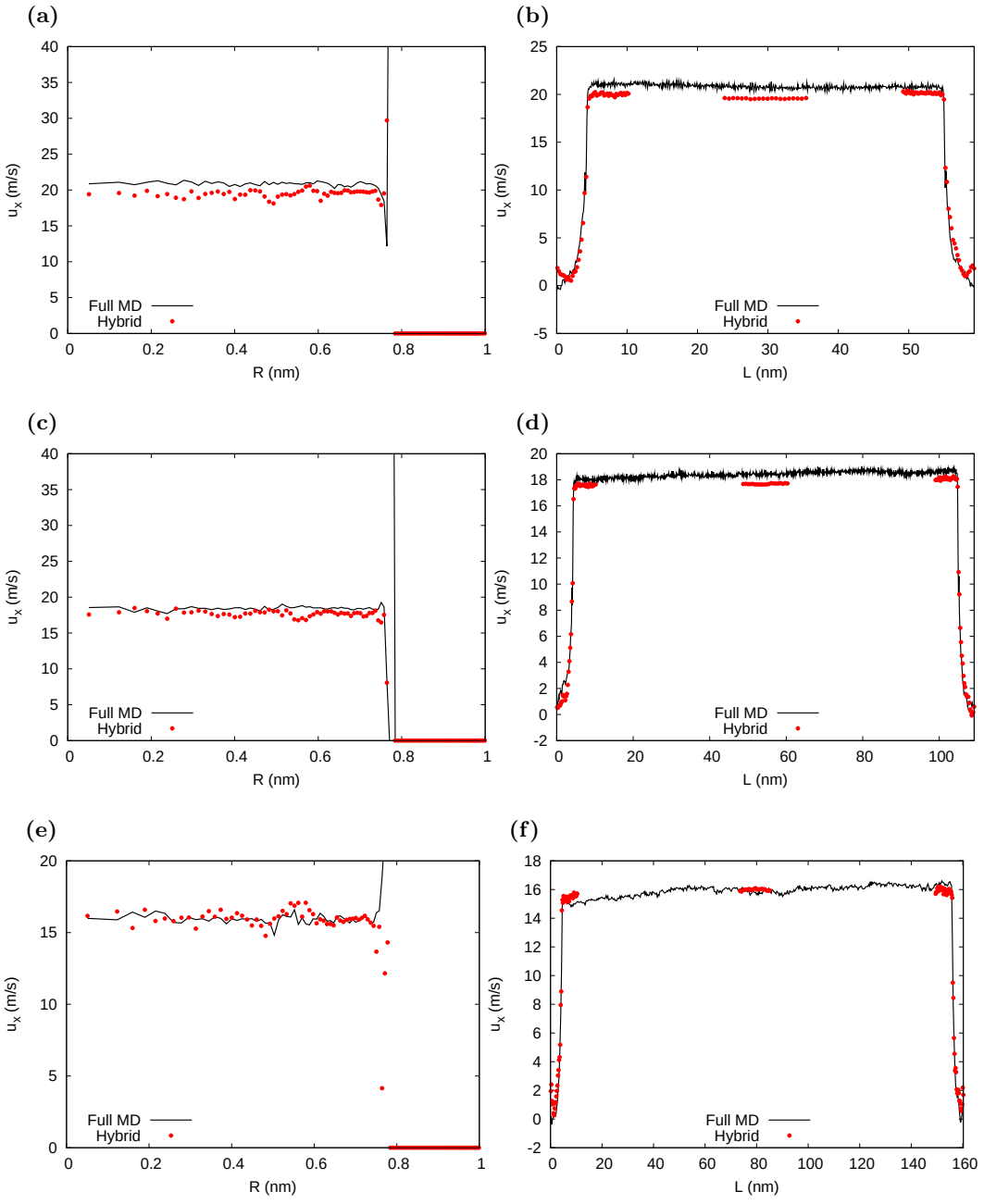

Figure 6.6: **a, c, e,** Radial velocity profiles across the CNT for the 50, 100 and 150 nm thick membranes, respectively. The velocity was measured and averaged over the length of the channel micro-element in the case of the IMM simulations. **b, d, f,** Axial velocity profiles along the simulated systems measured across the CNT diameter. The IMM points include measurements from both the junction and the channel micro-elements.

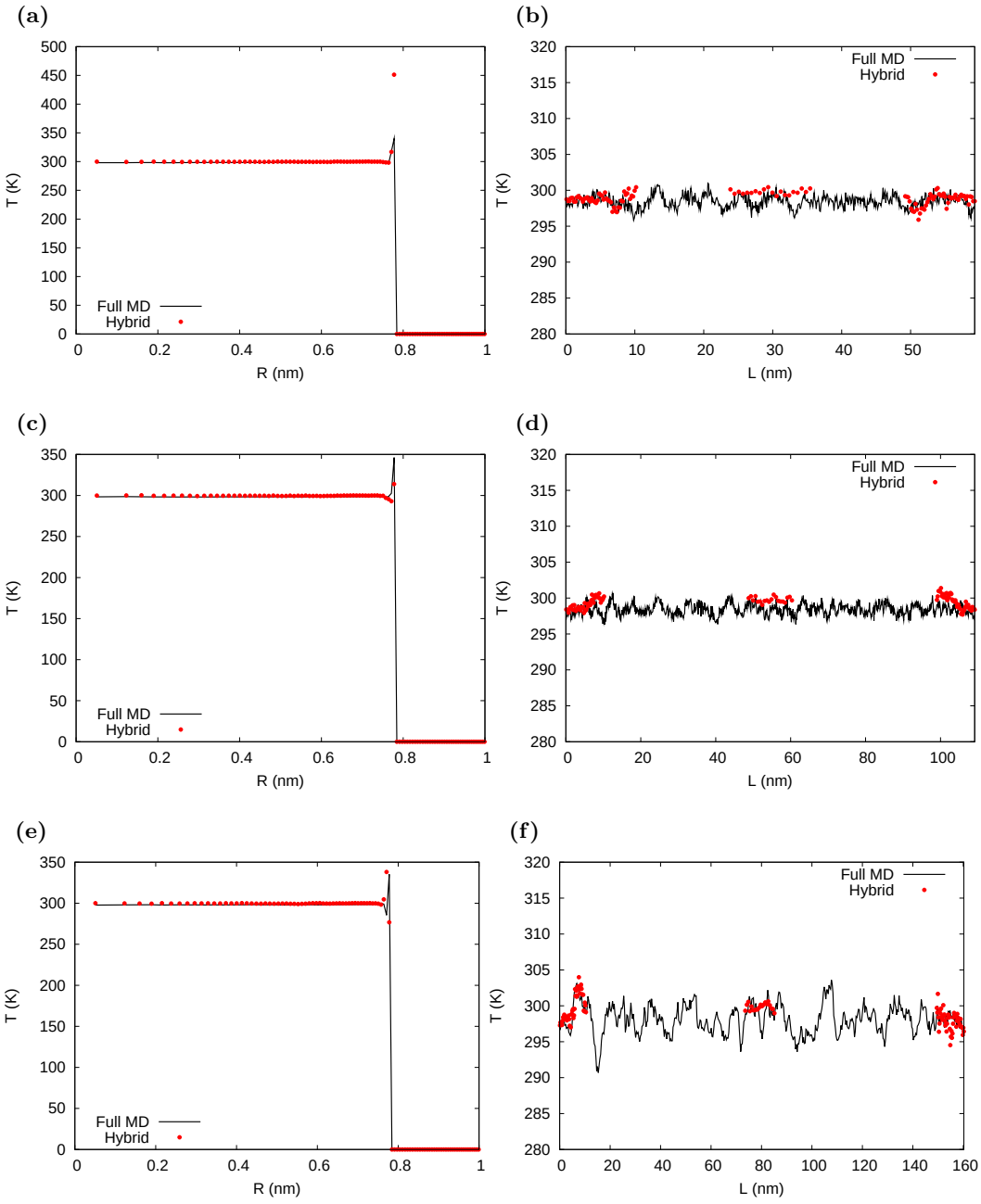

Figure 6.7: **a, c, e,** Radial temperature profiles across the CNT for the 50, 100 and 150 nm thick membranes, respectively. The temperature was measured and averaged over the length of the channel micro-element in the case of the IMM. **b, d, f,** Axial temperature profiles along the simulated systems. The IMM points include measurements from both the junction and the channel micro-elements.

6.2.2 Computational efficiency and performance

This section will briefly present the computational efficiency of the hybrid IMM and the advantages it offers over conventional pure MD simulations. All the comparisons made here are with the GPU version of mdFoam. This version of the code performs all the force calculations on the GPU while the rest of the measurements, controls and time-stepping are performed on the CPU. The hybrid approach utilises the same version of the MD solver, and simulations were performed on identical computational nodes of the high performance computer ARCHIE-WeSt at Strathclyde University. Each node consists of two Intel Xeon X5650 CPUs (12 cores in total), 48 GB of RAM and a NVidia M2075 GPU card. Therefore any computational savings reported here are attributed, solely, to the hybrid implementation, and not to any possible hardware or software differences. The GPU version of mdFoam already offers 7.7 times speed-up when compared to the CPU parallel implementation.

The performance comparison is based on the simulation time needed to reach the final solution using each method (pure MD and IMM), without calculating initialisation and equilibration times. The thickness of the CNT membrane (i.e. CNT length) is used as the size variable. Longer systems not only contain more molecules but also need additional time to reach steady state. In the case of pure MD simulations, the time to solution increases linearly with the CNT length, as Fig. 6.8 shows. For the three validation cases, the simulation time to solution is higher for IMM compared to pure MD simulation. However for the longer systems of 1 and 2 μm, the IMM is more efficient despite the fact that 6 iterations are performed in order to achieve the desired convergence and accuracy. If a fixed density is used for the iterations of the channel micro-elements, then both micro-elements can be simulated in parallel, reducing by almost 50% the computational time (see Fig. 6.8b). This can, however, significantly affect the accuracy, depending on the chosen density value.

For the 2 μm case the total simulation time is 50% of the equivalent pure MD simulation, as Fig. 6.8b shows. For longer cases still, the computational savings will be even greater as the simulated system in the IMM remains the same and only the number of iterations and/or time to reach steady state can increase. From these figures, it is estimated that a CNT membrane with a thickness of 100 μm would require around 8000

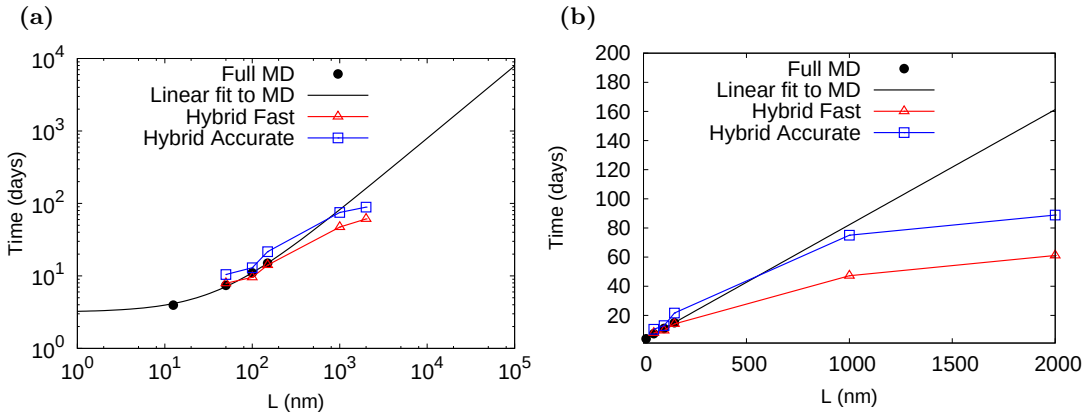

Figure 6.8: a,b, Computational time to solution varying with CNT length in logarithmic and linear scales, respectively. Blue squares show the time needed by the hybrid IMM when the density in the channel micro-element is initialised according to measurements in the junction micro-element at each iteration. Red triangles show the time needed by the hybrid IMM when there is a fixed density in the channel micro-element at every iteration.

days of simulation time using the current state-of-the-art pure MD solver on a GPU. However, the same result can be achieved using IMM in $\sim$ 100 days (see Fig. 6.8a).

An additional advantage of the fixed simulation size in IMM, independent of the problem's actual size, is the required computer memory. The GPU solver utilises only the GPU memory and not the RAM memory of a node; otherwise the communication overhead hinders any computational savings. The current GPU cards in ARCHIE-WeSt have 6 GB of memory, which is enough to simulate around $400,000$ atoms, highlighted in Fig. 6.9 by continuous red line. This limits the size of the pure MD simulations to a membrane with a CNT shorter than 1 μm. A possible solution would be to use GPUs with larger memory, but the best current GPU cards offer a maximum of only 12 GB memory. Another option would be the parallelisation of the GPU solver to enable it to run on multiple GPUs, although its performance would be reduced due to the communication overhead.

From this short performance analysis it can be concluded that the only viable option that can significantly reduce computational time and enable access to problem sizes of engineering interest is a hybrid approach like the IMM.

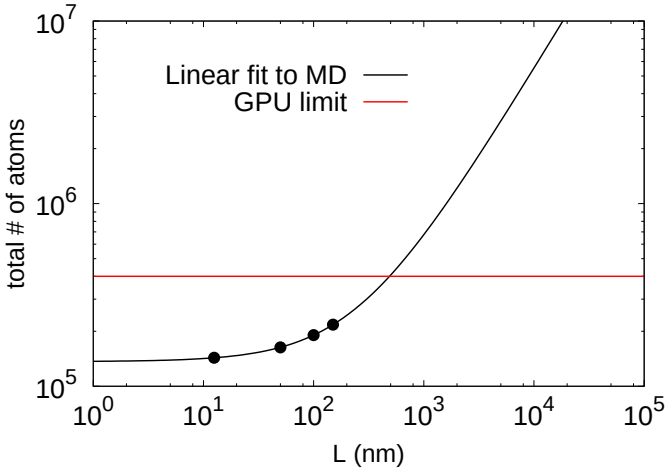

Figure 6.9: Number of simulated atoms varying with the CNT length in the simulated membranes.

6.3 Enhancement predictions and macroscopic equations

This section presents results from IMM simulations that are impossible, or at least extremely computationally demanding, to perform using pure MD. Simulations of CNT membranes with a thickness of 1 μm and 2 μm are performed first. The flow enhancement calculation in these cases, and the results from previous IMM simulations as well as results from Chapter 4, are combined and compared with other computational and experimental studies. A slip and entrance/exit-loss modified Hagen-Poiseuille equation, like the one proposed by Walther *et al.* [18], is also used in an attempt to calculate the flow enhancement (and flow rate) of a CNT membrane of any thickness without the need to perform further IMM or MD simulations.

Figure 6.10a shows how the hybrid IMM leads to a common flow rate through both the micro-elements as the iterations proceed. The variable relaxation factor seems to be very effective as all the values quickly converge after one iteration. However,this is also probably responsible for the oscillatory behaviour of the values around the mean, which has already been observed during the validation simulations of Section 6.2.1. The rapid convergence of the method towards the correct flow conditions (and the measured mass flow rate) is also shown in Fig. 6.10b. Although all channel micro-element simulations started from the same initial conditions at the first iteration, they quickly converge to their final pressure difference value after only one iteration. This figure also confirms that frictional losses inside the CNT membrane increase as the length of the CNT

increases. For the shorter validation cases the frictional losses are at most 25% of the total pressure losses, although this increases to 75% for the 2 μm case.

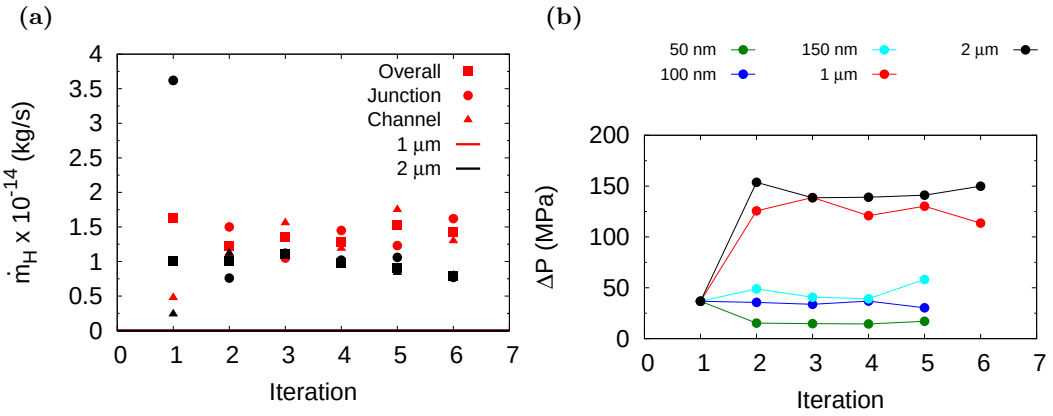

Figure 6.10: **a,** Mass flow rate measurements from the micro-elements and the overall hybrid prediction using Eq. (5.6) at each iteration of IMM. **b,** Pressure difference along the full length of the CNT, excluding the entrance/exit-losses, as calculated from Eq. (5.5).

The main performance measurement of a nanotube membrane is the flow enhancement ($\epsilon = \dot{m}_H/\dot{m}_{HP}$) that it provides above that predicted by the no-slip Hagen-Poiseuille (HP) equation. Enhancement results for nanotube membranes of various materials were presented in Chapter 4. Equation (4.7) attempted to connect this enhancement with the geometrical and material characteristics of the nanotube. Here, the enhancement of CNT membranes of different thicknesses (i.e. CNT lengths) for a constant external pressure difference is shown in Fig. 6.11. The reported values include results from pure MD (for L $<$ 50 nm) and IMM simulations (for L $\geq$ 50 nm). The enhancement initially increases as the CNT length increased, but then plateus significantly for L $>$ 150 nm. This should be expected, unless the flow inside the CNT is completely frictionless.

Figure 6.11 also includes flow enhancement values from other computational and experimental investigations. The diameter of the CNT (2.034 nm) is common in all the selected studies. It should be noted that in the experimental studies this diameter is the dominant one in a membrane that contains CNTs of various diameters. This can significantly affect the reported values, as viscosity and slip length varies with the diameter of the CNT [183]. At the same time, a small variation in the diameter used during the HP flow rate calculation can lead to great difference in the reported

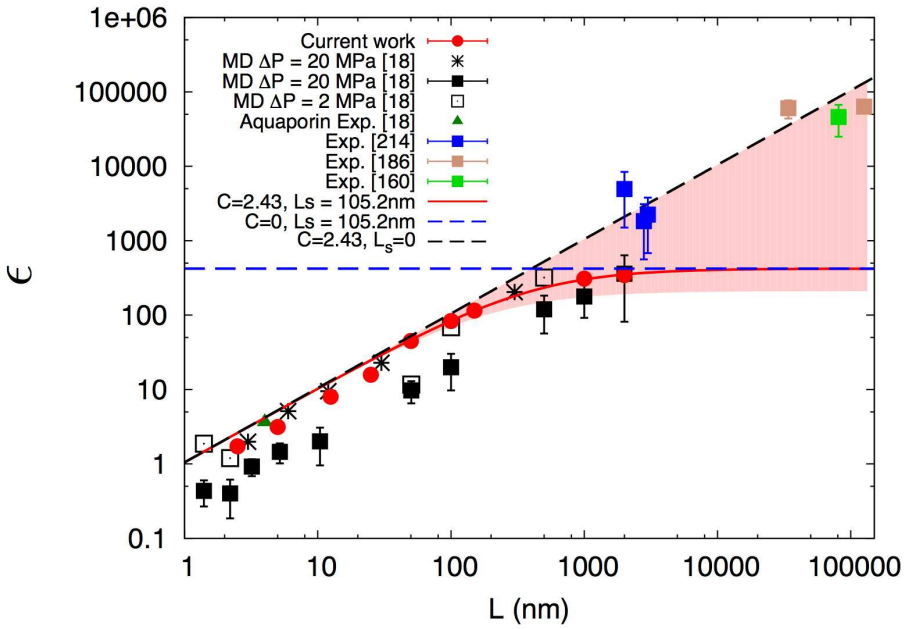

Figure 6.11: Flow rate enhancement ϵ for various thicknesses of CNT membranes L. Comparison of the current work with previous computational and experimental studies. Lines show the enhancement prediction (ϵ_{HPm}) of Eq. (6.3) for the given parameters. The pink shaded area shows the variation of ϵ_{HPm} when L_s varies from 52.75 nm to infinity.

enhancement values. This diameter issue, along with other possible errors during the experimental procedures, can explain the difference between the reported experimental values in Fig. 6.11.

Despite the fact that different MD codes, water models, interaction potentials and external applied pressure differences have been used, the computational results presented in Fig. 6.11 are in line with the values calculated in this thesis. The errorbars of the current results are smaller than the points in Fig. 6.11, while in previous studies the errorbars are quite significant (when given). In addition, an experimental research on a biological nano-channel (Aquaporin) is also included giving excellent agreement. In the study of Walther *et al.* [18], the asymptotic behaviour of the enhancement was predicted using results from a CNT membrane and periodic CNT simulations. Here the same behaviour is seen in membrane simulations taking advantage of the IMM. These results strengthen the hypothesis that the enhancement reaches a plateau after a linear dependence of the enhancement on CNT length — an issue that was raised in Chapter 4. For the CNT membranes studied here the enhancement limit is $\epsilon_{max} \approx 350$, independent of the CNT length.

In the work of Walther *et al.* [18] a modified Hagen-Poiseuille equation was developed in order to predict the flow enhancement for CNT membranes of various thicknesses. Given that the no-sip Hagen-Poiseuille equation is simply

$$\Delta P = \frac{8\mu \mathrm{L}\dot{Q}_{HP}}{\pi R^4}, \tag{6.1}$$

the modified equation incorporating slip and entrance/exit losses as presented in Ref. [18] takes the form [216, 217]:

$$\Delta P = \frac{\mu C\dot{Q}_{HPm}}{R^3} + \frac{8\mu \mathrm{L}\dot{Q}_{HPm}}{\pi\left(R^4 + 4R^3L_s\right)}, \tag{6.2}$$

where the coefficient C represents the sum of both fluid entrance and exit losses, L_s is the slip length, and $\dot{Q}_{HPm}$ is the volumetric flow rate calculated by this equation. From Eqs. (6.1) and (6.2) it can be calculated the modified flow enhancement factor,

$$\epsilon_{HPm} = \frac{8\mathrm{L}\left(R + 4L_s\right)}{8\mathrm{L}R + C\pi R^2 + C\pi R4L_s}. \tag{6.3}$$

This flow enhancement depends on the geometrical characteristics of the CNT membrane, including the length L and radius R of the CNT. It also depends on two parameters, the slip length L_s and the entrance/exit losses coefficient C. If both these parameters are zero then the no-slip Hagen-Poiseuille predictions are reproduced. Using Helmholtz's minimum-energy theorem, Weissberg showed that $C < 3.47$ for $\mathrm{L}/R \to \infty$ [216]. Incorporating in Eq. (6.3) the values of enhancement calculated by the present MD and IMM simulations results in the continuous red line in Fig. 6.11, with optimum fitting parameters $C = 2.43$ and $L_s = 105.2$ nm. The black dashed line in this figure indicate the behaviour of a membrane if the nanotubes were frictionless, while the dashed blue line is for a membrane without entrance or exit losses. The pink shaded area shows the effect of a varying slip length: from half the optimum fit of the slip length up to infinity (frictionless). For membranes with a thickness less than 150 nm the enhancement value is almost independent of the frictional properties of the nanotube (i.e. slip length).

This analysis shows that the flow enhancement, and as a result the flow rate of

water through CNT membranes of any thickness, can be estimated using Eq. (6.3) provided the parameters C and L_s are known. The value of C can be calculated by performing MD simulations of thin membrane cases, while L_s can be obtained from simulations of simple periodic CNT cases. Alternatively, Eq. (4.7) could be modified in order to include the entrance and exit losses. In that case, L_s and C may not be unknown pararameters but they could be calculated based on the geometrical and material properties of the nanotube. Beside the predictive capabilities that Eq. (6.3) offers, it also highlights the critical membrane thickness over which frictional losses dominate the flow.

Direct comparison with experimental results can be troublesome, as Fig. 6.11 shows, due to diameter issue previously analysed and other possible experimental errors. Recent experimental work by Qin *et al.* [215] managed to reduce a source of errors in CNT membrane experiments by performing flow rate measurements of water through a single CNT. One of these experimental cases is replicated here in an attempt to evaluate the computational efficiency of the IMM. The diameter of the chosen CNT in Ref. [215] is $D = 1.59$ nm while its length is L = 1 mm, which means a pure MD simulation would be impossible. Characteristic snapshots onto the CNT in the membrane are given in Fig. 6.12, and show the unique ordered ring formation (see Fig. 6.12b) of water molecules within the CNT. A continuum macroscopic description of water flow through such a narrow CNT could not be used in these circumstances. Basic water properties (e.g. viscosity, density, hydrogen bonding, etc.) are highly altered due to the confinement.

The same methodology as for the previous IMM simulations is applied, with the only differences being the reduced diameter and the external pressure difference, which is reduced to $\Delta P = 100$ MPa. The enhancement values reported by Qin *et al.* [215] are also calculated under some assumptions. The first one is that two van der Waals diameters of carbon (or, equivalently, twice the thickness of the CNT wall) is subtracted from the overall CNT diameter, i.e. $D_r = 1.59 - 0.33 = 1.33$ nm. The second assumption is that the viscosity of bulk water (1 mPa s) is used in all calculations, although it is known that the water viscosity inside such a narrow CNT differs significantly [123, 183]. The bulk water density ($\rho = 997.5$ kg/m^3) is also used in any transformations from

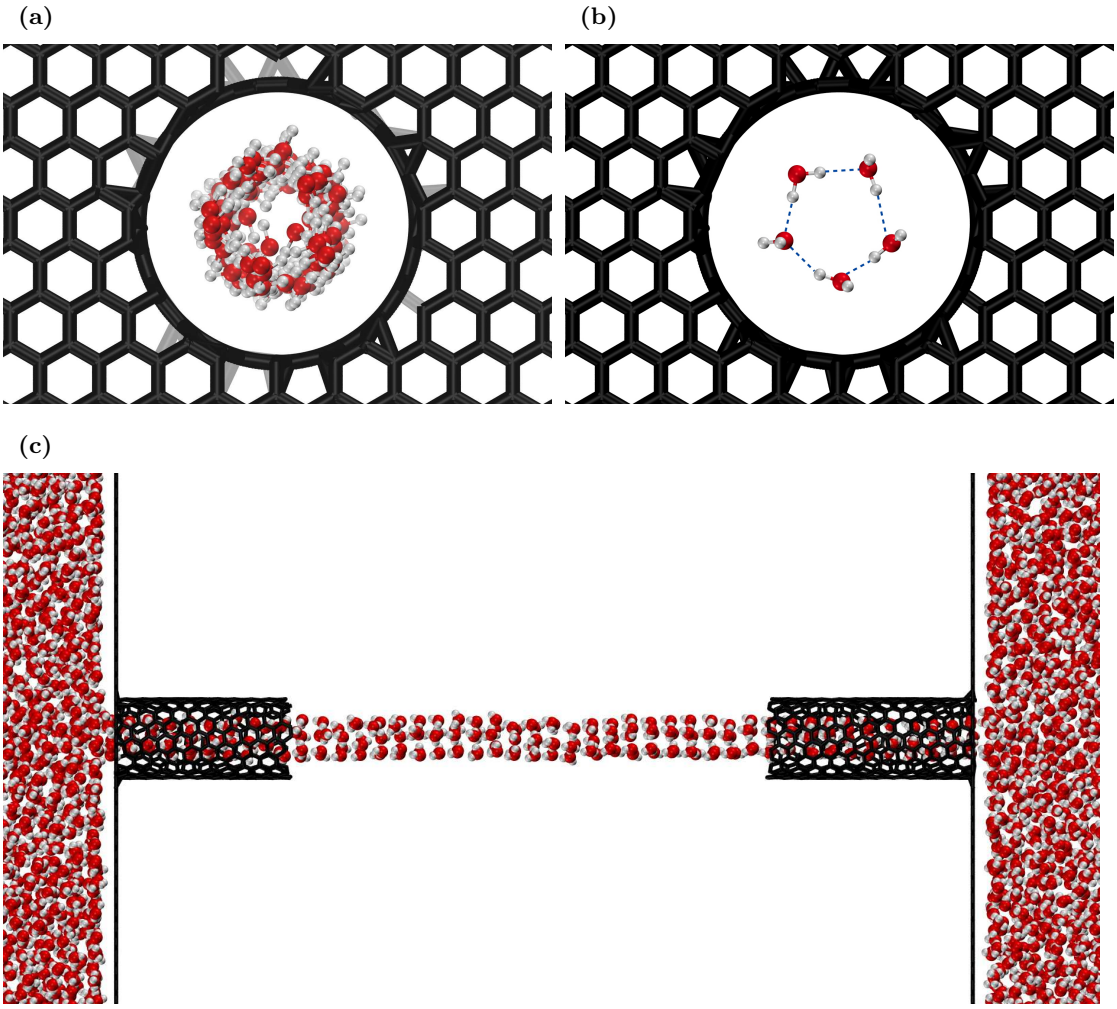

Figure 6.12: Snapshots from the junction IMM micro-element of the case replicating the experiment of Qin *et al.* [215]. **a**, Cross-sectional snapshot at the entrance of the CNT membrane. All the water molecules inside the CNT are visualised. **b**, Cross-sectional snapshot in the middle of the junction micro-element, only one layer of water molecules is shown. Dashed blues lines indicate the existence of hydrogen bonds (HB) according to the geometrical criterion of Luzar and Chandler [106]. **c**, Axial snapshot of the junction micro-element. The middle part of the CNT is not visualised in order to show more clearly the ordering of the water molecules inside it.

volumetric to mass flow rate and *vice versa*.

Figure 6.13a shows the mass flow rate measurements that the IMM simulations predicted at each iteration. The dashed line is the mass flow rate calculated from the enhancement value reported in Ref. [215], taking into account all the assumptions mentioned above. After only four iterations the agreement between the IMM results and the experimental data is very good. Similar observations can be made about Fig. 6.13b where the predicted flow enhancement is compared with the experimental

value.

At the fifth iteration, IMM predicts a flow enhancement factor of $\epsilon = 54.25$, while the experimental value from Qin *et al.* [215] is $\epsilon_{exp} = 51 \pm 1$. This very good qualitative agreement is despite the assumptions made during the calculations and the experiment. Further simulations of similar systems are, however, considered necessary before a solid opinion is formed regarding the accuracy and capability of the IMM for solving this type of problem.

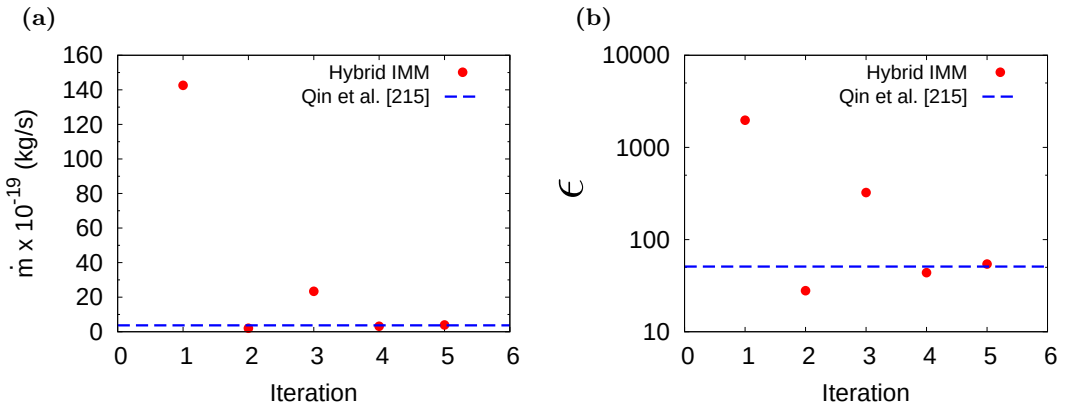

Figure 6.13: a, Mass flow rate measurements at each iteration of the IMM. Blue dashed line show the experimental mass flow rate calculated by Qin *et al.* [215]. **b,** Flow enhancement calculation at each iteration of the IMM. Blue dashed line shows the enhancement reported by Qin *et al.* [215]

The convergence of IMM in this case (see Fig. 6.14a) shows the same behaviour as in all previous simulations presented in this thesis. The variable relaxation factor ψ acts as an over-relaxation factor with large values. The method seems to be stable, despite the significant corrections taking place from iteration to iteration. Fig. 6.14b shows again how quickly (after only one iteration) the pressure difference along the CNT converges towards its final value. Due to the great length of the CNT in this application (L = 1 mm), pressure losses can completely be attributed to frictional losses.

Finally, it should be noted that the IMM simulation took 85 days of computational time (on one ARCHIE-WeSt node using the GPU) in order to perform all five iterations and provide the final result. According to the analysis in section 6.2.2, a pure MD simulation of the equivalent system would require $\sim$ 247 years.

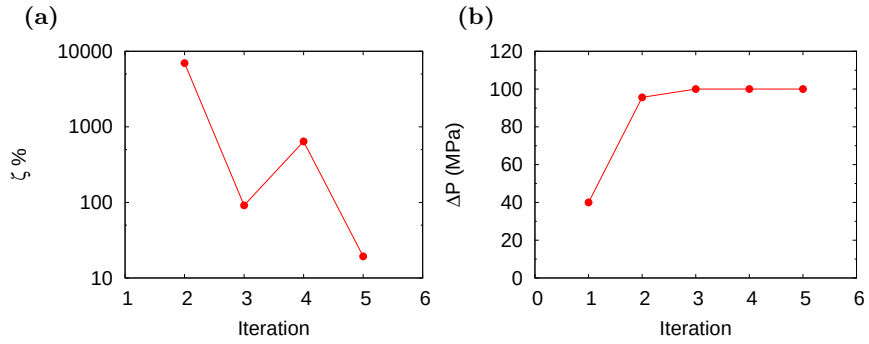

Figure 6.14: a, Convergence of the IMM simulation according to Eq. (5.7). **b,** Pressure difference along the CNT, excluding entrance/exit losses, calculated from the IMM simulation according to Eq. (5.5).

6.4 Summary

This chapter presented validation and performance simulations using the IMM on water-CNT membrane systems. The accuracy of the hybrid method is exceptional when compared to pure MD simulations of this case, while the computational performance improves as the size of the simulated problem increases. However, convergence issues are highlighted as possible sources of instabilities, for example, the freely variable relaxation factor ψ.

Simulations of two longer systems, and comparison with previous computational studies, showed satisfactory agreement. A modified Hagen-Poiseuille equation firstly proposed by Walther *et al.* [18], can be used as a tool for approximating the flow enhancement factor of CNT membranes of any length. Finally, the IMM was used to calculate the flow rate and enhancement through a 1 mm thick CNT membrane, replicating the experiment performed by Qin *et al.* [215]. The results were in good qualitatively agreement and in reasonable quantitative agreement too, taking into account the assumptions and errors during the experimental process. When IMM is applied to problems of this size, it is orders of magnitude more computationally efficient than pure MD simulations.

Further investigations into the method and additional simulations of benchmark cases are considered necessary. The results presented here, along with previous publications on LJ fluid systems, make IMM a candidate as a major computational tool of the near future for the study of multiscale channel flows.

Chapter 7

Conclusions

Γηράσκω δ' αιεί πολλά διδασκόμενος.
- Σόλων ο Αθηνέος (638-558 π.Χ.)

I grow old ever learning many things.
- Solon of Athens (638-558 B.C.)

This thesis has presented new simulation results on the behaviour of water at the nanoscale, including free surfaces as well as flowing in nanotubes. Based on the simulation results, new physical insights have been provided, and a new hybrid multiscale method has been validated for water flow through nanotube membranes of great relative thickness. This hybrid approach contributes a significant number of new results that directly connect molecular simulations with experimental observations. Hydrodynamic expressions that can quickly give estimations of the water flow along nanotubes were also presented.

Initially, an overview of the Molecular Dynamics (MD) method was given along with a validation of the code and the chosen water model. The TIP4P/2005 water model is the rigid model that can most accurately reproduce water properties such as surface tension, isothermal compressibility, self diffusion, shear viscosity and critical point properties. A salt (NaCl) model was also presented and validated in conjunction with the TIP4P/2005 water model for use in simulations of desalination processes.

Simulations of water nanodroplets on static and moving solid surfaces of various degrees of hydrophilicity were then performed. The interaction parameters between

the chosen water model and graphitic surfaces were calibrated in order to reproduce the macroscopically-observed water contact angle on these surfaces. The effect of solid-liquid interactions on the formation of water depletion layers and the cohesive strength of water molecules has been discussed. The effects of solid-liquid interaction and viscous dissipation were also investigated by setting the silicon and graphite surfaces moving. It was found that, for nanoscale droplets, the solid-liquid interactions play a vital role in determining the wetting dynamics, while viscous dissipation effects induced by the moving surface were found to be only slightly important for the silicon surface and negligible for the graphite surface. These observations are different from the wetting dynamics of macroscale droplets, which show a significant dependence on the capillary number.

Using the calibrated water-graphite potentials, the average orientation of water molecules in CNT membrane systems was studied. A method that can fully describe the ensemble order at a molecular level was developed based on liquid crystal's theory. The increase of anisotropy and biaxial ordering of the water molecules close to both the CNT wall and to the entrance of the CNT was revealed. The effect of an external axial static electric field on water orientation, anisotropy and flow behaviour for a pressure driven flow was also investigated. The results indicated that an axial electric field produces competing effects on the mass flow rate, reducing flow when the field affects molecules within the CNT but increasing flow rates when the field aligns molecules close to the inlet of the CNT. It therefore appears that an electric field can be used to pre-order water molecules, to form a paranematic biaxial phase, in a region close to the CNT entrance. This reduces entrance losses and produces much higher flow rates for the same applied pressure difference. A very high electric field can, however, change the phase of water from liquid to solid, leading to complete blocking of the flow through the CNT.

Molecular dynamics simulations of water flow in nanotubes of different materials were compared with an analytical model to show, quantitavely for the first time, the effect of solid-liquid molecular interactions on fluid flow in nanotubes. The unfavorable energetic interaction between water and the graphitic walls of CNTs results in significantly higher flow rates than in other nanotube materials like Boron Nitride or

Silicon Carbide. The proposed analytical model can satisfactorily predict the flow enhancement factors for nanotube membranes of small thickness. However, further development is required in order for it to be applicable to membranes with a nanotube length of practical engineering interest.

Hybrid multiscale approaches that combine molecular accuracy with the computational effectiveness of conventional macroscopic computational tools were reviewed. The theoretical justification for the further validation and development of the IMM approach for water flow in nanotube membranes was also presented. The IMM was presented in detail, including algorithmic aspects, alongside the assumptions made in the equations consisting it.

Finally, results of applying the IMM to water-CNT membrane systems were presented and compared with pure MD simulations for validation purposes. The hybrid method showed great accuracy, and its computational efficiency increases as the system size increases. The IMM outperforms conventional MD for membrane thicknesses greater than 1 μm, and can in fact produce results for problems that are impossible to simulate using pure MD even with state-of-the-art codes and hardware. The IMM results showed that flow enhancement reaches a plateau and does not continue to grow as the CNT length increases. A modified Hagen-Poiseuille equation has the potential to provide quick flow rate estimations if two flow parameters are known. A comparison of computational and experimental results was also satisfactory, taking into account the assumptions made.

This thesis has shown that despite the extensive research on water flow at the nanoscale there are still surprising and unexpected effects (e.g. electric field effect on flow rate), and phenomena to be explained and understood (e.g. importance of water nanotube wall interactions, flow enhancement growth and limits). Moreover, there are computationally efficient methods to be developed and improved (e.g. IMM) and macroscopic equations to be re-assessed that can potentially be applied to nanoscale problems (e.g. the modified Hagen-Poiseuille, Weissenberg equation). MD will always be a valuable tool to study fundamental effects and phenomena at the nanoscale, but the study of engineering multiscale problems will increasingly depend on a new family of hybrid simulation tools such as the IMM.

Future Work

Based on the work in this thesis there are a number of potential future studies and extensions:

1. The further development of the existing MD code in order to simulate other materials of engineering interest, like metals, metal oxides and ceramics. To achieve this there is the need for both validated interaction potentials and parameters that will reproduce the properties of the material, and fluid-solid interaction potentials. The inclusion of interactions among the solid atoms will also allow the study of heat transfer problems.

2. Further development and optimisation of the GPU software in order to perform MD simulations with minimum contribution from the CPU. The parallelisation of the GPU code along with the introduction of new hardware technologies (accelerators such as Intel's Phi, next generations GPUs, etc.) will enable the pure MD simulation of larger, more complicated problems, and for longer timescales too.

3. The current models and computational tools presented in this thesis allow the simulation of desalination processes. The inclusion of salt (NaCl) in the water - nanotube systems will enable the assessment of desalination efficiency of the various nanotubes.

4. Further simulations of nanodroplets on moving surfaces with larger droplets in order to investigate size effects. Additional measurements such as the velocity field in the droplet could provide further physical insight.

5. Applying the molecular kinetic theory to MD data will enable the user to extract the coefficient of contact line friction for a nanodroplet, the molecular jump frequency, and the molecular jump length. The effect of droplet size on the measured properties can also be reported as a function of liquid-Knudsen number [80], which is the ratio of the molecular jump length to the characteristic macroscopic length.

6. Further study of the effect of electromagnetic fields of various forms and combinations on water flow in a nanotube could reveal unknown phenomena. In addition to the interesting phenomena presented in this thesis (see Chapter 3) other recent studies present how rotating electric or electromagnetic fields can produce a flow along a nanochannel [135, 218].

7. CNT entrance functionalisation has already been studied with reference to its effect on desalination performance [163, 219]. However, the new method of measuring water molecule anisotropy and orientation in this thesis could guide researchers to more focused chemical and/or geometrical modifications.

8. The promising model of Mattia *et al.* [1] could be further developed in order to include entrance and exit losses in a nanotube. In combination with modified hydrodynamic equations, like the ones presented in Chapter 6, this could provide researchers and engineers with a quick and accurate flow rate prediction tool.

9. The effect of the variable relaxation coefficient ψ on the convergence and accuracy of the IMM needs further study. A comparison with an IMM simulation that uses a constant under-relaxation coefficient is suggested.

10. Another major assumption of the IMM approach that needs further investigation is the linear relationship between pressure and mass flow rate. MD simulations of the membrane case with various externally applied pressure differences will reveal whether this assumption is valid or not.

11. The IMM should be used to simulate nanotube membranes of even greater thickness. This will enable the direct comparison with other experimental studies, and confirm the enhancement limit proposed in this thesis.

12. A combination of the method recently published by Stephenson *et al.* [213] with those presented in Chapters 5 and 6 will enable the simulation for design of complex nanotube networks.

References

[1] D. Mattia and F. Calabrò. Explaining high flow rate of water in carbon nanotubes via solid-liquid molecular interactions. *Microfluid. Nanofluid.*, 13: 125–130, 2012.

[2] S. Iijima. Helical microtubes of graphitic carbon. *Nature*, 354: 56–58, 1991.

[3] A. Alexiadis and S. Kassinos. Molecular simulation of water in carbon nanotubes. *Chem. Rev.*, 108(12): 5014–5034, 2008.

[4] N. G. Portney and M. Ozkan. Nano-oncology: drug delivery, imaging and sensing. *Anal. Bioanal. Chem.*, 384(3): 620–630, 2006.

[5] R. Singh, D. Pantarotto, L. Lacerda, G. Pastorin, C. Klumpp, M. Prato, A. Bianco and K. Kostarelos. Tissue biodistribution and blood clearance rates for intravenously administered carbon nanotube radiotracers. *Proc. Natl. Acad. Sci. USA*, 103(9): 3357–3362, 2006.

[6] J. Kong, N. R. Franklin, C. W. Zhou, M. G. Chapline, S. Peng, K. J. Cho and H. J. Dai. Nanotube molecular wires as chemical sensors. *Science*, 287(5453): 622–625, 2000.

[7] E. S. Snow, F. K. Perkins, E. J. Houser, S. C. Badescu and T. L. Reinecke. Chemical detection with a single-walled carbon nanotube capacitor. *Science*, 307(5717): 1942–1945, 2005.

[8] D. Mattia and Y. Gogotsi. Review: static and dynamic behavior of liquids inside carbon nanotubes. *Microfluid. Nanofluid.*, 5: 289–305, 2008.

[9] K. P. Lee, T. C. Arnot and D. Mattia. A review of reverse osmosis membrane materials for desalination–development to date and future potential. *J. Membr. Sci.*, 370(1-2): 1–22, 2011.

[10] C. Liu, Y. Y. Fan, M. Liu, H. T. Cong, H. M. Cheng and M. S. Dresselhaus. Hydrogen storage in single-walled carbon nanotubes at room temperature. *Science*, 286(5442): 1127–1129, 1999.

[11] D. P. Cao, X. R. Zhang, J. F. Chen, W. C. Wang and J. Yun. Optimization of single-walled carbon nanotube arrays for methane storage at room temperature. *J. Phys. Chem. B*, 107(48): 13286–13292, 2003.

[12] R. H. Baughman, C. X. Cui, A. A. Zakhidov, Z. Iqbal, J. N. Barisci, G. M. Spinks, G. G. Wallace, A. Mazzoldi, D. D. Rossi, A. G. Rinzler, O. Jaschinski, S. Roth and M. Kertesz. Carbon nanotube actuators. *Science*, 284(5418): 1340–1344, 1999.

[13] V. Sazonova, Y. Yaish, H. Ustunel, D. Roundy, T. A. Arias and P. L. McEuen. A tunable carbon nanotube electromechanical oscillator. *Nature*, 431(7006): 284–287, 2004.

[14] M. C. Gordillo and J. Martí. Hydrogen bond structure of liquid water confined in nanotubes. *Chem. Phys. Lett.*, 329: 341–345, 2000.

[15] F. Franks. *Water: A Comprehensive Treatise*. Plenum Press, 1979.

[16] G. Karniadakis, A. Beskok and N. Aluru. *Microflows and Nanoflows. Fundamentals and Simulation*. Springer, 2005.

[17] M. S. P. Sansom, I. D. Kerr, J. Breed and R. Sankararamakrishnan. Water in channel-like cavities: structure and dynamics. *Biophys. J.*, 70(2): 693–702, 1996.

[18] J. H. Walther, K. Ritos, E. R. Cruz-Chu, C. M. Megaridis and P. Koumoutsakos. Barriers to superfast water transport in carbon nanotube membranes. *Nano Lett.*, 13: 1910–1914, 2013.

[19] S. Joseph and N. R. Aluru. Why are carbon nanotubes fast transporters of water? *Nano Lett.*, 8(2): 452–458, 2008.

[20] J. A. Thomas and A. J. H. McGaughey. Water flow in carbon nanotubes: Transition to subcontinuum transport. *Phys. Rev. Lett.*, 102: 184502, 2009.

[21] D. W. Brenner. Empirical potential for hydrocarbons for use in simulating the chemical vapor deposition of diamond films. *Phys. Rev. B*, 42(15): 9458–9471, 1990.

[22] K. Malek and M. Sahimi. Molecular dynamics simulations of adsorption and diffusion of gases in silicon-carbide nanotubes. *J. Chem. Phys.*, 132: 014310, 2010.

[23] N. Dongari, Y. Zhang and J. M. Reese. Molecular free path distribution in rarefied gases. *J. Phys. D: Appl. Phys.*, 44(12): 125502, 2011.

[24] Y. Y. Zhang, Y. Cheng, Q. X. Pei, C. M. Wang and Y. Xiang. Thermal conductivity of defective graphene. *Phys. Lett. A*, 376: 3668–3672, 2012.

[25] B. Mortazavi and Y. Rémond. Investigation of tensile response and thermal conductivity of boron-nitride nanosheets using molecular dynamics simulations. *Physica E*, 44: 1846–1852, 2012.

[26] N. Klomkliang, D. D. Do, D. Nicholson, C. Tangsathitkulchai and A. Wongkoblap. Multilayer adsorption of benzene on graphitised thermal carbon black—The importance of quadrupole and explicit hydrogen in the potential model. *Chem. Eng. Sci.*, 69: 472–482, 2012.

[27] N. Dongari, R. W. Barber, D. R. Emerson, S. K. Stefanov, Y. Zhang and J. M. Reese. The effect of Knudsen layers on rarefied cylindrical Couette gas flows. *Microfluid. Nanofluid.*, 14: 31–43, 2013.

[28] F. Taghavi, S. Javadian and S. M. Hashemianzadeh. Molecular dynamics simulation of single-walled silicon carbide nanotubes immersed in water. *J. Mol. Graphics Modell.*, 44: 33–43, 2013.

[29] M.-Q. Le and R. C. Batra. Single-edge crack growth in graphene sheets under tension. *Comput. Mater. Sci.*, 69: 381–388, 2013.

[30] K. Falk, F. Sedlmeier, L. Joly, R. R. Netz and L. Bocquet. Ultralow liquid/solid friction in carbon nanotubes: Comprehensive theory for alcohols, alkanes, OMCTS and water. *Langmuir*, 28: 14261–14272, 2012.

[31] S. K. Kannam, B. D. Todd, J. S. Hansen and P. J. Daivis. Interfacial slip friction at a fluid-solid cylindrical boundary. *J. Chem. Phys.*, 136: 244704, 2012.

[32] W. D. Nicholls, M. K. Borg, D. A. Lockerby and J. M. Reese. Water transport through (7,7) carbon nanotubes of different lengths using molecular dynamics. *Microfluid. Nanofluid.*, 12: 257–264, 2012.

[33] L. Wang, R. S. Dumont and J. M. Dickson. Nonequilibrium molecular dynamics simulation of pressure-driven water transport through modified CNT membranes. *J. Chem. Phys.*, 138: 124701, 2013.

[34] M. P. Allen and D. J. Tildesley. *Computer Simulation of Liquids.* Oxford University Press, 1991.

[35] F. Ercolessi. A molecular dynamics primer. Technical report, International School for Advanced Studies, 1997.

[36] D. Frenkel and B. Smit. *Understanding Molecular Simulation.* Academic Press, 2002.

[37] D. C. Rapaport. *The Art of Molecular Dynamics Simulation.* Cambridge University Press, 2004.

[38] G. B. Macpherson, M. K. Borg and J. M. Reese. Generation of initial molecular dynamics configurations in arbitrary geometries and in parallel. *Mol. Simul.*, 33(15): 1199–1212, 2007.

[39] G. B. Macpherson and J. M. Reese. Molecular dynamics in arbitrary geometries: parallel evaluation of pair forces. *Mol. Simul.*, 34(1): 97–115, 2008.

[40] G. B. Macpherson, N. Nordin and H. G. Weller. Particle tracking in unstructured, arbitrary polyhedral meshes for use in CFD and molecular dynamics. *Commun. Numer. Meth. Engng.*, 25(3): 263–273, 2009.

[41] M. K. Borg, G. B. Macpherson and J. M. Reese. Controllers for imposing continuum-to-molecular boundary conditions in arbitrary fluid flow geometries. *Mol. Simul.*, 36(10): 745–757, 2010.

[42] OpenCFD Ltd. http://www.openfoam.org, 2014.

[43] L. de Broglie. *Recherches sur la théorie des quanta (Researches on the quantum theory).* Ph.D. thesis, Faculty of Sciences at Paris University, 1924.

[44] J. P. Hansen and I. R. McDonald. *Theory of simple liquids.* Academic Press, 3rd edition, 2006.

[45] M. K. Borg. *Hybrid Molecular-Continuum Modelling of Nano-Scale Flows.* Ph.D. thesis, University of Strathclyde, 2010.

[46] W. D. Nicholls. *Molecular Dynamics Simulations of Liquid Flow in and around Carbon Nanotubes.* Ph.D. thesis, University of Strathclyde, 2012.

[47] P. Angelikopoulos, C. Papadimitriou and P. Koumoutsakos. Data driven, predictive molecular dynamics for nanoscale flow simulations under uncertainty. *J. Phys. Chem. B*, 117: 14808–14816, 2013.

[48] T. Werder, J. H. Walther, R. L. Jaffe, T. Halicioglu and P. Koumoutsakos. On the water-carbon interaction for use in molecular dynamics simulations of graphite and carbon nanotubes. *J. Phys. Chem. B*, 107: 1345–1352, 2003.

[49] J. S. Hansen, T. B. Schrøder and J. C. Dyre. Simplistic Coulomb forces in molecular dynamics: Comparing the Wolf and shifted-force approximations. *J. Phys. Chem. B*, 116: 5738–5743, 2012.

[50] J. L. F. Abascal and C. Vega. A general purpose model for the condenced phases of water: TIP4P/2005. *J. Chem. Phys.*, 123: 234505, 2005.

[51] C. Vega and J. L. F. Abascal. Simulating water with rigid non-polarizable models: a general perspective. *Phys. Chem. Chem. Phys.*, 13: 19663–19688, 2011.

[52] D. J. Huggins. Correlations in liquid water for the TIP3P-Ewald, TIP4P-2005, TIP5P-Ewald, and SWM4-NDP models. *J. Chem. Phys.*, 136: 064518, 2012.

[53] H. W. Horn, W. C. Swope, J. W. Pitera, J. D. Madura, T. J. Dick, G. L. Hura and T. Head-Gordon. Development of an improved four-site water model for biomolecular simulations: TIP4P-Ew. *J. Chem. Phys.*, 120(20): 9665–9678, 2004.

[54] J. Alejandre, G. A. Chapela, F. Bresme and J.-P. Hansen. The short range anion-H interaction is the driving force for the crystal formation of ions in water. *J. Chem. Phys.*, 130: 174505, 2009.

[55] A. K. Soper and M. G. Phillips. A new determination of the structure of water at 25° C. *Chem. Phys.*, 107(1): 47–60, 1986.

[56] P. Postorino, M. A. Ricci and A. K. Soper. Water above its boiling point: Study of the temperature and density dependence of the partial pair correlation functions. I. Neutron diffraction epxeriment. *J. Chem. Phys.*, 101(5): 4123–4132, 1994.

[57] G. B. Macpherson. *Molecular Dynamics Simulation in Arbitrary Geometries for Nanoscale Fluid Mechanics*. Ph.D. thesis, University of Strathclyde, 2008.

[58] M. K. Borg, D. A. Lockerby and J. M. Reese. A hybrid molecular-continuum simulation method for incompressible flows in micro/nanofluidic networks. *Microfluid. Nanofluid.*, 15(4): 541–557, 2013.

[59] M. K. Borg, D. A. Lockerby and J. M. Reese. The FADE mass-stat: A technique for inserting or deleting particles in molecular dynamics simulations. *J. Chem. Phys.*, 140: 074110, 2014.

[60] M. K. Borg, D. A. Lockerby and J. M. Reese. A multiscale method for micro/nano flows of high aspect ratio. *J. Comput. Phys.*, 233: 400–413, 2013.

[61] P. G. de Gennes. Wetting: statics and dynamics. *Rev. Mod. Phys.*, 57(3): 827–863, 1985.

[62] K. Lum, D. Chandler and J. D. Weeks. Hydrophobicity at small and large length scales. *J. Phys. Chem. B*, 103(22): 4570–4577, 1999.

[63] F. H. Stillinger. Structure and aqua solutions of nonpolar solutes from the standpoint of scaled-particle theory. *J. Solution Chem.*, 2(2-3): 141–158, 1973.

[64] Y. C. Jung and B. Bhushan. Dynamic effects induced transition of droplets on biomimetic superhydrophobic surfaces. *Langmuir*, 25: 9208–9218, 2009.

[65] B. Bhushan and Y. C. Jung. Natural and biomimetic artificial surfaces for superhydrophobicity, self-cleaning, low adhesion, and drag reduction. *Prog. Mater. Sci.*, 56(1): 1–108, 2011.

[66] B. Bhushan. *Biomimetics: Bioinspired Hierachical-Structured Surfaces for Green Science and Technology*. Springer: Heidelberg, 2012.

[67] D. M. Huang, C. Chandler, D. Horinek, R. R. Netz and L. Bocquet. Water slippage versus contact angle: A quasiuniversal relationship. *Phys. Rev. Lett.*, 101(22): 226101–226104, 2008.

[68] J. Janecek and R. R. Netz. Interfacial water at hydrophobic and hydrophilic surfaces: Depletion versus adsorption. *Langmuir*, 23(16): 8417–8429, 2007.

[69] D. Chandler. Physical chemistry: Oil on troubled waters. *Nature*, 445: 831–832, 2007.

[70] N. Dongari. Liquid slip/stick over hydrophobic/hydrophilic surfaces and their implications in coating processes. *Chem. Eng. Process.*, 50: 450–453, 2011.

[71] R. Tadmor. Approaches in wetting phenomena. *Soft Matter*, 7: 1577–1580, 2011.

[72] D. Duviver, D. Seveno, R. Rioboo, T. D. Blake and J. Coninck. Experimental evidence of the role of viscosity in the molecular kinetic theory of dynamic wetting. *Langmuir*, 27(21): 13015–13021, 2011.

[73] T. D. Blake. The physics of moving wetting lines. *J. Colloid Interface Sci.*, 299(1): 1–13, 2006.

[74] W. Ren and W. E. Boundary conditions for the moving contact line problem. *Phys. Fluids*, 19: 022101, 2007.

[75] J. C. Bird, S. Mandre and H. A. Stone. Short-time dynamics of partial wetting. *Phys. Rev. Lett.*, 100: 234501, 2008.

[76] C. Huh and L. E. Scriven. Hydrodynamic model of steady movement of solid/liquid/fluid contact line. *J. Colloid Interface Sci.*, 35(1): 85–101, 1971.

[77] O. V. Voinov. Hydrodynamics of wetting. *Fluid Dynamics*, 11(5): 714–721, 1976.

[78] D. Jacqmin. Contact-line dynamics of a diffuse fluid interface. *J. Fluid Mech.*, 402: 57–88, 2000.

[79] J. W. Cahn and J. E. Hilliard. Free energy of a nonuniform system. I. Interfacial free energy. *J. Chem. Phys.*, 28(2): 258–267, 1958.

[80] A. Carlson, M. Do-Quang and G. Amberg. Modeling of dynamic wetting far from equilibrium. *Phys. Fluids*, 21(121701), 2009.

[81] S. Chakraborty. Generalization of interfacial electrohydrodynamics in the presence of hydrophobic interactions in narrow fluidic confinements. *Phys. Rev. Lett.*, 100(9): 097801–4, 2008.

[82] E. R. Cruz-Chu and K. Shulten. Water-silica force field for simulating nanodevices. *J. Phys. Chem. B*, 110: 21497–21508, 2006.

[83] J. T. Hirvi and T. A. Pakkanen. Molecular dynamics simulations of water droplets on polymer surfaces. *J. Chem. Phys.*, 125(14): 144712, 2006.

[84] M. Lundgren, N. L. Allan and T. Cosgrove. A molecular dynamics study of wetting of a pillar-surface. *Langmuir*, 19: 7127–7129, 2003.

[85] M. Schneemilch and N. J. Quirke. Effect of oxidation on the wettability of poly(dimethylsiloxane) surfaces. *J. Chem. Phys.*, 127(114701): 114701, 2007.

[86] G. Scocchi, D. Sergi, C. D'Angelo and A. Ortona. Wetting and contact-line effects for spherical and cylindrical droplets on graphene layers: A comparative molecular-dynamics investigation. *Phys. Rev. E*, 84: 061602, 2011.

[87] A. Malani, A. Reghavanpillai, E. B. Wysong and G. C. Rutledge. Can dynamic contact angle be measured using molecular modeling? *Phys. Rev. Lett.*, 109: 184501, 2012.

[88] D. Sergi, G. Scocchi and A. Ortona. Molecular dynamics simulations of the contact angle between water droplets and graphite surfaces. *Fluid Phase Equilib.*, 332: 173–177, 2012.

[89] E. E. Santiso, C. Herdes and E. A. Müller. On the calculation of solid-fluid contact angles from molecular dynamics. *Entropy*, 15: 3734–3745, 2013.

[90] F.-C. Wang and Y.-P. Zhao. Contact angle hysteresis at the nanoscale: a molecular dynamics simulation study. *Colloid Polym. Sci.*, 291(2): 307–315, 2013.

[91] T. Koishi, K. Yasuoka, S. Fujikawa and X. C. Zeng. Measurement of contact-angle hysteresis for droplets on nanopillared surface and in the Cassie and Wenzel states: A molecular dynamics simulation study. *ACS Nano*, 5(9): 6834–6842, 2011.

[92] E. S. Savoy and F. A. Escobedo. Molecular simulations of wetting of a rough surface by an oily fluid: Effect of topology, chemistry, and droplet size on wetting transition rates. *Langmuir*, 28: 3412–3419, 2012.

[93] W.-J. Jeong, M. Y. Ha, H. S. Yoon and M. Ambrosia. Dynamic behaviour of water droplets on solid surfaces with pillar-type nanostructures. *Langmuir*, 28: 5360–5371, 2012.

[94] R. C. Dutta, S. Khan and J. K. Singh. Wetting transition of water on graphite and boron-nitride surfaces: A molecular dynamics study. *Fluid Phase Equilib.*, 302: 310–315, 2011.

[95] M. S. Ambrosia, M. Y. Ha and S. Balachandar. The effect of pillar surface fraction and pillar height on contact angles using molecular dynamics. *Appl. Surf. Sci.*, 282: 211–216, 2013.

[96] M. Yan, X. Yang and Y. Lu. Wetting behavior of water droplet on solid surfaces in solvent environment: A molecular simulation study. *Colloid Surface A*, 429: 142–148, 2013.

[97] A. Shahraz, A. Borhan and K. A. Fichthorn. Wetting on physically patterned solid surfaces: The relevance of molecular dynamics simulations to macroscopic systems. *Langmuir*, 29: 11632–11639, 2013.

[98] S. Khan and J. K. Singh. Wetting transition of nanodroplets of water on textured surfaces: a molecular dynamics study. *Mol. Simul.*, 40(6): 458–468, 2014.

[99] Y. Jiang, J. T. Hirvi, M. Suvanto and T. A. Pakkanen. Molecular dynamic simulations of anisotropic wetting and embedding on functionalized polypropylene surfaces. *Chem. Phys.*, 429: 44–50, 2014.

[100] J. C. Walter. *The Coating Processes*. Tappi Press, Atlanta, 1993.

[101] S. F. Kistler and P. M. Shcweizer. *Liquid Film Coating*. Chapman & Hall, London, 1997.

[102] S. J. Weinstein and K. J. Ruschak. Coating flows. *Annu. Rev. Fluid. Mech*, 36: 29–53, 2004.

[103] W. C. Nelson, P. Sen and C.-J. Kim. Dynamic contact angles and hysteresis under electrowetting-on-dielectric. *Langmuir*, 27: 10319–10326, 2011.

[104] B. Sobac and D. Brutin. Thermal effects of the substrate on water droplet evaporation. *Phys. Rev. E*, 86: 021602, 2012.

[105] M. J. de Ruijter, T. D. Blake and J. Coninck. Dynamic wetting studied by molecular modeling simulations of droplet spreading. *Langmuir*, 15: 7836–7847, 1999.

[106] A. Luzar and D. Chandler. Hydrogen-bond kinetics in liquid water. *Nature*, 379: 55–57, 1996.

[107] F. M. Fowkes and W. D. Harkins. The state of monolayers adsorbed at the interface solid-aqueous solution. *JACS*, 62: 3377–3386, 1940.

[108] J. W. Gibbs. *The Scientific Papers of J. Willard Gibbs*, volume 1. Dover Publications, 1961.

[109] L. Boruvka and A. W. Neumann. Generalization of the classical theory of capillarity. *J. Chem. Phys.*, 66(12): 5464–5476, 1977.

[110] B. A. Pethica. The contact angle equilibrium. *J. Colloid Interface Sci.*, 62(3): 567–569, 1977.

[111] J. Y. Wang, S. Betelu and B. M. Law. Line tension approaching a first-order wetting transition: Experimental results from contact angle measurements. *Phys. Rev. E*, 63(3): 031601, 2001.

[112] F. Mugele, T. Becker, R. Nikopoulos, M. Kohonen and S. Herminghaus. Capillarity at the nanoscale: an AFM view. *J. Adhesion Sci. Technol.*, 16(7): 951–964, 2002.

[113] R. T. Cygan, J.-J. Liang and A. G. Kalinichev. Molecular models of hydroxide, oxyhydroxide, and clay phases and the development of a general force field. *J. Phys. Chem. B*, 108: 1255–1266, 2004.

[114] A. A. Skelton, P. Fenter, J. D. Kubicki, D. J. Wesolowski and P. Cummings. Simulations of the quartz(1011)/water interface: A comparison of classical force fields, ab initio molecular dynamics, and x-ray reflectivity experiments. *J. Phys. Chem. C*, 115: 2076–2088, 2011.

[115] K. Hermansson, U. Lindberg, B. Hok and G. Palmskog. Wetting properties of silicon surfaces. *International Conference on Solid-State Sensors and Actuators*, pages 193–196, 1991.

[116] K. Kashimoto, J. Yoon, B. Hou, C. H. Chen, B. Lin, M. Arotono, T. Takiue and M. L. Schlossman. Structure and depletion at fluorocarbon and hydrocarbon/water liquid/liquid interfaces. *Phys. Rev. Lett.*, 101(7): 076102, 2008.

[117] D. C. Tretheway and C. D. Meinhart. Apparent fluid slip at hydrophobic microchannel walls. *Phys. Fluids*, 14: L9–L12, 2002.

[118] M. Whitby and N. Quirke. Fluid flow in carbon nanotubes and nanopipes. *Nat. Nanotechnol.*, 2: 87–94, 2007.

[119] S. Vaitheeswaran, J. C. Rasaiah and G. Hummer. Electric field and temperature effects on water in the narrow nonpolar pores of carbon nanotubes. *J. Chem. Phys.*, 121: 7955–7965, 2004.

[120] J. Dzubiella and J. P. Hansen. Electric-field-controlled water and ion permeation of a hydrophobic nanopore. *J. Chem. Phys.*, 122(23): 234706, 2005.

[121] J. C. Rasaiah, S. Garde and G. Hummer. Water in nonpolar confinement: From nanotubes to proteins and beyond. *Annu. Rev. Phys. Chem.*, 59: 713–740, 2008.

[122] J. A. Thomas, A. J. H. McGaughey and O. Kuter-Arnebeck. Pressure-driven water flow through carbon nanotubes: Insights from molecular dynamics simulation. *Int. J. Therm. Sci.*, 49: 281–289, 2010.

[123] K. Ritos, D. Mattia, F. Calabrò and J. M. Reese. Flow enhancement in nanotubes of different materials and lengths. *J. Chem. Phys.*, 140: 014702, 2014.

[124] C. C. Cruickshank, R. F. Minchin, A. C. Le-Dain and B. Martinac. Estimation of the pore size of the large-conductance mechanosensitive ion channel of Escherichia coli. *Biophys. J.*, 73: 1925–1931, 1997.

[125] D. P. Tieleman, H. Leontiadou, A. E. Mark and S. J. Marrink. Simulation of pore formation in lipid bilayers by mechanical stress and electric fields. *J. Am. Chem. Soc.*, 125: 6382–6383, 2003.

[126] G. D. Matteis, A. M. Sonnet and E. G. Virga. Landau theory for biaxial nematic liquid crystals with two order parameter tensors. *Continuum Mech. Thermodyn.*, 20: 347–374, 2008.

[127] A. M. Sonnet and E. G. Virga. *Dissipative Ordered Fluids, Theories for Liquid Crystals.* Springer, 2012.

[128] G. R. Luckhurst. Biaxial nematic liquid crystals: fact or fiction? *Thin Solid Films*, 393: 40–52, 2001.

[129] L. A. Madsen, T. J. Dingemans, N. Nakata and E. T. Samulski. Thermotropic biaxial nematic liquid crystals. *Phys. Rev. Lett.*, 92(14): 145505, 2004.

[130] V. Prasad, S.-W. Kang, K. A. Suresh, L. Joshi, Q. Wang and S. Kumar. Thermotropic uniaxial and biaxial nematic and smectic phases in bent-core mesogens. *J. Am. Chem. Soc.*, 127: 17224–17227, 2005.

[131] G. R. Luckhurst, S. Naemura, T. J. Sluckin, K. S. Thomas and S. S. Turzi. Molecular-field-theory approach to the Landau theory of liquid crystals: Uniaxial and biaxial nematics. *Phys. Rev. E*, 85: 031705, 2012.

[132] X. Gong, J. Li, H. Lu, R. Wan, J. Li, J. Hu and H. Fang. A charge-driven molecular water pump. *Nat. Nanotechnol.*, 2(11): 709–712, 2007.

[133] M. E. Suk and N. R. Aluru. Effect of induced electric field on single-file reverse osmosis. *Phys. Chem. Chem. Phys.*, 11: 8614–8619, 2009.

[134] R. Srivastava, J. K. Singh and P. T. Cummings. Effect of electric field on water confined in graphite and mica pores. *J. Phys. Chem. C*, 116(33): 17594–17603, 2012.

[135] X.-P. Li, G.-P. Kong, X. Zhang and G.-W. He. Pumping of water through carbon nanotubes by rotating electric field and rotating magnetic field. *Appl. Phys. Lett.*, 103: 143117, 2013.

[136] P. Kaiser, W. Wiese and S. Hess. Stability and instability of an uniaxial alignment against biaxial distortions in the isotropic and nematic phases of liquid crystals. *J. Non-Equilib. Thermodyn.*, 17: 153–169, 1992.

[137] X. Zhou and Z. Zhang. Dynamics of order reconstruction in a nanoconfined nematic liquid crystal with a topological defect. *Int. J. Mol. Sci.*, 14: 24135–24153, 2013.

[138] V. P. Sokhan, D. Nicholson and N. Quirke. Fluid flow in nanopores: Accurate boundary conditions for carbon nanotubes. *J. Chem. Phys.*, 117: 8531–8539, 2002.

[139] D. H. Jung, J. H. Yang and M. S. Jhon. The effect of an external electric field on the structure of liquid water using molecular dynamics simulations. *Chem. Phys.*, 244: 331–337, 1999.

[140] H. Hu, H. Hou and B. Wang. Molecular dynamics simulations of ice growth from supercooled water when both electric and magnetic fields are applied. *J. Phys. Chem. C*, 116: 19773–19780, 2012.

[141] B. Roux. The membrane potential and its representation by a constant electric field in computer simulations. *Biophys. J.*, 95: 4205–4216, 2008.

[142] J. Gumbart, F. Khalili-Araghi, M. Sotomayor and B. Roux. Constant electric field simulations of the membrane potential illustrated with simple systems. *Biochim. Biophys. Acta*, 1818: 294–302, 2012.

[143] S. Mashaghi, T. Jadidi, G. Koenderink and A. Mashaghi. Lipid nanotechnology. *Int. J. Mol. Sci.*, 14: 4242–4282, 2013.

[144] F. Zhu, E. Tajkhorshid and K. Schulten. Pressure-induced water transport in membrane channels studied by molecular dynamics. *Biophys. J.*, 83(1): 154–160, 2002.

[145] W. D. Nicholls, M. K. Borg, D. A. Lockerby and J. M. Reese. Water transport through carbon nanotubes with defects. *Mol. Simul.*, 38(10): 781–785, 2012.

[146] G. Raabe and R. J. Sadus. Molecular dynamics simulation of the effect of bond flexibility on the transport properties of water. *J. Chem. Phys.*, 137: 104512, 2012.

[147] S. K. Kannam, B. D. Todd, J. S. Hansen and P. J. Daivis. How fast does water flow in carbon nanotubes? *J. Chem. Phys.*, 138: 094701, 2013.

[148] J. Koplik, J. R. Banavar and J. F. Willemsen. Molecular dynamics of Poiseuille flow and moving contact lines. *Phys. Rev. Lett.*, 60: 1282–1285, 1988.

[149] K. P. Travis and K. E. Gubbins. Poiseuille flow of Lennard-Jones fluids in narrow slit pores. *J. Chem. Phys.*, 112(4): 1984–1994, 2000.

[150] X.-J. Fan, N. Phan-Thien, N. T. Yong and X. Diao. Molecular simulation of liquid in a complex nano channel flow. *Phys. Fluids*, 14(3): 1146–1153, 2002.

[151] F. Zhu, E. Tajkhorshid and K. Schulten. Theory and simulation of water permeation in aquaporin-1. *Biophys. J.*, 86(1): 50–57, 2004.

[152] C. Polk. Biological applications of large electric fields: Some history and fundamentals. *IEEE Trans. Plasma Sci.*, 28(1): 6–14, 2000.

[153] J. Dzubiella, R. J. Allen and J. P. Hansen. Electric field-controlled water permeation coupled to ion transport through a nanopore. *J. Chem. Phys.*, 120(11): 5001–5004, 2004.

[154] S. W. I. Siu and R. A. Böckmann. Electric field effects on membranes: Gramicidin A as a test ground. *J. Struct. Biol.*, 157: 545–556, 2007.

[155] D. P. Tieleman. The molecular basis of electroporation. *BMC Biochemistry*, 5(10), 2004.

[156] M. Deminsky, A. Eletskii, A. Kniznik, A. Odinokov, V. Pentkovskii and B. Potapkin. Molecular dynamics simulation of transmembrane pore growth. *J. Membrane Biol.*, 246: 821–831, 2013.

[157] D. Bratko, C. D. Daub and A. Luzar. Field-exposed water in a nanopore: liquid or vapor? *Phys. Chem. Chem. Phys.*, 10: 6807–6813, 2008.

[158] J. Y. Yan and G. N. Patey. Molecular dynamics simulations of ice nucleation by electric fields. *J. Phys. Chem. A*, 116(26): 7057–7064, 2012.

[159] T. Sisan and S. Lichter. The end of nanochannels. *Microfluid. Nanofluid.*, 11(6): 787–791, 2011.

[160] M. Majumder and B. Corry. Anomalous decline of water transport in covalently modified carbon nanotube membranes. *Chem. Commun.*, 47(27): 7683–7685, 2011.

[161] D. Mattia, H. H. Bau and Y. Gogotsi. Wetting of CVD carbon films by polar and nonpolar liquids and implications for carbon nanopipes. *Langmuir*, 22: 1789–1794, 2006.

[162] D. Mattia, M. P. Rossi, B. M. Kim, G. Korneva, H. H. Bau and Y. Gogotsi. Effect of graphitization on the wettability and electrical conductivity of CVD-carbon nanotubes and films. *J. Phys. Chem. B*, 110: 9850–9855, 2006.

[163] B. Corry. Water and ion transport through functionalised carbon nanotubes: implications for desalination technology. *Energy Environ. Sci.*, 4(3): 751–759, 2011.

[164] C. Neto, D. R. Evans, E. Bonaccursi, H. J. Butt and V. S. J. Craig. Boundary slip in Newtonian liquids: a review of experimental studies. *Rep. Prog. Phys.*, 68: 2859–2897, 2005.

[165] T. Myers. Why are slip lengths so large in carbon nanotubes? *Microfluid. Nanofluid.*, 10(5): 1141–1145, 2010.

[166] J. S. Hansen, B. D. Todd and P. J. Daivis. Prediction of fluid velocity slip at solid surfaces. *Phys. Rev. E*, 84: 016313, 2011.

[167] M. Menon and D. Srivastava. Structure of boron nitride nanotubes: tube closing versus chirality. *Chem. Phys. Lett.*, 307: 407–412, 1999.

[168] D. Golberg, Y. Bando, C. Tang and C. Zhi. Boron nitride nanotubes. *Adv. Mater.*, 19: 2413–2432, 2007.

[169] C. Zhi, Y. Bando, C. Tang and D. Golberg. Boron nitride nanotubes. *Mater. Sci. Eng. R*, 70: 92–111, 2010.

[170] M. Menon, E. Richter, A. Mavrandonakis, G. Froudakis and A. Andriotis. Structure and stability of SiC nanotubes. *Phys. Rev. B*, 69(115322): 1–4, 2004.

[171] C. Y. Won and N. R. Aluru. Water permeation through a subnanometer boron nitride nanotube. *J. Am. Chem. Soc.*, 129: 2748–2749, 2007.

[172] C. Y. Won and N. R. Aluru. Structure and dynamics of water confined in a boron nitride nanotube. *J. Phys. Chem. C*, 112: 1812–1818, 2008.

[173] M. E. Suk, A. V. Raghunathan and N. R. Aluru. Fast reverse osmosis using boron nitride and carbon nanotubes. *Appl. Phys. Lett.*, 92: 133120, 2008.

[174] T. A. Hilder, D. Gordon and S.-H. Chung. Boron nitride nanotubes selectively permeable to cations or anions. *Small*, 5(24): 2870–2875, 2009.

[175] T. A. Hilder, D. Gordon and S.-H. Chung. Salt rejection and water transport through boron nitride nanotubes. *Small*, 5(19): 2183–2190, 2009.

[176] C. Y. Won and N. R. Aluru. A chloride ion-selective boron nitride nanotube. *Chem. Phys. Lett.*, 478: 185–190, 2009.

[177] M. Khademi and M. Sahimi. Molecular dynamics simulation of pressure-driven water flow in silicon-carbide nanotubes. *J. Chem. Phys.*, 135: 204509, 2011.

[178] R. Yang, T. A. Hilder, S.-H. Chung and A. Rendell. First-principles study of water confined in single-walled silicon carbide nanotubes. *J. Phys. Chem. C*, 115: 17255–17264, 2011.

[179] F. M. Garakani and R. Kalantarinejad. A molecular dynamics simulation of water transport through C and SiC nanotubes: Application for desalination. *Int. J. Nano Dim.*, 2(3): 151–157, 2012.

[180] T. A. Hilder, R. Yang, D. Gordon, A. P. Rendell and S.-H. Chung. Silicon carbide nanotube as a chloride-selective channel. *J. Phys. Chem. C*, 116: 4465–4470, 2012.

[181] C. L. Kong. Combining rules for intermolecular potential parameters. II. rules for the Lennard Jones (12-6) potential and the Morse potential. *J. Chem. Phys.*, 59(5): 2464–2467, 1973.

[182] L. A. J. Bastien, P. N. Price and N. J. Brown. Intermolecular potential parameters and combining rules determined from viscosity data. *Int. J. Chem. Kinet.*, 42(12): 713–723, 2010.

[183] J. A. Thomas and A. J. H. McGaughey. Reassessing fast water transport through carbon nanotubes. *Nano Lett.*, 8(9): 2788–2793, 2008.

[184] F. Calabrò, K. P. Lee and D. Mattia. Modelling flow enhancement in nanochannels: Viscosity and slippage. *Appl. Math. Lett.*, 26(10): 991–994, 2013.

[185] J. H. Park and N. R. Aluru. Ordering-induced fast diffusion of nanoscale water film on graphene. *J. Phys. Chem. C*, 114(6): 2595–2599, 2010.

[186] M. Majumder, N. Chopra, R. Andrews and B. J. Hinds. Nanoscale hydrodynamics - Enhanced flow in carbon nanotubes. *Nature*, 438(7064): 44, 2005.

[187] F. Du, L. Qu, Z. Xia, L. Feng and L. Dai. Membranes of vertically aligned superlong carbon nanotubes. *Langmuir*, 27(13): 8437–8443, 2011.

[188] R. Chang, G. S. Ayton and G. A. Voth. Multiscale coupling of mesoscopic- and atomistic-level lipid bilayer simulations. *J. Chem. Phys.*, 122: 244716, 2005.

[189] R. Delgado-Buscalioni and G. D. Fabritiis. Embedding molecular dynamics within fluctuating hydrodynamics in multiscale simulations of liquids. *Phys. Rev. E*, 76: 036709, 2007.

[190] M. Praprotnik, L. D. Site and K. Kremer. A macromolecule in a solvent: Adaptive resolution molecular dynamics simulation. *J. Chem. Phys.*, 126: 134902, 2007.

[191] W. Ren. Analytical and numerical study of coupled atomistic-continuum methods for fluids. *J. Comput. Phys.*, 227(2): 1353–1371, 2007.

[192] C. J. Garcia-Cervera, W. Ren, J. Lu and W. E. Sequential multiscale modeling using sparse representation. *Commun. Comput. Phys.*, 4: 1025–1033, 2008.

[193] R. Delgado-Buscalioni, K. Kremer and M. Praprotnik. Coupling atomistic and continuum hydrodynamics through a mesoscopic model: Application to liquid water. *J. Chem. Phys.*, 131: 244107, 2009.

[194] W. Hankui, Z. Xiong and Q. Ximming. Adaptive smoothed molecular dynamics for multiscale modeling. *Comput. Mater. Sci.*, 46(3): 713–715, 2009.

[195] I. G. Kevrekidis and G. Samaey. Equation-free multiscale computation: Algorithms and applications. *Annu. Rev. Phys. Chem.*, 60: 321–344, 2009.

[196] F. Dommert, J. Schmidt, C. Krekeler, Y. Y. Zhao, R. Berger, L. D. Site and C. Holm. Towards multiscale modeling of ionic liquids: From electronic structure to bulk properties. *J. Mol. Liq.*, 152: 2–8, 2010.

[197] K. Gu, C. B. Watkins and J. Koplik. Atomistic hybrid DSMC/NEMD method for nonequilibrium multiscale imulations. *J. Comput. Phys.*, 229: 1381–1400, 2010.

[198] K. M. Mohamed and A. A. Mohamad. A review of the development of hybrid atomistic-continuum methods for dense fluids. *Microfluid. Nanofluid.*, 8: 282–302, 2010.

[199] S. Poblete, M. Praprotnik, K. Kremer and L. D. Site. Coupling different levels of resolution in molecular simulations. *J. Chem. Phys.*, 132: 114101, 2010.

[200] D. A. Lockerby, C. A. Duque-Daze, M. K. Borg and J. M. Reese. Time-step coupling for hybrid simulations of multiscale flows. *J. Comput. Phys.*, 237: 344–365, 2013.

[201] W. E and B. Engquist. The hetereogeneous multi-scale methods. *Comm. Math. Sci.*, 1: 87–133, 2003.

[202] W. Ren and W. E. Heterogeneous multiscale method for the modeling of complex fluids and micro-fluidics. *J. Comput. Phys.*, 204: 1–26, 2005.

[203] W. E, B. Engquist, X. Li, W. Ren and E. Vanden-Eijnden. Heterogeneous multiscale methods: A review. *Commun. Comput. Phys.*, 2(3): 367–450, 2007.

[204] W. E. *Principles of Multiscale Modeling.* Cambridge University Press, 2011.

[205] S. T. O'Connell and P. A. Thompson. Molecular dynamics-continuum hybrid computations: A tool for studying complex fluid flows. *Phys. Rev. E*, 52(6): R5792–R5796, 1995.

[206] N. G. Hadjiconstantinou and A. T. Patera. Heterogeneous atomistic-continuum representations for dense fluid systems. *Int. J. Mod. Phys.*, 8(4): 967–976, 1997.

[207] T. Werder, J. H. Walther and P. Koumoutsakos. Hybrid atomistic-continuum method for the simulation of dense fluid flows. *J. Comput. Phys.*, 205(1): 373–390, 2005.

[208] E. G. Flekkoy, G. Wagner and J. Feder. Hybrid model for combined particle and continuum dynamics. *Europhys. Lett.*, 52(3): 271–276, 2000.

[209] E. G. Flekkoy, R. Delgado-Buscalioni and P. V. Coveney. Flux boundary conditions in particle simulations. *Phys. Rev. E*, 72(2): 1–9, 2005.

[210] S. Yasuda and R. Yamamoto. A model for hybrid simulations of molecular dynamics and computational fluid dynamics. *Phys. Fluids*, 20: 113101, 2008.

[211] N. Asproulis, M. Kalweit and D. Drikakis. A hybrid molecular continuum method using point wise coupling. *Adv. Eng. Softw.*, 46(1): 85–92, 2012.

[212] W. E, W. Ren and E. Vanden-Eijnden. A general strategy for designing seamless multiscale methods. *J. Comput. Phys.*, 228: 5437–5453, 2009.

[213] D. Stephenson, D. A. Lockerby, M. K. Borg and J. M. Reese. Multiscale simulation of nanofluidic networks of arbitrary complexity. *Microfluid. Nanofluid.*, in press, 2014.

[214] J. K. Holt, H. Y. Park, Y. Wang, M. Stadermann, A. B. Artyukhin, C. P. Grigoropoulos, A. Noy and O. Bakajin. Fast mass transport through sub-2-nanometer carbon nanotubes. *Science*, 321: 1034 – 1037, 2006.

[215] X. Qin, Q. Yuan, Y. Zhao, S. Xie and Z. Liu. Measurement of the rate of water translocation through carbon nanotubes. *Nano Lett.*, 11: 2173–2177, 2011.

[216] H. L. Weissberg. End correction for slow viscous flow through long tubes. *Phys. Fluids*, 5(9): 1033–1036, 1962.

[217] S. Sisavath, X. Jing, C. C. Pain and R. W. Zimmerman. Creeping flow through an axisymmetric sudden contraction or expansion. *J. Fluids Eng.*, 124: 273–278, 2002.

[218] S. D. Luca, B. D. Todd, J. S. Hansen and P. J. Daivis. Molecular dynamics study of nanoconfined water flow driven by rotating electric fields under realistic experimental conditions. *Langmuir*, 30: 3095–3109, 2014.

[219] W.-F. Chan, H. yan Chen, A. Surapathi, M. G. Taylor, X. Shao, E. Marand and J. K. Johnson. Zwitterion functionalized carbon nanotube/polyamide nanocomposite membranes for water desalination. *ACS Nano*, 7(6): 5308–5319, 2013.